MEMS PIEZOELECTRIC ENERGY HARVESTER FOR COCHLEAR IMPLANT APPLICATIONS

A THESIS SUBMITTED TO
THE GRADUATE SCHOOL OF NATURAL AND APPLIED SCIENCES
OF
MIDDLE EAST TECHNICAL UNIVERSITY

BY

LEVENT BEKER

IN PARTIAL FULFILLMENT OF THE REQUIREMENTS
FOR
THE DEGREE OF MASTER OF SCIENCE
IN
MICRO AND NANOTECHNOLOGY

JULY 2013

Approval of the thesis:

MEMS PIEZOELECTRIC ENERGY HARVESTER FOR COCHLEAR IMPLANT APPLICATIONS

submitted by **LEVENT BEKER** in partial fulfillment of the requirements for the degree of **Master of Science in Micro and Nanotechnology Department, Middle East Technical University** by,

Prof. Dr. Canan Özgen
Dean, Graduate School of **Natural and Applied Sciences** ---------------------

Prof. Dr. Tayfun Akın
Head of Department, **Micro and Nanotechnology** ---------------------

Assoc. Prof. Dr. Haluk Külah
Supervisor, **Electrical and Electronics Eng. Dept., METU** ---------------------

Prof. Dr. H. Nevzat Özgüven
Co-supervisor, **Mechanical Eng. Dept., METU** ---------------------

Examining Committee Members:

Prof. Dr. Tayfun Akın ---------------------
Electrical and Electronics Eng. Dept., METU

Assoc. Prof. Dr. Haluk Külah ---------------------
Electrical and Electronics Eng. Dept., METU

Prof. Dr. H. Nevzat Özgüven ---------------------
Mechanical Eng. Dept., METU

Prof. Dr. Nebil Göksu ---------------------
Otolaryngology-Head and Neck Surgery Dept., Gazi University

Assist. Prof. Dr. Ali Muhtaroğlu ---------------------
Electrical and Electronics Eng. Dept., METU-NCC

Date: 18.07.2013

I hereby declare that all information in this document has been obtained and presented in accordance with academic rules and ethical conduct. I also declare that, as required by these rules and conduct, I have fully cited and referenced all material and results that are not original to this work.

Name, Last name: Levent Beker
Signature:

ABSTRACT

MEMS PIEZOELECTRIC ENERGY HARVESTER FOR COCHLEAR IMPLANT APPLICATIONS

Beker, Levent

M.Sc., Department of Micro and Nanotechnology
Supervisor: Assoc.Prof.Dr. Haluk Külah
Co-Supervisor: Prof.Dr. H. Nevzat Özgüven

July 2013, 85 pages

This thesis proposes a novel method for eliminating the battery dependency of cochlear implant users. The proposed method utilizes a MEMS harvester mounted onto the eardrum. The harvester converts the vibrations of the eardrum to electricity and supplies the generated electricity to the cochlear implant; thus, reducing the battery replacement/recharge problems. As an extension of the proposed method, by utilizing a multi-frequency harvester, electricity can be generated while sensing the frequency of the vibration. By transferring the generated electrical signals to corresponding regions inside the cochlea, auditory nerve can be stimulated. Thus, a fully implantable and self-powered cochlear implant can be realized with the harvester, which electromechanically mimics the operation of cochlea.

Modeling, design, and optimization studies are conducted by considering operational conditions. Due to comparable mass and stiffness parameters of the eardrum and the harvester, structures are coupled using finite element method (FEM). Initially, the harvester is modeled, and a macro-scale prototype is fabricated for verification. Then, a membrane model is developed utilizing FEM. Eventually, these structures are coupled and optimized.

Among possible methods for fabrication of piezoelectric energy harvester, bulk piezoceramics is preferred due to its high strain coefficients and high output power potential. A fabrication method is implemented to integrate piezoceramics into MEMS. The fabrication process involves low-temperature bonding and thinning processes. Finally, the fabricated devices are tested, and it is shown that the harvester is capable of supplying electrical power of 1.33 μW at 0.1g while resonating at its resonance frequency of 474 Hz.

Keywords: cochlear implant, MEMS, piezoelectric, energy harvester, vibration energy harvesting, implantable microsystem.

ÖZ

KOKLEAR İMPLANT UYGULAMALARI İÇİN MEMS PİEZOELEKTRİK ENERJİ ÜRETECİ

Beker, Levent

Yüksek Lisans, Mikro ve Nanoteknoloji Bölümü
Tez Yöneticisi: Doç.Dr. Haluk Külah
Ortak Tez Yöneticisi: Prof.Dr. H. Nevzat Özgüven

Temmuz 2013, 85 sayfa

Bu tez çalışmasında, koklear implant kullanıcılarının batarya bağımlılıklarını azaltmaya yönelik yeni bir metod önerilmiştir. Önerilen metod kulak zarına bağlı olarak çalışan bir MEMS enerji üreticini kullanmaktadır. Enerji üreteci kulak zarı titreşimlerini elektriğe çevirmekte ve koklear implantı beslemektedir; böylece batarya değiştirme/şarj etme problemini azaltmaktadır. Önerilen metodun başka bir varyasyonu çoklu frekans enerji üreteci kullanılarak elektrik üretilmesi ve aynı zamanda titreşim frekansının belirlenmesidir. Üretilen elektrik sinyallerini kokleanın ilgili bölgelerine ulaştırarak işitme sinirleri uyarılabilmektedir. Böylece, kokleanın çalışma prensibini elektro-mekanik olarak mimic eden bir enerji üreteci ile tamamen vücut içinde ve kendi enerjisini sağlayabilen bir koklear implant gerçekleştirilmiş olacaktır.

Modelleme, tasarım ve optimizasyon çalışmaları çalışma koşullarını hesaba katarak yapılmıştır. Kulak zarının ve enerji üretecinin birbirine yakın kütle ve esnekliklerinin olmasından dolayı yapılar sonlu elemanlar metodu (SEM) kullanarak entegre edilmiştir. Başlangıçta, enerji üreteci modeli geliştirilmiş ve makro boyutta bir prototiple doğrulanmıştır. Daha sonra, SEM kullanılarak bir membran modeli geliştirilmiştir. Son aşamada, bu iki yapı birleştirilmiş ve optimizasyon çalışmaları yapılmıştır.

Piezoelektrik enerji üreteçlerini üretmek için diğer metodlar arasında yüksek gerinim katsayılarından ve yüksek güç potansiyeli olmasından ötürü hazır piezoseramik yapılar tercih edilmiştir. Bu piezoseramik yapıların MEMS yapılarına entegrasyonu amacıyla bir üretim metodu uygulanmıştır. Üretim aşamaları düşük sıcaklıkta yapıştırma ve inceltme işlemlerini de kapsamaktadır. Son olarak üretilen cihaz test edilmiş ve 0.1g ivme altında rezonans frekansı olan 474 Hz'de titreşirken 1.33 µW güç üretmiştir.

Anahtar kelimeler: koklear implant, MEMS, piezoelektrik, enerji üreteci, titreşim enerji üreteci, implant edilebilir mikrosistem.

To

My wife Fulya,
My brothers Cem & Can,
My parents Selma & Nuri,
My nephew Ali Sungur…

Your endless love, support, and
patience made this possible…

ACKNOWLEDGMENTS

From the beginning of my thesis study, I met with many people who helped me during my research for the last three years. I would like to express my sincere gratitude to everybody for enabling this thesis. First, I would like to express my appreciation and thanks to my supervisor Assoc. Prof. Dr. Haluk Külah for his supervision, guidance, and criticism. Without his support and belief in my ideas, this thesis could not be realized. I would also like to thank my co-supervisor Prof. Dr. H. Nevzat Özgüven for his invaluable guidance and support. Even with his very busy schedule, he has always managed to allocate time for my research and give inspiring ideas.
I am grateful to Assist. Prof. Dr. Ali Muhtaroğlu for his support and belief in my research, especially in the keyboard energy harvesting project. Long phone meetings and his criticism helped me a lot during my research. I wish to express my gratitude to Prof. Dr. Nebil Göksu for his support, guidance, and belief in my research. I am also thankful to him for sparking my interest in cochlear implants with his excitement. I want to thank Prof. Dr. Tayfun Akın for his support in my research. Without the wonderful research environment, METU-MEMS Center, this thesis could not be realized.
I would like to thank to Dr. Özge Zorlu for his guidance during my research. His support made everything easier for me and helped me to gain the motivation I needed. In addition, I would like to acknowledge Dr. Orhan Akar for his dedication to the facility and sharing his invaluable fabrication experiences with me. Our discussions helped me a lot in my research and increased my critical thinking skills.
I am deeply honored and enjoyed sharing the same office with several colleagues and friends at the BioMEMS Group and the Structural Dynamics Group. They did everything they can to motivate me and support my research. I would like express my sincere gratitude to my outstanding colleagues Dr. Hatice Ceylan Koydemir, Caner Gençoğlu, Aziz Koyuncuoğlu, Hasan Uluşan, and Taylan Töral for their invaluable friendship, which means a lot for me. Knowing that they are around, made me feel comfortable at all times. I am deeply grateful to former members of our group Emre Tan Topal, Serol Türkyılmaz, Ekrem Bayraktar, and Dr. Ender Yıldırım for introducing me the lab environment and sharing their invaluable experiences. I really enjoyed the chats with Mustafa Kangül, Özgen Laçin, Rui Çolaço, and Dr. Murat Aykan.
I would like to thank to all my friends at the METU-MEMS Group. They always tried to help me when I was in need. Especially Mert Torunbalcı and Osman Aydın helped me a lot during long cleanroom days. I am thankful to all the personnel making the METU-MEMS Facility such a great place with their kind friendship. I am grateful to Mr. Murat Demirpolat for helping me during the shear test apparatus manufacturing.
I am grateful to the Aselsan personnel Ufuk Temoçin and Alp Tolungüç for supporting me during gold-indium bonding and thinning studies. I want to thank Dr. Yetkin Arslan and Dr. Ethem E. Aktakka for their advices on flip-chip bonding and fabrication.
This work has been supported by Intel Corp., and TUBITAK Project No: 109E220. I am grateful to them for providing me the necessary means to conduct my study and game me the opportunity to present my research in high level international conferences.

I want to express my deepest gratitude to my wife, Fulya Beker, for her love, patience, and support at all times. I am very lucky to have her in my life. I would like to express my deepest appreciation to my nephew, Ali Sungur. Knowing that he is always there for me, gives me the motivation I needed. I owe special thanks to my parents, Selma and Nuri Beker, and my brothers Cem and Can Beker. I am grateful for their endless patience and support during my studies. It was wonderful to visit them during my studies at METU and see their smiling faces to regain the energy I needed. Without their belief in me, this study could not be realized. This study is dedicated to them.

TABLE OF CONTENTS

LIST OF TABLES

TABLES

LIST OF FIGURES

FIGURES

CHAPTER 1

INTRODUCTION

Advances in microelectronics manufacturing industry, low-power circuit design, and networking algorithms have increased the computational performance while reducing the power requirement of electronic circuits to the order of microwatts. On the other hand, recent improvements in microsystem technologies have enabled the development and fabrication of micro-mechanical systems that can interact with their physical surroundings. In this sense, combination of the microelectronics with micro-mechanical systems, or micro-electro-mechanical systems (MEMS), has started to revolutionize our lives starting from 1980s with the first commercialized MEMS pressure sensors [1]. When compared to their macro-scale counterparts, MEMS transducers provide smaller size, higher performance, lower power consumption, and lower cost. These advantages of MEMS have brought radical developments in many areas, such as automotive, health, defense systems, and consumer electronics [2].

One of the most recent topics that MEMS researchers are struggling with today is energy harvesting. The purpose of the research in this field is to convert available surrounding energy (such as mechanical vibrations, light, heat, etc.) to electrical energy for powering up systems without the need of battery. Battery or electric cable requirement of devices can thus be disregarded or reduced; self-supplied, renewable, and green energy systems can be realized. Besides, due to their relatively small size, energy harvesting systems led many emerging applications, such as implants, bio-MEMS applications, wireless sensor networks, etc.

Another area that MEMS has a particular importance is health industry. Because of the micro-scale size of the MEMS devices, they become a perfect candidate for medical applications and implantable systems. Recently, drug delivery systems [3], pacemakers [4], neural recording systems [5], microneedles [6], and blood pressure sensors [7] have been studied widely. Most of these systems have been commercialized or in commercialization stage. However, up to now, middle ear applications of microsystems have not been investigated in depth. For instance, currently, cochlear implants are used by more than 220.000 patients worldwide [8], and there have not been any significant improvement in this industry over the past three decades. Some of the drawbacks of the cochlear implants limiting their daily usage are: frequent battery replacement/charging requirement [9], damage risk of external components especially if exposed to water (shower, rain, pool, etc.), aesthetic concerns of the patients [8], and high cost [10]. In the scope of this thesis, novel cochlear implant applications are proposed to eliminate the mentioned drawbacks of the conventional cochlear implants. In this regard, a micro-scale piezoelectric energy harvester is designed and fabricated by considering the middle ear dynamics. The harvester is designed such that it can convert the vibrations of the eardrum to electricity for possible applications to provide continuous access to sound for patients. The first proposed application is aimed to reduce the battery recharge problems of cochlear implants by supplying the generated electricity to the battery. With this method, harvested mechanical power of the eardrum can be used to increase the time of operation of the cochlear implants. The second application utilizes a multi-frequency harvester to generate frequency-discriminated electrical signals. Then, generated signals are used to stimulate corresponding sections of the auditory nerve. Thus, with this method it is possible to eliminate electronic components (such as microphone, processor, transmitter) and battery requirement of the conventional cochlear implants and a fully implantable and self-powered cochlear implant can be realized [11–13].

This chapter presents a literature survey related with micro-scale vibration based energy harvesting with a focus on piezoelectric transduction mechanism. Then, biomedical applications of MEMS are given with specific and recent examples. Finally, motivation, research objectives, and organization of the thesis are given at the end of the chapter.

1.1 Energy Harvesting

Many emerging applications such as wireless sensor networks (structural health monitoring systems, tire pressure monitoring systems) and portable consumer electronic devices require autonomous operation. However, battery does not provide a successful experience to the end-users due to its limited energy and periodic maintenance requirement. Although there has been a significant improvements in the low-power circuit design and power consumption of the transducers, studies on batteries and power storage systems could not provide a sustained solution for powering up the autonomous electronics. Moreover, the batteries utilize materials that are not eco-friendly and are not desired for consumer electronics [14].

Table 1.1: Comparison of main energy harvesting sources [15].

		Power Density (μW/cm³) 1-year lifetime	**Power Density (μW/cm³) 10-year lifetime**	**Source of information**
Scavenged power sources	*Solar (outdoors)*	15.000 – direct sun 150 – cloudy day	15.000 – direct sun 150 – cloudy day	Commonly available
	Solar (indoors)	6 – office desk	6 – office desk	[16]
	Vibrations	200	200	[16]
	Acoustic noise	0.003 @75 dB	0.003 @75 dB	Theory
		0.96 @100 dB	0.96 @100 dB	
	Daily Temp. variation	10	10	Theory
	Temperature gradient	15 @10 °C gradient	15 @10 °C gradient	[17]
	Shoe inserts	330	330	[18]
Energy reservoirs	*Batteries (non-rechargeable Lithium)*	45	3.5	Commonly available
	Batteries (rechargeable Lithium)	7	0	Commonly available
	Hydrocarbon fuel (micro heat engine)	333	33	[19]
	Fuel cells (methanol)	280	28	Commonly available
	Nuclear isotopes (uranium)	$6x10^6$	$6x10^5$	Commonly available

On the other hand, reduced power requirements of the transducers have enabled the use of environmental energy sources to be used as an energy source by employing energy harvesting techniques. For this reason, in the last decade, energy harvesting has received great attention.

Recently, researchers strive to develop micro-scale energy harvesting devices to convert mechanical vibrations, heat, solar energy to electrical energy for powering up transducers.

Roundy *et al*. conducted a detailed analysis on these sources in 2003 [15]. As seen from the Table 1.1, solar energy might be seen as the most feasible alternative source, since it provides power densities between 150 µW/cm^3 to 15.000 µW/cm^3 [15]. However, the solar energy is not available in closed environments and at nights, which reduces its application areas and effectiveness. Furthermore, when the power density of indoor solar energy is considered, it decreases considerably, down to 6 µW/cm^3. On the other hand, energy harvesting using heat gradients provides a sustained power density (when considered in 1 and 10-year lifetime). However, it has a power density of 10 µW/cm^3 under 30 °C gradients, which is low compared to the requirements of the transducers. Vibration energy has an advantage of abundance, and supplying continuous power is an important issue that should be considered when powering up transducers. Unlike low power densities of solar and heat energy, vibration has a power density between 100 to 200 µW/cm^3. Another advantage of harvesting energy from vibrations is that, it does not make use of non-eco-friendly materials as in the batteries and provides clean energy. Another comparison study was conducted by Cook-Chennault *et al*. [20]. Figure 1.1 shows the comparison of the power densities of solar energy and other vibration energy harvesting techniques. It can be seen that vibration energy harvesting techniques (piezoelectric, and electromagnetic) occupy much more area than solar cells, and especially piezoelectric materials are promising candidate among other methods. Thus, vibration energy harvesting is the most advantageous method among other methods in terms of energy density, sustainability, and environmental issues.

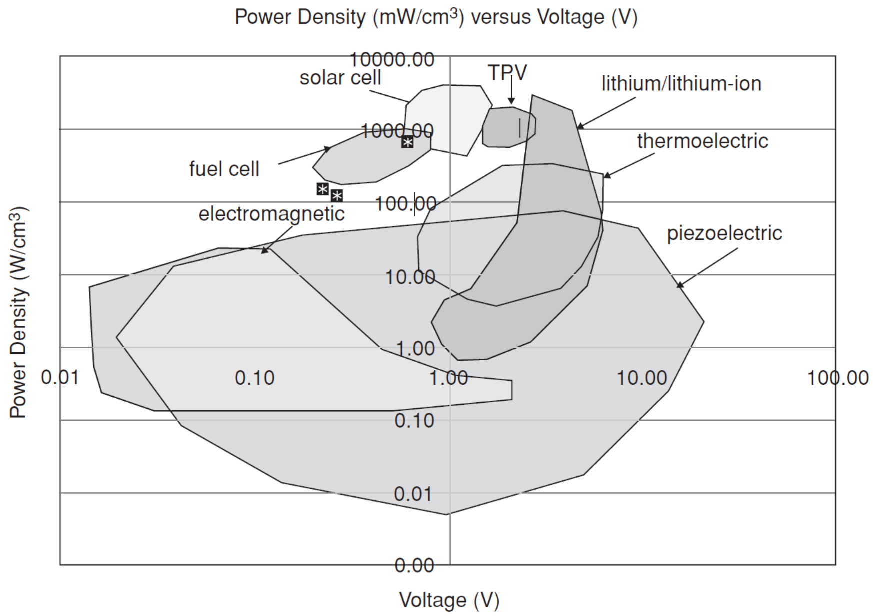

Figure 1.1: Power density versus voltage plot for various transduction mechanisms and lithium-based supplies [20].

1.1.1 Vibration Energy Harvesting

In recent studies, it is practically shown that vibration energy harvesting techniques are able to power-up various types of transducers [21–26]. These studies show the feasibility of vibration-based energy harvesting techniques. Up to now, three different transduction mechanisms have been studied in the literature for converting vibrations to electrical energy: electromagnetic (inductive), electrostatic (capacitive), and piezoelectric. Below subsections will give more detailed information on these techniques.

1.1.1.1 Electromagnetic (Inductive) Energy Harvesting

The principle of the electromagnetic energy harvesting is based on the Faraday's law of electromagnetic induction. This law states that when the magnetic field through a conductor changes, an electrical current is generated. Therefore, by configuring the magnet and coil structures accordingly and providing a relative motion between these structures, it is possible to generate an induced current through the coil structures. By making use of this phenomenon, starting from mid-90s, researchers investigated in various electromagnetic energy harvesting structures.

An initial detailed research on micro-scale electromagnetic energy harvesters are conducted by the University of Sheffield researchers in 1996 [27]. This paper proposes an electromagnetic energy harvester, where the magnet is moving through the center of the coils. Effects of electrical damping and vacuum environment on the resonant structure are also presented in this study. Later on, in 2001 researchers microfabricated the proposed electromagnetic energy harvester and reported experimental results [28]. A samarium-cobalt magnet is attached to a polyimide membrane to create magnetic flux on top the coil structures as shown in Figure 1.2a, where the total volume of the device is 0.25 mm^3. Experimental studies were conducted using a shaker table, and ~1 µW power is generated around frequency of 4.3 kHz while the vibration amplitude was 0.5 µm and a resistive load of 39 kΩ was connected to the harvester. Characteristics of the fabricated device while resonating was also elaborated, and two conclusions were derived from this study. These conclusions are that maximum power output can be obtained when electrical damping matches mechanical damping, and the generated power is proportional to the cube of the input vibration frequency. Authors also proposed a single-degree-of-freedom model of the energy harvester, which is similar to the representation of an accelerometer as shown in Figure 1.2b.

El-Hami *et al.* from the University of Southampton have designed and fabricated an electromagnetic energy harvester in 2000 [29]. This study makes use of finite element analysis in order to determine the magnetic flux around the coils. It is reported that, by exciting the system with 25 µm amplitude vibrations at 320 Hz, 0.53 mW power can be generated within a volume of 240 mm^3. In 2004, researchers from the same group implemented two different designs to compare the performances of the harvesters [22]. First prototype is a two-magnet generator while second is a four-magnet generator. The latter design was implemented to a car engine, and a 158 µW power is generated on average. Importance of the magnet and coil configurations and considerable low output voltage of micro-scale electromagnetic harvesters with respect to macro-scale ones are emphasized in this study.

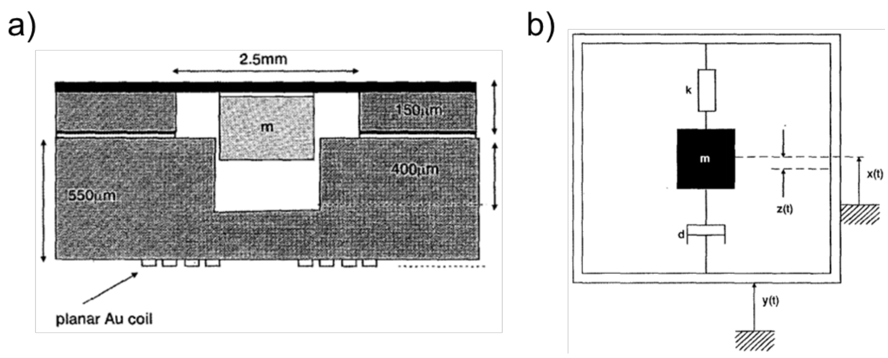

Figure 1.2: a) Schematic view of the microfabricated electromagnetic energy harvester with 0.25 mm^3 volume, b) equivalent mass-spring-damper model of the electromagnetic energy harvester [28].

Several system-level studies have been conducted lately on electromagnetic energy harvesting method to elaborate on its performance [30–32]. It is observed that the main problem of electromagnetic energy harvesters is that the generated voltage relies on the rate of magnetic flux change. In this sense, high frequency vibrations are favorable for this application. On the other hand, this makes electromagnetic energy harvesting method not a viable solution for low-frequency applications. In order to overcome this problem, Kulah *et al*. from the University of Michigan proposed a novel method to increase the time rate of change of the magnetic flux by utilizing the "frequency up-conversion" method [33]. The aim of this method is to up-convert the low-frequency vibrations to relatively higher frequency by making use of structural resonance phenomena. As a continuation of this work, Sari *et al*. from the Middle East Technical University, microfabricated a 0.15 cm^3 electromagnetic harvester having 3.8 x 3.8 x 1.5 mm^3 NdFeB magnet of 1.18 T [34]. Figure 1.3a shows the image of the fabricated device assembly. Experimental results showed that a maximum peak power and voltage output of 0.25 nW and 0.57 mV can be generated by exciting a single device at 113 Hz. This study also compares the proposed method with traditional electromagnetic energy harvester design (Figure 1.2a), and it is showed that proposed method increases the efficiency of the harvester considerably. In 2011, Galchev *et al*. assembled an AA-battery-sized electromagnetic harvester with volume of 2.12 cm^3 (Figure 1.3b). The assembled harvester is aimed to be operating below 20 Hz and generated an average power of 13.6 μW from an input acceleration of 1g at 10 Hz. Zorlu *et al*. also investigated the frequency up-conversion method and proposed a method which mechanically up-converts the input vibration frequency [35]. It is experimentally shown that 88.6 mV and 544.7 μW rms power output can be generated by up-converting 10 Hz input vibrations to 394 Hz.

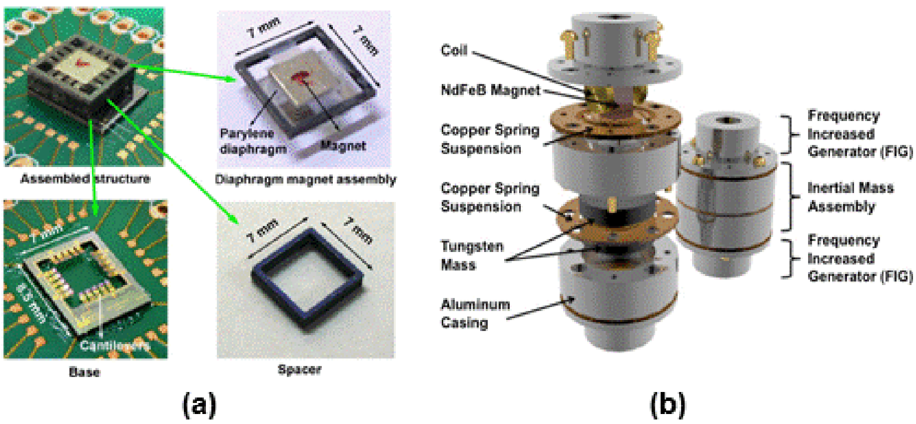

Figure 1.3: Image of the frequency-up converter electromagnetic energy harvester assembly by a) [34] *b)* [36].

Another issue on electromagnetic energy harvesting is related with the scalability. Electromagnetic energy harvesters show high efficiency at macro-scale. However, they have relatively low voltage output in micro-scale, and it is not easy to implement these harvesters in micro-scale. Since the magnetic flux is dependent on the size and the magnetic properties of the magnet, decreasing the size of the magnet has considerable negative effects on the generated voltage. Therefore, generated voltage of the micro-scale electromagnetic energy harvesters is relatively low when compared to its macro-scale counterparts or electrostatic and piezoelectric energy harvesters. Besides, integration of planar magnets into the microfabricated coil structures brings alignment and assembly problems, since planar magnet cannot be fabricated via standard MEMS fabrication processes. Another drawback of micro-scale electromagnetic energy harvesters is its rectifying circuitry, since implementation of a current-based circuitry for rectification purposes is not trivial as implementing a voltage-based circuitry [37].

1.1.1.2 Electrostatic (Capacitive) Energy Harvesting

Electrostatic energy harvesting utilizes capacitance change between two charged plates. The relative movement between two charged plates result in a capacitance change, thus system acts as a current or voltage source. One of the most favorable advantages of the electrostatic energy harvesters is their CMOS-compatible fabrication process. Their structure is similar to accelerometers or gyroscopes. Usually a design utilizing an inertial mass with several comb fingers is considered for electrostatic energy harvesters. By configuring the dimensions of inertial mass and crab leg structures, which are supporting the inertial mass, resonance frequency of the structure can be tuned to desired range. Typical electrostatic energy harvester designs are shown in Figure 1.4. In-plane overlap and in-plane gap closing type of harvesters are used to convert the vibrations, which are in plane with the harvester. The out-of-plane gap closing type of harvester is used to convert to vibrations, which are perpendicular to the harvester plane.

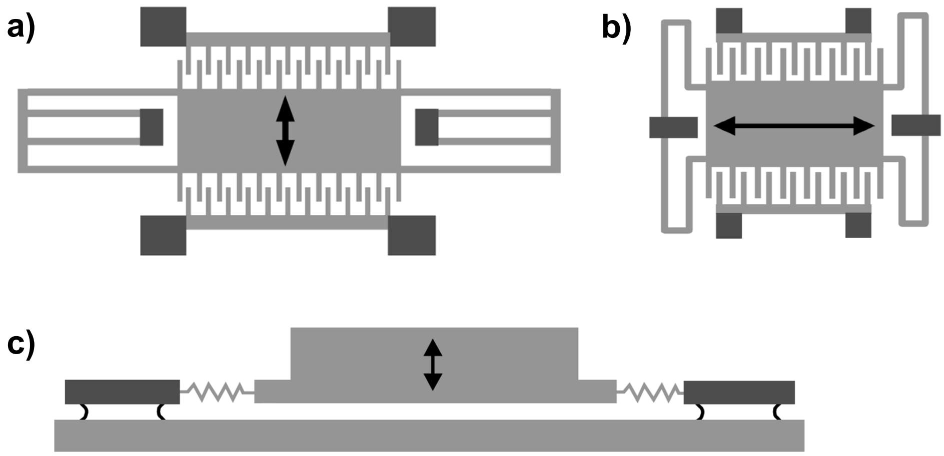

Figure 1.4: Typical electrostatic energy harvester designs, a) in-plane overlap, b) in-plane gap closing, c) out-of-plane gap closing converter.

Sterken *et al*. from IMEC presented a microfabricated gap-closing electret-based structure in 2003. Proposed structure was fabricated using a silicon-on-insulator (SOI) wafer, and the prototype has a resonance frequency of 980 Hz and a footprint of 2.65 mm^2. Within this area, 255 comb pairs (the gap between 2 µm wide fingers is 2.2 µm) were realized and the capacitance of the structure was measured as 0.6 pF. Experimental investigation of the 10V-polarized prototype showed that the energy harvester is capable of generating 2 nW when an excitation of 500 Hz under 1 g is applied. Considerable increase in power levels was observed when polarization levels were increased. When an initial polarization of 100 V was applied, a power of 5 µW has been observed.

In 2009, Basset *et al*. proposed an in-plane gap closing type of micro-scale harvester [38]. The fabricated prototype has a total volume of 0.1 cm^3. Schematic view of the harvester is given in Figure 1.5. After an initial charge of 6 V via a supply, 61 nW of power is obtained with vibrations of 250 Hz under acceleration of 0.25g.

Although electrostatic energy harvesters are favorable in terms of fabrication, the polarization requirement of the structures lacks their use in many applications. This and a requirement for mechanical stop are main disadvantages of the electrostatic energy harvesters. Besides, high output impedance especially at low frequencies and corona-charging issues are other problems related with this method. When compared with piezoelectric harvesters, displacement range of the electrostatic harvesters is limited due to pull-in voltage. Furthermore, low power density, stiction problems, and parasitic capacitance on output power of these devices make them unfavorable.

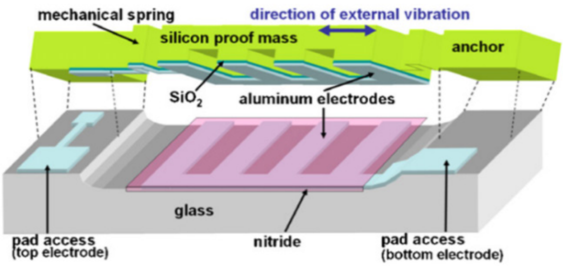

Figure 1.5: 3D schematic view of the electrostatic energy harvester [38].

1.1.2 Piezoelectricity Phenomena and Piezoelectric Energy Harvesting

1.1.2.1 Piezoelectricity

Piezoelectricity is a coupling behavior of material's mechanical and electrical properties. This electromechanical coupling arises from charge asymmetry of the crystal lattice. When a material is twisted or compressed, spontaneous polarization within the material is further exaggerated and a potential difference is developed across the crystal structure. Upon application of a high electric field these spontaneous polarization of crystals can be set to a desired direction (Figure 1.6). Corona charging method is applied at elevated temperatures for polarization of the commercial piezoelectric materials such as PZT.

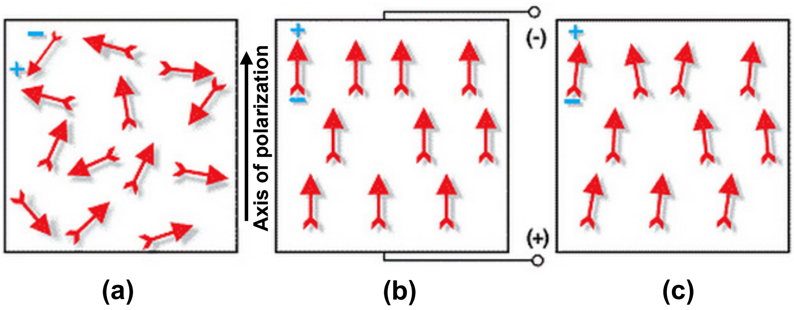

Figure 1.6: Poling a piezoelectric ceramic, a) random orientation of polar domains before polarization, b) polarization in DC field, c) remanent polarization after electric field removed [39].

After polarization process, piezoelectric materials are able to generate electrical voltage output when a mechanical stress is induced within the material, and this behavior is called direct piezoelectric effect (Figure 1.7b-c). Conversely, generation of a mechanical stress due to an applied electrical voltage is called inverse piezoelectric effect (Figure 1.7d-e). The generated electrical voltage or stress is proportional to the applied stress or voltage respectively.

The direct piezoelectric effect was discovered by the Curie brothers in 1880. One year later, inverse piezoelectric effect was observed by Lippmann along with its mathematical relations [40]. In the same year, the Curie brothers experimentally verified these mathematical relations for the direct effect. The standard form of the piezoelectric constitutive equations is given in Equation 1.1 and Equation 1.2 [39].

$$S_i = s_{ij}^E T_j + d_{mi} E_m \tag{1.1}$$

$$D_m = d_{mi} T_i + \varepsilon_{mk}^T E_k \tag{1.2}$$

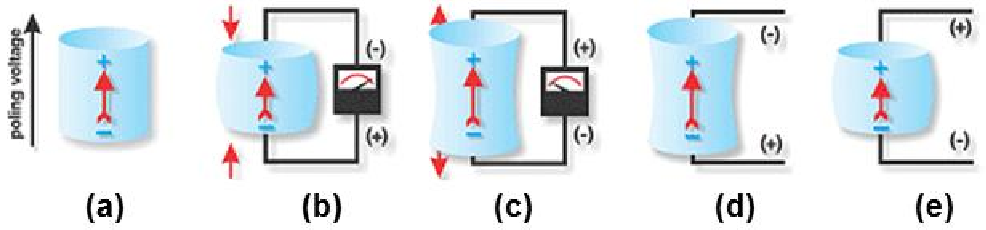

Figure 1.7: Direct and inverse piezoelectric effects, a) poling direction of a disk type piezoceramics, b) disk compressed: generated voltage has same polarity as poling voltage, c) disk stretched: generated voltage has polarity opposite that of poling voltage, d) applied voltage has same polarity as poling voltage: disk lengthens, e) applied voltage has polarity opposite that of poling voltage: disk shortens [39].

In these equations, S_i represents the strain component, T_j is the stress, E_m is the electric field, D_m is the electric displacement, s_{ij} is the elastic compliance constant, d_{mi} is the piezoelectric constant, and ε_{ik} is the permittivity constant. Superscript E represents that the constant is evaluated at constant electric field. Similarly, superscript T represents that the constant is evaluated at constant stress. Subscripts (ij) are used such that the former is used to represent the direction of excitation while the latter represents the direction of the response. These materials do not exhibit isotropy; thus, their material behavior and orientation should be considered during modeling and design.

1.1.2.2 Piezoelectric Energy Harvesting

Piezoelectric materials are used in many applications due to their ease of application and high power density. Figure 1.8 shows possible applications of piezoelectric transducers. Among other applications, piezoelectricity is also utilized in energy harvesting applications. Recently, piezoelectric energy harvesting is the most widely studied energy harvesting technique due to high output voltage and power levels [41].

UC Berkeley researchers, Roundy *et al*., conducted the first detailed analysis for the use of piezoelectric materials in energy harvesting systems in 1999 [15]. An analytical model is proposed, and it is shown that mechanical damping and electrical damping should be equal and minimized in order to obtain maximum electrical power. As an initial verification of the developed models, macro-scale cantilever beam type of energy harvesters are tested with a resistive load (Figure 1.9a). Exciting a 0.83 cm^3 prototype with 0.23 g acceleration and at 60 Hz, 335 µW power is obtained under 200 kΩ resistive load.

Jeon *et al*. from MIT developed a micro-scale piezoelectric energy harvester by utilizing thin film piezoelectric materials [43]. Initially, statically bent cantilever structures were observed due to residual stress on the cantilever beams. After optimizing the fabrication process, researchers overcame this problem and developed an interdigitated electrode model in order to increase the voltage output of the piezoelectric material by employing strains through the polarization axis (Figure 1.9b). Experimental results showed that a peak-to-peak voltage of 3 V is generated under 10.1 MΩ resistive load when the harvester is excited at its resonance frequency of 13.9 kHz. As a continuation of this study, Hajati *et al*. presented an ultra-wide bandwidth energy harvesting concept by utilizing a nonlinear resonator [44]. A nonlinear electromechanical model representing the proposed structure is also presented in this study. Proposed doubly clamped cantilever type energy harvester is microfabricated with a thin-film PZT on a silicon nitride membrane (Figure 1.9c). Experimental results showed that fabricated harvester is able to generate a power density up to 2 W/cm^3 within a bandwidth of up to 75% of the resonance frequency. The prototype generated an open circuit voltage of 1 to 1.5 V while vibrating between frequencies 2000 Hz and 3000 Hz.

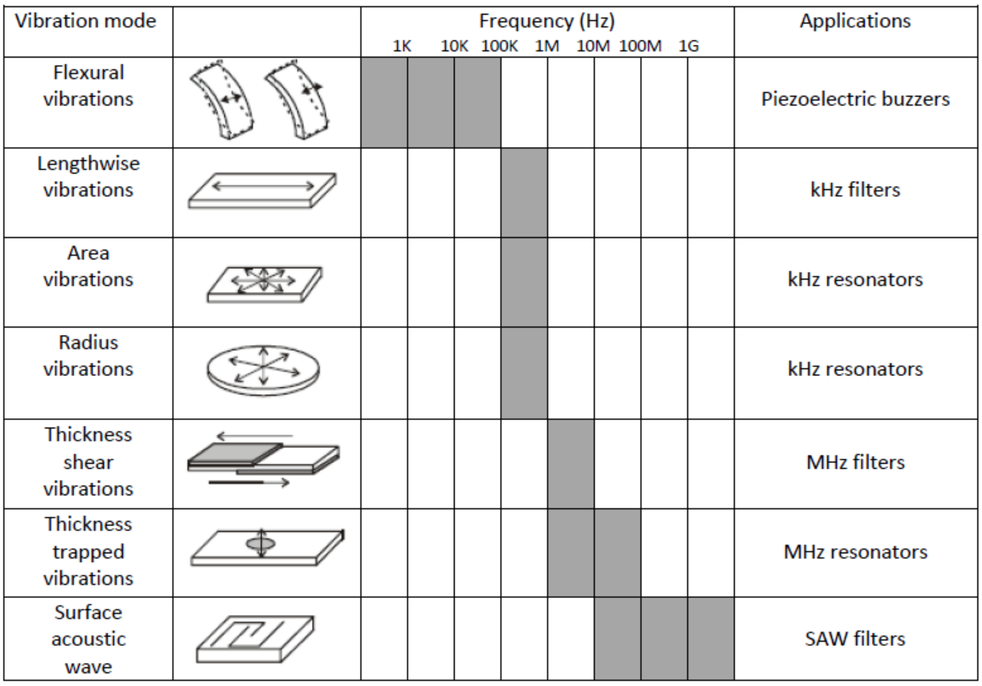

Figure 1.8: Various vibration modes and frequency ranges for piezoelectric transducer applications [42].

Recently Aktakka *et al*. from the University of Michigan has developed a micro-scale piezoelectric energy harvester by using bulk piezoceramics [37]. The advantage of bulk piezoceramics is its higher piezoelectric coefficient with respect to other materials; thus, yielding higher voltage outputs. However, the integration of bulk piezoceramics into standard MEMS fabrication processes is not trivial. Researchers developed a low-temperature bonding method by employing AuIn diffusion bonding, thus integrating bulk piezoceramics to silicon wafers without degrading their superior characteristics. Following this process, grinding is performed to thin down the piezoceramics to a desired thickness of around 10 to 20 µm. A wafer-level CMOS compatible fabrication flow is presented utilizing both bonding and thinning processes. A 0.027 cm^3 energy harvester prototype is fabricated and tested under acceleration levels of 0.1g to 1.5g around its natural frequency of 160 Hz (Figure 1.9d). It is seen that optimized energy harvester is capable of generating 205 µW and 2.74 µW under 1.5g and 0.1g, respectively.

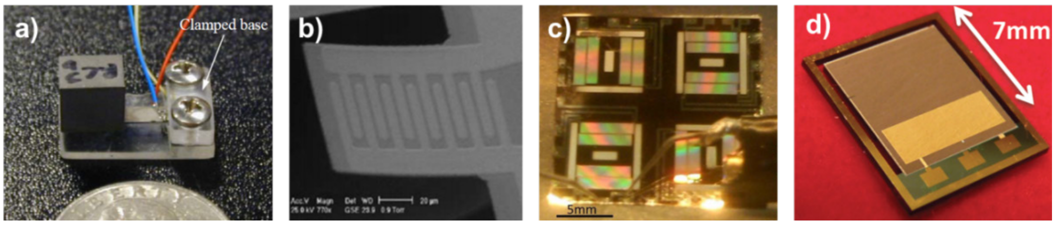

Figure 1.9: a) A macro-scale piezoelectric energy harvester [15], *b) microfabricated thin-film PZT energy harvester with interdigitated electrodes* [43], *c) nonlinear doubly clamped cantilever type wide-bandwidth energy harvester* [44], *d) piezoelectric energy harvester using bulk piezoceramics* [37].

When compared to electromagnetic energy harvesters, piezoelectric harvesters do not require bulky magnets, which cause assembly problems. Other major reason is higher voltage output of the piezoelectric harvesters. As stated previously, voltage-based rectification circuitry is easier to implement than current-based circuits. In this sense, micro-scale piezoelectric harvesters can be combined with electronics more easily than electromagnetic harvesters [37]. On the other hand, fabrication of electrostatic harvesters seems to be easier than fabrication of piezoelectric harvesters. However, when the structural complexity is considered, it is harder to design and optimize an inertial mass with hundreds of comb fingers and several crab leg structures compared to a cantilever beam, which represents the structure of choice for most piezoelectric harvesters.

1.2 Biomedical Applications of MEMS and MEMS-Based Energy Harvesting

Biomedical applications are an exciting field for MEMS, since the size scales of the MEMS are comparable with that of cells and human body. In addition, most of the materials used during MEMS fabrication, such as silicon, gold, silicon nitride, polydimethylsiloxane (PDMS), and parylene are biocompatible [3], [45], [46]. These features of MEMS-based devices enabled them to be applied in many biomedical applications, such as implants, drug delivery systems, tissue engineering, health screening, organ prosthesis, and surgery.

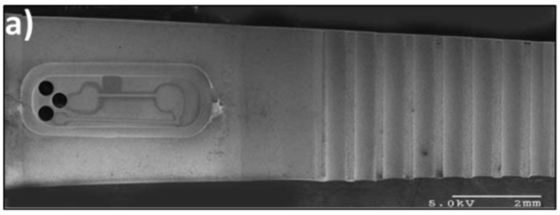

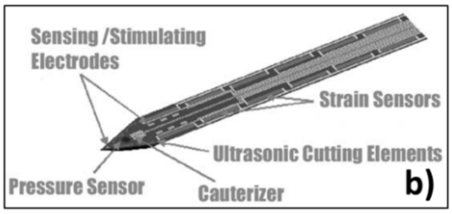

Figure 1.10: a) Embedded strain gauges and temperature sensors on a micro gripper, b) the data knife smart scalpel developed by Verimetra, Inc. [47].

Figure 1.10a shows strain gauge sensors fabricated concurrently with surgical sharps in order to eliminate disadvantages of glue layers such as epoxy and tape. Similarly, Figure 1.10b shows a smart scalpel developed by Verimetra, Inc., which has built-in pressure sensor, cauterizer, ultrasonic cutting element, strain sensor, and sensing/stimulating electrodes. In this system, the electrodes are used to measure the resistance and impedance of the tissue, which is used to classify tissues. Furthermore, they can be used to stimulate and identify nerves by picking-up electrical signals. Therefore, by using MEMS-based sensors, limits of surgical operations can be eliminated.

MEMS transducers have also been used for diagnostics. One of the most popular biomedical applications of piezoelectric transducers is piezoelectric micromachined ultrasound transducer (PMUT), which is used for medical imaging applications (Figure 1.11a) [48], [49]. Khuri-Yakub research group from Stanford is developing a capacitive micromachined transducer (CMUT), which has recently emerged as an alternative to PMUT due to wide bandwidth and ease of fabrication (Figure 1.11b) [50]. These ultrasound transducers are widely used in intravascular imaging applications. They can emit and receive sound waves, and can be placed easily through the vessels due to their small size.

Implantable microsystems receive great attention, due to their high potential to be used within human body. Pacemakers, insulin pumps are some of the most popular MEMS implants. Recently, UC Berkeley researchers proposed a new method for treatment of ocular posterior segment diseases via a MEMS drug delivery device [53]. With this device, the disadvantages of conventional laser ablation therapy and delivery of therapeutic agents via injection are eliminated. An implantable device, which is mounted to the posterior eyeball (Figure 1.12), is fabricated and *ex-vivo* studies have been conducted.

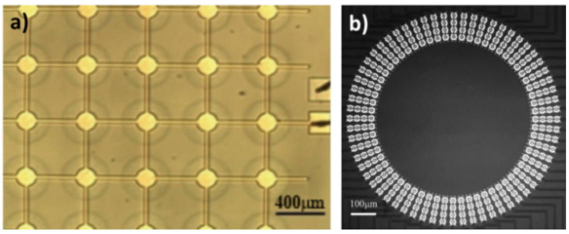

Figure 1.11: a) Micrograph of a ring-annular, 64-element cMUT for intravascular ultrasound (IVUS) imaging array [51]*, b)optical image of a rectangular shaped 5x5 pMUT array* [52].

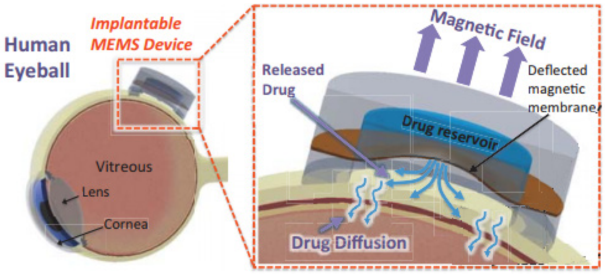

Figure 1.12: a) Schematic of a lab-on-a-chip system, b) conceptual illustration of MEMS drug delivery device to be used for the treatment of ocular posterior segment diseases [53].

These studies show that microsystems are a promising candidate for the treatment of diseases. Various types of microsystems are used as implants as sensors or actuators. Some of them, such as pacemakers, are commercialized. However, treatment of hearing impairment via microsystems has never been studied in the literature. In this thesis, an energy harvester structure is proposed to be used as an implant. The harvester is implanted onto eardrum, and converts the eardrum vibrations to electricity. The generated electrical signals can be used to eliminate the drawbacks of the conventional systems that are used by the patients, which will be discussed in Chapter 2 and Chapter 4.

1.3 Motivation and Research Objectives

MEMS have an enormous impact on medical industry, and its effect will become more obvious in the near future. As researchers strive in this field, new conceptual designs will be proposed for conventional treatments, and would make our life easier. One of the possible application fields of the microsystems is auditory sensory system, or more specifically, hearing impairment. According to the World Health Organization (WHO), over 5.3% of the world's population – 360 million people (328 million adults, 32 million children) – experience hearing loss greater than 40 dB SPL (sound pressure level) in 2012 [54]. Conventional hearing aids are used for the treatment of individuals with mild-to-moderate hearing loss. However, these devices cannot be used to aid individuals with severe-to-profound hearing loss where average loss is greater than 90 dB SPL [55]. In such cases, cochlear implants restore hearing to some degree via electronic devices such as microphone, sound processor, transmitter, and implant. Currently, cochlear implants are implanted to more than 220.000 patients worldwide [8]. However, these devices require battery. Depending on the usage of the patient and the surrounding sound levels, frequent battery replacement and charging problem (once or twice a day) prevents patients' continuous access to sound [8], [9]. Recently, a MEMS accelerometer is proposed to be used as an implantable microphone for a fully implantable cochlear prosthesis [56]. However, this system requires all other electronic components of the conventional cochlear implants (such as sound processor, battery, power management, and interface circuit) to be implanted within the skin. Besides, this method also needs external battery charging unit.

This thesis proposes an energy harvester coupled to the eardrum in order to eliminate the battery problem of the cochlear implants. The harvester converts the vibration of the eardrum to electrical energy by utilizing a piezoelectric material. By providing the generated electrical energy to the battery, cochlear implants can continue to operate.

Another problem that cochlear implant users face arises due to the external components. External components of the cochlear implants do not operate under aqueous environment such as rain, shower, pool, etc. Furthermore, external components bring aesthetic concern to the patient. In order to address this problem, a multi-frequency energy harvester can be mounted onto the eardrum to sense the frequency of the vibration and generate electricity. By transferring the generated electrical output directly to the auditory nerve, it is possible to eliminate the external components; thus realizing a fully implantable and self-powered cochlear implant, which overcomes the drawbacks of the conventional cochlear implants.

In this research, following objectives are aimed:

- A method to eliminate the battery charge/replacement problem of cochlear implant users with an implantable MEMS harvester:
    - which is mounted onto the eardrum.
    - that converts the vibrations of the eardrum to electricity.
    - that supplies the generated electricity to the battery of the cochlear implant to increase the time of operation.
- As an extension of the first proposal, a method to eliminate the external components and the battery need of the cochlear implants, thus realizing a fully implantable and self-powered cochlear implant:
    - which is mounted onto the eardrum.
    - that converts the vibrations of the eardrum to electricity by making use of a multi-frequency structure and works as a frequency transducer. Thus, the proposed device electromechanically mimics the operation of cochlea and can be used as a fully implantable and self-powered cochlear implant.
    - that transfers the generated frequency discriminated electricity to the corresponding section of the cochlea to stimulate the auditory nerve.
- Modeling, design, and optimization of a MEMS energy harvester capable of converting vibrations of the eardrum to electrical energy:
    - Mass and stiffness parameters of the MEMS energy harvester are comparable to that of the eardrum. Therefore, coupled system dynamics should be considered during design. Each structure (membrane and energy harvester) should be modeled separately and the verified before coupling.
    - Due to anisotropic nature of the piezoelectric material, a proper material model should be developed and verified by utilizing macro-scale prototypes.
    - Developed model should be parametric in order to optimize the design parameters for the maximum electrical output.
- Fabrication and testing of the MEMS energy harvester:
    - Bulk piezoceramics should be considered for high electrical output, and a compatible fabrication flow should be utilized for integration of bulk piezoceramics into MEMS processes.

- Low-temperature bonding process should be developed to prevent degrading of piezoelectric properties of material. In addition, thinning of the bonded piezoceramics should be accomplished to obtain desired natural frequency range for the harvester. In this regard, the shear strength of the bonding should be enough to survive during thinning process.
- Experiments of the fabricated harvester should be conducted to observe its performance under a specific sound frequency and SPL.

The thesis is organized as follows:

Chapter 2 explains modeling and design studies of the harvester mounted on eardrum. Following the explanation of the proposed application, brief information and literature review on theory and modeling of piezoelectric energy harvesters are given. Then, finite element modeling approach utilized for the piezoelectric energy harvester is presented in detail. Results from the macro-scale prototype are presented. The eardrum finite element (FE) model is developed, after the development and verification of a circular membrane structure. Developed FE models are coupled together and their dynamics are investigated. The chapter is concluded with the optimization study.

Chapter 3 presents fabrication flow of the piezoelectric energy harvester and experimental results. Initially, various methods of piezoelectric MEMS are discussed. Similarly, possible methods of integration of bulk PZT's are explained. Then, preferred bonding methods are investigated empirically. Details of the developed fabrication flow are explained. Finally, the chapter ends with experimental results of the fabricated harvester.

Chapter 4 explains the proposed method for the development of fully implantable and self-powered cochlear implant. Anatomy of the ear, hearing mechanism, and cochlear implants are explained briefly. Then, the proposed method for the development of fully implantable and self-powered cochlear implants is explained in detail.

Finally, conclusions and recommendations for possible future work are presented in Chapter 5.

CHAPTER 2

MODELING, DESIGN, AND OPTIMIZATION OF A PIEZOELECTRIC ENERGY HARVESTER MOUNTED ON EARDRUM

This chapter begins with a detailed explanation of the first proposed application. The proposed application aims to eliminate/degrade the battery recharging/replacement problem of conventional cochlear implants. After the proposal of the application, modeling, design, and optimization of a piezoelectric energy harvester, which is mounted on eardrum, is explained in detail. This section starts with theory and modeling of energy harvesters. Next, development of an eardrum model is explained. Eventually, at the end of the chapter, developed models are coupled and optimization studies are described.

2.1 Proposed Application: Energy Harvesting Using Eardrum Vibrations

Vibration energy harvesting devices have so far been in the focus of many emerging applications that require an autonomous power supply. Some of these applications are structural health monitoring systems, mobile devices, and customer electronics. Therefore, researchers have striven to develop vibration energy harvesters considering these applications. In this regard, energy harvesters are mostly optimized for frequency band of 30-125 Hz where most industrial or household applications' vibrations occur.

Eardrum is one of the most important auditory system organs, and it converts the acoustic sound pressure variations to vibrations. Thus, it is also a promising area where mechanical vibrations can be converted to electrical energy. The generated electrical energy can be used to supply electronics. However, converting eardrum vibrations to electrical power via an energy harvester has never been studied in the literature. In this thesis, the harvester is hence designed and optimized considering the eardrum dynamics. On the other hand, when an harvester is mounted onto the eardrum, due to comparable dynamic parameters of the harvester and eardrum, the dynamics of the eardrum change considerably. Therefore, proposed method is more suitable for people using cochlear implants, since natural hearing mechanisms are not employed.

Cochlear implants have been used for the treatment of sensorineural hearing loss. They have been used more than 40 years and today implanted in approximately 220.000 individuals worldwide [8]. A cochlear implant consists of 3 main parts. The outer part is composed of electronic devices such as microphone, sound processor, and transmitter, while the inner part consists of implant, which is also an electronic device, and electrode. These electronic parts consume electrical energy, such that the user should replace/recharge the battery of the implant frequently (typically once-twice a day) [9]. Therefore, the users have to carry additional batteries with them. To overcome this problem, an autonomous power supply is required to power up the cochlear implant and eliminate the need of the device for battery. On the other hand, cochlear implant users do not make use of the eardrum vibrations, since electronic components replace all of the natural hearing mechanism. Therefore, the proposed method of harvesting eardrum vibrations can be used to eliminate the battery dependence of the cochlear implant users.

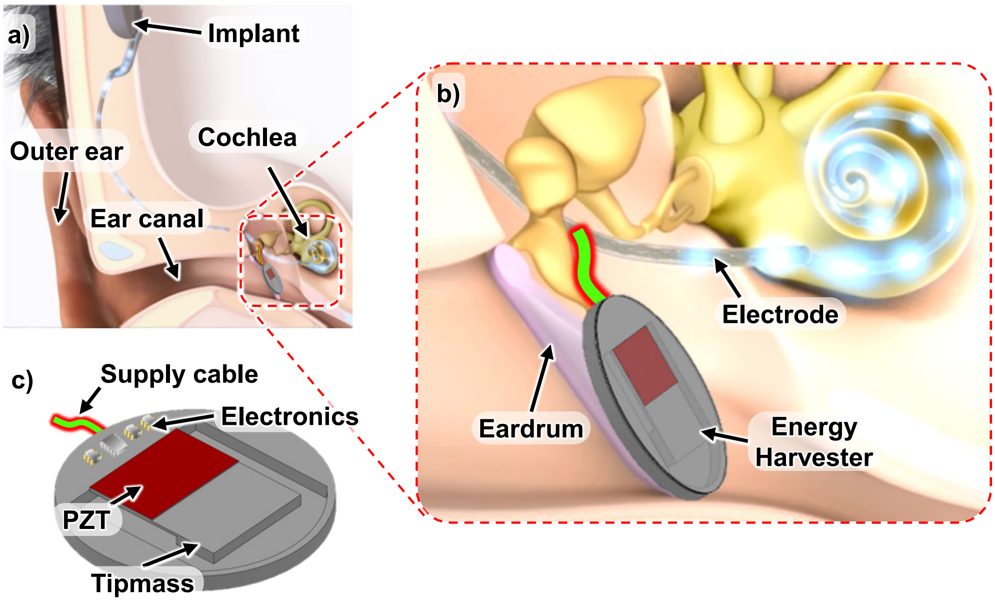

Figure 2.1: The proposed method: converting eardrum vibrations to electricity, a) peripheral auditory system of a cochlear implant user, b) placement of the energy harvester onto the eardrum, c) close-up view of the harvester.

Figure 2.1a conceptually depicts peripheral auditory system (outer ear, middle ear, and inner ear) of a cochlear implant user utilizing the energy harvester mounted on the eardrum. As seen from the figure, the implant is surgically placed under skin and behind the ear. Figure 2.1b shows close-up view of the middle ear. The electrode component of the implant is placed through the cochlea. The harvester is placed onto the eardrum. The harvester converts the available mechanical energy to electrical energy, and provides additional electrical energy to the cochlear implants by connecting the output to the implant via electrode. A single frequency energy harvester is designed (Figure 2.1c), and when this harvester is mounted onto the eardrum, the coupled structure resonates at a predetermined frequency. Various frequencies are considered for the resonance frequency of the coupled structure, which are within the frequency band of daily sounds.

Figure 2.2 shows an audiogram of the daily sounds and it can be seen that 500 Hz to 3000 Hz is one of the most common sound frequency range that is observed during daily life. Therefore, this range is focused during design studies.

2.2 Modeling of Piezoelectric Energy Harvesters

Figure 2.3 shows a typical piezoelectric energy harvester structure. Most of the reported piezoelectric energy harvesters use a cantilever beam with a proof mass to tune the natural frequency of the structure. Usually a piezoelectric layer is bonded around the fixed side of the beam. When the harvester is mounted to a vibrating device or machine, these vibrations will be transferred to the harvester through the vibrations of its base. Thus, the excitation of the base will force the beam to vibrate. The bending of the beam results in alternating tensile and compressive stresses in the piezoelectric layer. Then, depending on the amplitude of the stress, an oscillating voltage output is generated through the piezoelectric layer. Hence, during design, a large enough stress should be enabled through piezoelectric layer for maximum voltage output.

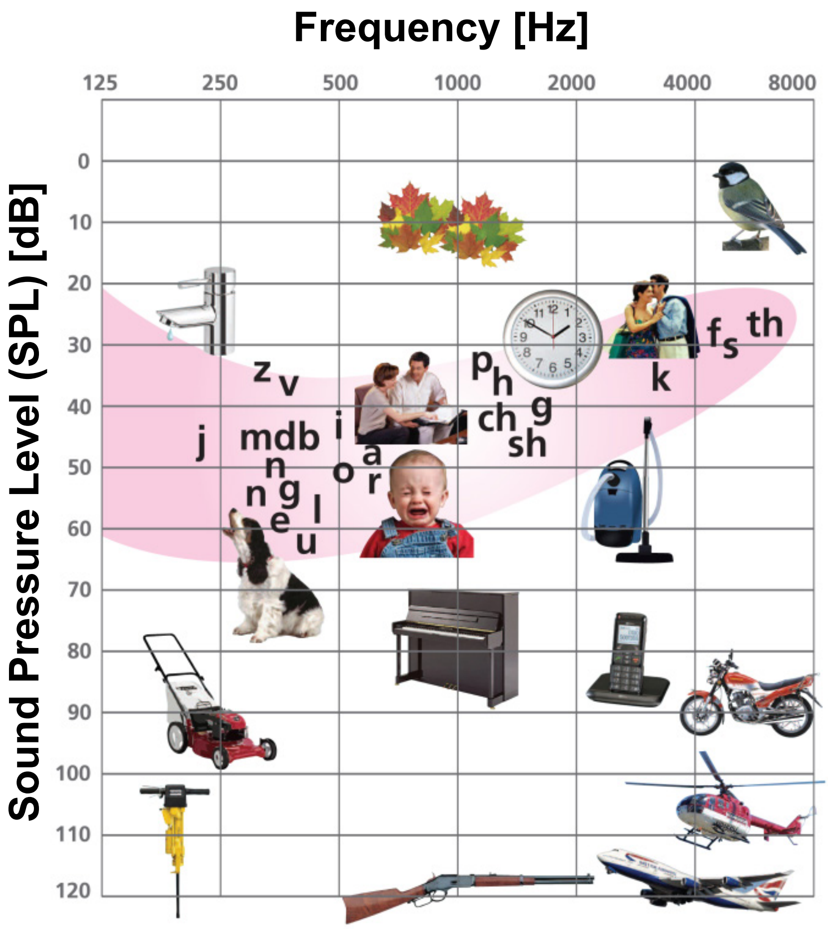

Figure 2.2: Audiogram showing the frequency and decibel of the daily sounds [57].

There are mainly three methods for modeling of piezoelectric energy harvesters. These methods are lumped parameter, distributed-parameter (continuous systems), and finite element analysis. In the following subsections, these methods will be discussed in more detail.

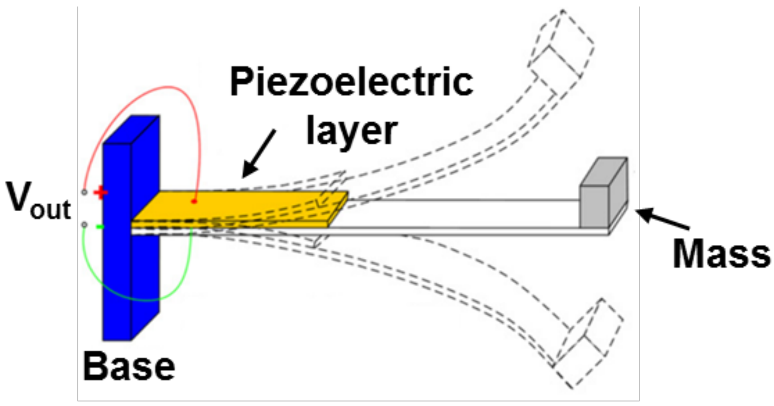

Figure 2.3: Conventional piezoelectric energy harvester design, a fixed-free cantilever beam with tipmass [58].

2.2.1 Lumped Parameter Modeling

Lumped parameter modeling is simplification of the physical system into several lumped discrete elements, which are describing the behavior of the physical system. This modeling approach is widely used for electrical circuits, and is also applicable to piezoelectric energy harvesters. Since piezoceramics can be represented as lumped elements, representing the mechanical characteristics of the harvester with this approach has been a popular method in the literature [59]. In 2002, Flynn *et al.* modeled piezoelectric coupling as a transformer, where transformer relates stress to electric field [60]. In this system, by utilizing a capacitor and a resistor, inherent capacitance and external load resistance of the piezoceramics is modeled. By using piezoelectric constitutive equations [39], the mechanical domain is coupled with the electrical domain. Thus, a transformer relation between these domains and electromechanical model of the piezoelectric energy harvester are obtained by using circuit elements. Roundy *et al.* [15] and duToit *et al.* [61] used this approach for modeling piezoelectric energy harvesters in their study. Figure 2.4 shows the developed circuit representation of the harvester. In this figure, on the mechanical side, stress is used as the across variable and strain as the through variable. Since piezoelectric constant, d, relates stress to electrical voltage, it is easier to utilize stress and strain instead of force and tip displacement. Besides, mechanical properties of the harvester, mass, elasticity, and damping are represented using inductor, capacitor, and resistor, respectively. Geometric constants are also derived in this study, which are relating average stress and average strain to the force applied to the base and the displacement at the tip of the cantilever beam. On the electrical side of the circuitry, R_L is the external resistance load, C_P is the capacitance, and V is the voltage output of the piezoceramics.

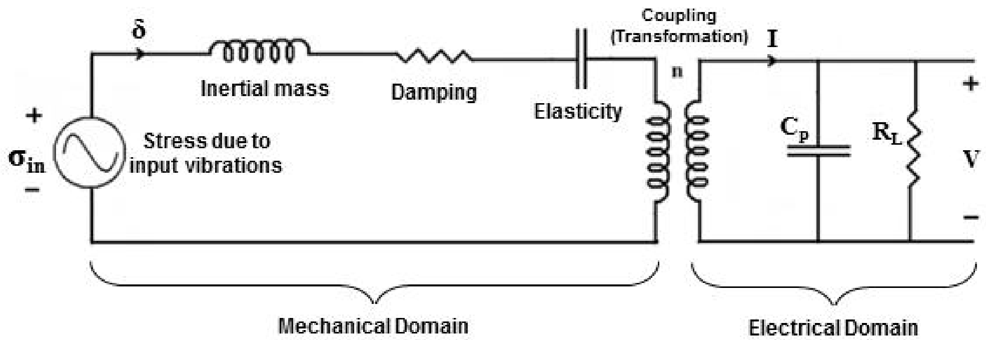

Figure 2.4: Representation of piezoelectric energy harvester with lumped electrical elements [15].

For the mechanical domain, single-degree-of-freedom harmonic base excitation lumped model is widely used in the literature. For this purpose, a point of interest, such as the tip of a cantilever beam, is chosen. The physical system is reduced and represented with lumped parameters of equivalent stiffness, k_{eq}, mass, m_{eq}, and damping, c_{eq}, which are obtained by considering the dynamics of the chosen point. Then, this model is coupled with the electrical domain. Finally, design and optimization studies of the parameters are carried out to maximize the power output [20], [22], [27], [43], [61–63].

Figure 2.5a shows the commonly referred base excitation problem for modeling harvesters. In this model, y(t) is the harmonic base excitation and x(t) is the tip displacement of the cantilever beam. Recently, Erturk *et al.* proposed a correction for the widely referred lumped model [64]. The proposed model is shown in Figure 2.5b, and treats structural and air damping as separate elements, which act on the relative velocity between the base and the mass and the absolute velocity of the mass, respectively. Authors showed the effect of assuming a constant damping in the model by comparing the transmissibility functions of the distributed model and lumped parameter model, and developed a correction factor for the commonly referred lumped parameter model.

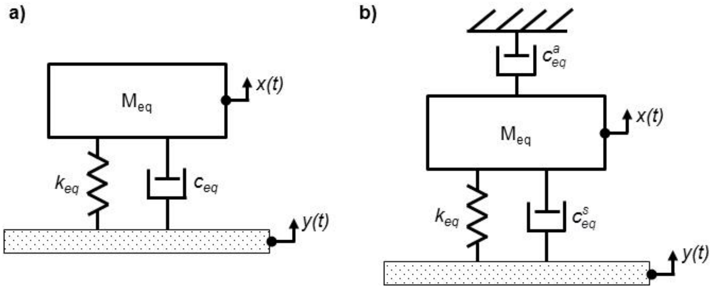

Figure 2.5: Lumped parameter model of the base excitation problem used for representation of vibration-based energy harvesters a) widely referred lumped model, b) modified model representing more precise model of air damping mechanism proposed by Erturk et al. [64].

As depicted in Figure 2.6, the equivalent stiffness of the cantilever beam, k_{eq}, is derived using static deflection of the structure due to a concentrated load at the tip, and its explanation is given in Equation 2.1. In this equation, P represents the applied force at the tip, δ represents the transverse displacement of the tip of the beam, E is the Young's Modulus, I is the second moment of area, and L is the length of the beam.

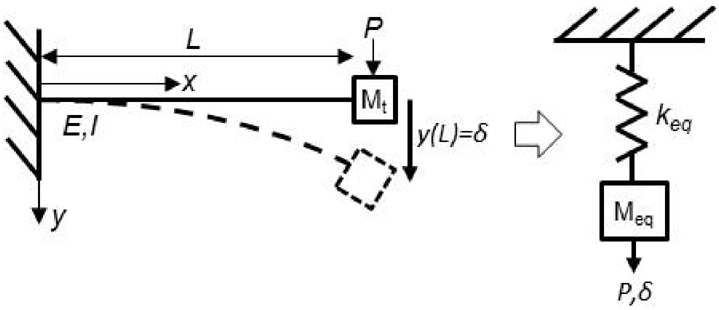

Figure 2.6: Fixed-free type cantilever beam with a tipmass and its lumped model.

The equivalent mass of the cantilever beam, m_{eq}, is obtained using kinetic energy relations [65]. The maximum kinetic energy of the cantilever beam, T_{max}, is found using Equation 2.2. In this equation, m_{beam} represents the mass of the beam, and y(x) is the transverse displacement of the cantilever beam. Note that the transverse velocity, $\dot{y}(x)$, depends on the deflection of the beam, which can be obtained using force-deflection relations. The equation for fixed-free cantilever beam where a concentrated load is applied at the tip is given in Equation 2.3. By replacing the force term in this equation with maximum displacement, δ or y_{max}, equivalent stiffness relations is obtained as given in Equation 2.4.

$$k_{eq} = \frac{P}{\delta} = \frac{3EI}{L^3} \tag{2.1}$$

$$T_{\max} = \frac{1}{2}\int_0^L \frac{m_{beam}}{L}\{\dot{y}(x)\}^2\,dx \tag{2.2}$$

$$y(x) = \frac{Px^2}{6EI}(3L - x) \tag{2.3}$$

$$y(x) = \frac{y_{\max}\,x^2}{2L^3}(3L - x) \tag{2.4}$$

After obtaining y(x), T_{max} can be simplified as given in Equation 2.5. On the other hand, by considering the lumped model, T_{max} can also be written as in Equation 2.6. By comparing Equation

2.5 and Equation 2.6, the equivalent mass of the cantilever beam can be obtained. For many cases, a tipmass is used for energy harvesting cantilever beams to increase power levels and resonate the structure at desired frequency. The effect of tip mass is usually assumed as a concentrated load at the tip, and Equation 2.7 is the equivalent mass, m_{eq}, of the cantilever beam with a tipmass, M_t.

$$T_{\max} = \frac{m_{beam}}{2L}\left(\frac{\dot{y}_{\max}}{2L^3}\right)^2 \int_0^L (3x^2L - x^3)^2\,dx = \frac{1}{2}\left(\frac{33}{144}m_{beam}\right)\dot{y}_{\max}^2 \tag{2.5}$$

$$T_{\max} = \frac{1}{2}m_{eq}\dot{y}_{\max}^2 \tag{2.6}$$

$$m_{eq} = \frac{33}{140}m_{beam} + M_t \tag{2.7}$$

The advantage of lumped modeling is that it gives an initial insight on the problem. Besides, the electrical representation of the whole system is convenient for developing the rectifying circuitry for the harvesters, since model can be directly integrated into electronic circuit simulation programs. On the other hand, this modeling approach is an approximation and limited to a single vibration mode. Therefore, dynamic mode shapes of the harvester, strain distribution and its effects on voltage output of the piezoceramics cannot be considered during modeling [41].

In the frame of this thesis, a coupled structure consisting of a piezoelectric energy harvester and a membrane is aimed to be modeled. Therefore, effect of higher-order modes should be considered during modeling. Hence, lumped parameter modeling cannot be used. Besides, a model providing a more accurate output voltage value is desired for optimization purposes.

2.2.2 Distributed Parameter Modeling

Recently, distributed parameter modeling received great attention due to the issues presented for the lumped parameter modeling [66–70]. Especially, when modeling cantilever beams without tipmass, the forcing amplitude used in the base excitation problem is greatly dependent on the distributed mass of the beam [41]. However, this contribution of the beam mass is neglected in lumped parameter modeling, which considerably affects the dynamics of the problem.

Initially, as an improved model of the lumped parameter model of piezoelectric actuation, Rayleigh-Ritz discretization is derived by Hagood *et al*. [71]. This type of model can be considered as a transition from lumped parameter model to a distributed parameter model, since it is a spatially discretized model of the distributed parameter model. This approach is applied to the piezoelectric energy harvesters by Sodano *et al*. [72] and duToit *et al*. [61]. This model gives a more accurate representation of the system when compared to the lumped parameter model. However, this approach is still an approximation of the physical system, and requires much more computational power and time in order to get accurate results [64].

Distributed parameter modeling attempts of piezoelectric energy harvesters are based on incorporating the piezoelectric constitutive equations into the Euler-Bernoulli beam theory equations. In 2004, Lu *et al*. developed a simple analytical model for analysis of a piezoelectric energy harvester [67]. In this study, the output power and the conversion efficiency are optimized using the model developed. The derived formula for time-averaged electrical power of single piezoelectric layer is given in Equation 2.8:

$$\overline{P} = \frac{\omega^2 b^2 h^2 e_{31}^2 \left[\varphi(l_0) - \varphi(l_1)\right]^2}{8(1 + bL\varepsilon_{33}\dfrac{\omega R}{\Delta})} \tag{2.8}$$

and relates tip displacement of the cantilever to the electrical power. In this equation, b and h are the width and thickness of the beam, L and Δ are length and thickness of piezoelectric layer, e_{31} is piezoelectric constant in 31 coupling direction, ε_{33} is dielectric constant, and φ(x,t) is flexibility of the beam, thus $[\varphi(l_0)-\varphi(l_1)]$ is the difference of bending slopes at both ends of the piezoelectric layer. However, as stated by Erturk *et al.*, this formulation does not include information on higher vibration modes, and lacks resonance phenomena since expansion theorem is not included in the derivation [73].

Lin *et al*. modeled a micro-scale piezoelectric energy harvester using Euler-Bernoulli beam theory with a lumped mass at the tip of the beam [68]. They used well-known fourth-order differential equation for transverse vibrations of cantilever beams as given in Equation 2.9, where z(x,t) is the transverse displacement of the point that has distance x from the fixed end of the beam, E is modulus, I is the second moment of area, m is mass per length, b is the damping factor, and f(x,t) is the force per unit length. Then, method of separation of variables is employed (Equation 2.10), and eigenvalues of the beam are determined considering the lumped proof mass, M, at the free end. In order to obtain the response of the structure, f(x,t) is represented as a harmonic force as in Equation 2.11, where $z_b=z_{b0}\cos(\omega t)$ is the base displacement. After rearranging Equation 2.9, and satisfying orthogonality condition for a beam with lumped mass at the free end, the response of the cantilever beam is obtained. By using the response, strain conditions around the piezoelectric layer are evaluated. Eventually, using piezoelectric relations, strain-induced current through piezoelectric layer is calculated as given in Equation 2.12. In this equation, Q is the strain-induced charge, d_{31} is the piezoelectric constant, E_P is the Young's Modulus of piezoelectric layer, z_N and z_P are height of the neutral axis of the beam and the center of the piezoelectric layer, respectively, w_d is the width of the beam, L_P is the length of the piezoelectric layer, and E_z is the electric field in z-direction. Authors also used this relation in a lumped circuit model to get the optimum load resistance for maximum power output.

$$EI\frac{\partial^4 z(x,t)}{\partial x^4} + m\frac{\partial^2 z(x,t)}{\partial t^2} + b\frac{\partial z(x,t)}{\partial t} = f(x,t) \tag{2.9}$$

$$z(x,t) = \sum_{n=1}^{\infty} X_n(x)T_n(t) \tag{2.10}$$

$$f(x,t) = m\ddot{z}_b = mz_{b0}\omega^2\cos(\omega t) \tag{2.11}$$

$$I = \frac{\partial Q}{\partial t} = j\omega Q = j\omega\left(d_{31}E_p(z_N - z_P)w_d\left.\frac{\partial z(x,t)}{\partial x}\right|_{x=L_P} + \varepsilon_P E_Z w_d L_P\right) \tag{2.12}$$

Backward coupling behavior of piezoelectric materials is an important issue, and should be considered during modeling via piezoelectric constitutive equations. However, in the study presented by Lin *et al*. [68] and Chen *et al*. [70], they did not integrate the behavior of backward piezoelectric effect, instead oversimplified this relation as a viscous damping in the model [41]. Thus, vibration of the beam is not affected due to power generation from piezoelectric layer, thus violating the piezoelectric constitutive equations [73]. Besides, as the authors of the study, Lin *et al*., mentioned, the developed model is not sufficient for modeling of the cantilever beams where the length is not far longer than the width of the structure, which is the case for many micro-scale harvesters [68].

Other issues of distributed parameter modeling are as follows: assuming the force due to base excitation as a tip force [74], using static piezoelectric equations [68], and incorporating static deflection patterns into equations of a dynamic vibration problem [75]. More detailed discussions on these issues can be found in [73].

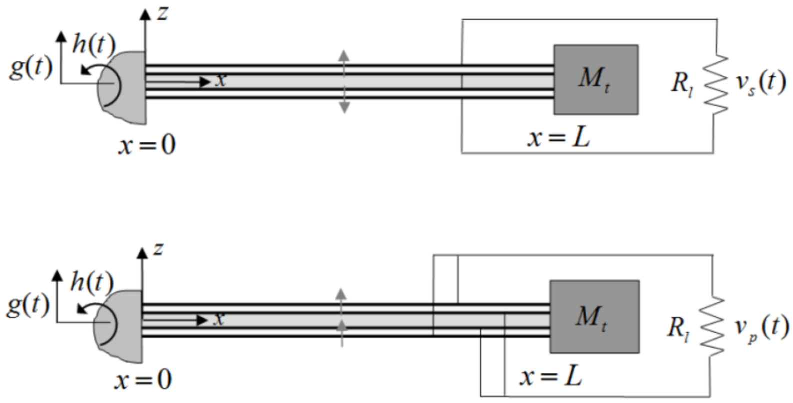

Figure 2.7: Bimorph piezoelectric energy harvesters with a) series connection, b) parallel connection [64].

Recently, Erturk and Inman developed a closed-form distributed parameter solution based on Euler-Bernoulli beam theory for unimorph and bimorph (for both series and parallel configuration (Figure 2.7)) type of piezoelectric energy harvesters [76], [77]. Authors also start derivations with the differential equation for cantilever beams as in Equation 2.9. However, they used bending moment term, M(x,t), instead of the fourth order derivative of the transverse displacement term. Besides, a more concise representation of damping terms are employed as mentioned in Section 2.2.1. The governing differential equation of motion is written as in Equation 2.13:

$$\frac{\partial^2 M(x,t)}{\partial x^2} + c_s I \frac{\partial^5 z_{rel}(x,t)}{\partial x^4 \partial t} + c_a \frac{\partial w_{rel}(x,t)}{\partial t} + m \frac{\partial^2 z_{rel}(x,t)}{\partial t^2} = - m \frac{\partial^2 z_b(x,t)}{\partial t^2} - c_a \frac{\partial w_b(x,t)}{\partial t} \tag{2.13}$$

where z_{rel} and z_b represents the relative displacement between the beam and its base, m is the mass per unit length, c_s is the structural damping coefficient, c_a is the air damping coefficient, and I is the area moment of inertia. Bending moment, M(x,t), is obtained by combining piezoelectric constitutive equations with the integral of first moment of the stress distribution. Thus, the bending moment term, M(x,t) is obtained as in Equation 2.14; thus, coupling behavior of piezoelectric materials is integrated into the Euler-Bernoulli beam equation [64].

$$M(x,t) = EI \frac{\partial^2 z_{rel}(x,t)}{\partial x^2} + \tau v(t) \tag{2.14}$$

In Equation 2.14, v(t) is the voltage across the piezoelectric layer and τ is the coupling term, which is written as [64]:

$$\tau = -\frac{E_p d_{31} b}{2h_p}(h_c^2 - h_b^2) \tag{2.15}$$

where E_p is the modulus of piezoelectric layer, d_{31} is the piezoelectric constant, b is the width of the beam, h_b and h_c are positions of the bottom and top of the piezoelectric layer, and h_p is the thickness of the piezoelectric layer. Consequently, authors derive closed-form expressions of unimorph and bimorph structures for current, voltage, and power outputs, and validated them experimentally.

Effects of external load resistance on the resonance frequency can also be observed with this model, as well as open and short circuit behaviors.

The closed-form equations developed by Erturk and Inman matches closely with the experiments conducted using macro-scale cantilever types with length/width ratios ranging from 3.7 to 6.7. However, many MEMS cantilever structures have relatively low length/width ratio (as low as 1). Thus, assuming the structure as a 2-D plate instead of a 1-D structure might be a more concise assumption for MEMS cantilever structures. Besides, Euler-Bernoulli beam theory works pretty well when uniform structures are considered. However, most of the MEMS cantilever structures employ tipmasses with lengths comparable to the length of the beam, and usually piezoelectric layer is not uniform throughout the beam length. When length of the tipmass is comparable to the beam length, stiffness behavior of the cantilever changes considerably [78]. However, the models developed with distributed modeling approach assumes the tipmass as a concentrated load, and ignore its dimensions [69]. Thus, structural characteristics of the micro-scale cantilever structure with tipmass cannot be modeled accurately with this model. Furthermore, when length of the piezoelectric layer is lower than the length of the beam, the solution should be rearranged considering the beam as a two-segment structure. To model the discontinuity, piecewise differential equations are used along with four additional compatibility conditions, which should be satisfied at the point of discontinuity. Then, with four boundary conditions for the ends of the cantilever, 8x8 coefficient matrix should be solved. Since this coefficient matrix include hyperbolic and trigonometric functions, resulting matrix is usually ill-conditioned, making the problem much more complicated. Another disadvantage of using Euler beam theory is that the rotary and shear deformations are neglected. This would result in missing of torsional vibration modes, which might be abundant for cantilevers with large tipmasses and low length/width ratio.

In this thesis, a MEMS piezoelectric energy harvester is aimed to be designed which is mounted onto the eardrum. When micro-scale cantilever beams with desired frequency range of up to 5000 Hz are designed, usually length/width ratio of these structures is relatively low compared to their macro-scale counterparts. Besides, the tipmass of the structures should not be considered as a concentrated mass, since the length of tipmasses is usually comparable to the beam length for applications within the mentioned frequency range. Lastly, piezoelectric layer in most MEMS harvesters is not coated through the whole length of the beam. Therefore, they should be considered as two-segment cantilever beams if one seeks solution through distributed parameter modeling approach.

2.2.3 Finite Element Modeling

As discussed in previous sections, lumped parameter modeling and distributed parameter modeling are not suitable for designing MEMS piezoelectric energy harvesters. Besides, many engineering problems cannot be solved using analytical problems due to the complexity of boundary conditions, material properties, and structure itself. Therefore, another modeling approach, finite element modeling (FEM) is considered, which is widely used in both industry and academia. FEM is a numerical method utilizing variational methods to find approximate solutions to boundary value problems where the structure is represented by an assembly of its subdivisions called finite elements [79]. Recently, FEM received great attention from many fields, including various applications ranging from nano-scale to micro-scale [80–90]. Using these finite elements, FEM converts partial differential equation problem to a set of linear equations as given in Equation 2.16, where [K] is the stiffness matrix, {q} is the nodal displacement vector, and {F} is the nodal vector force. Besides, this method is widely used for modeling magnetic [91–93] and piezoelectric [84], [94–97] transducers.

$$[K]\{q\} = \{F\} \tag{2.16}$$

The advantage of FEM modeling is that structural features of the harvester can be considered without making any assumptions as in the lumped and distributed parameter models. Effects of tipmass, when its length is comparable to the beam length, and discontinuity for two-segment type of harvester structures do not require special treatment in the model. Unlike other methods, in FEM it is possible to observe the effect of each parameter. Thus, FEM provides a better solution for parametric modeling, which makes them a promising tool for optimization purposes.

Various FEM programs are available for structural problems. Among these choices, due to its wide usage in piezoelectric transducers, ease of use, speed due to code based working environment, and its built-in optimization tool, ANSYS is preferred for the FEM simulations in this thesis.

In this thesis, finite element modeling has been chosen due to several reasons. First, the harvester dimensions have several constraints due to the desired application and fabrication issues: instead of an Euler-Bernoulli type of cantilever beam, a plate-like structure is to be considered. Secondly, large tipmass should be used, and there are discontinuities in the cross-section, which can be handled by FE modeling. Third, anisotropic material properties of the piezoelectric material can be directly integrated into the solution. Lastly, after modeling the harvester it will be coupled with another structure (eardrum). In this regard, it is more convenient to use FEM modeling approach instead of lumped parameter and distributed parameter modeling approaches.

2.3 Modeling and Design of the MEMS Piezoelectric Energy Harvester Using FEM

Figure 2.8 shows schematic of the proposed MEMS piezoelectric energy harvester. Footprint of the harvester is selected considering the desired application. A typical eardrum has an elliptic shape with diameters of 10 mm and 9 mm [98]. Thus, footprint of the harvester is chosen as 5x5 mm^2. Then, cantilever beam is fixed to the casing and tipmass is placed at the free end. Piezoelectric material is placed around the fixed side of the cantilever in order to induce more strain during vibrations.

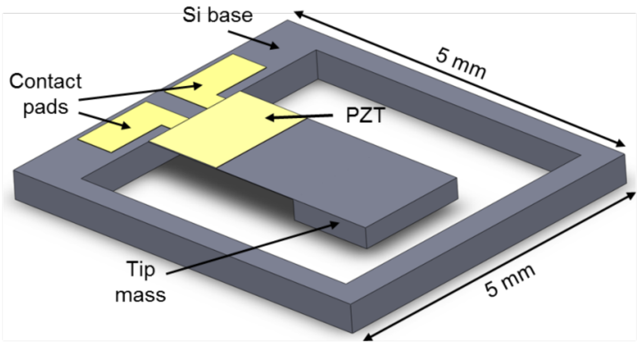

Figure 2.8: Proposed MEMS piezoelectric energy harvester.

A parametric MEMS piezoelectric energy harvester model is developed using ANSYS Parametric Design Language (APDL). Considered parameters during design can be seen in Figure 2.9 where L_B is the total beam length, L_P is the piezoelectric material length, L_{TM} is the tipmass length, W_B is the beam width, T_P, T_B, and T_{TM} are thickness of the piezoelectric material, beam, and tipmass, respectively. Instead of considering only cantilever structure, case is also included in the model. Therefore, developed model can account for the stiffness characteristics of the anchor, and can be directly mounted onto the eardrum model as in the desired application; thus, realistic boundary conditions can be applied.

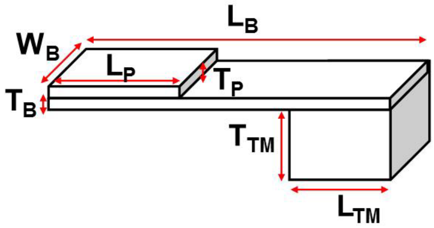

Figure 2.9: Dimensions of the MEMS piezoelectric energy harvester.

Two different element types are used during simulations, namely, SOLID186 and SOLID226 (Figure 2.10). These elements have various shape options and it should be considered during simulations, because it affects meshing quality of the structure. Former element is a typical one used for modeling 3-D solid structures, while the latter one is a coupled-field element. Both of them have a brick shape by default, and have tetrahedral, prism, as well as pyramid option. Depending on the desired mesh quality of the each region within the structure, available shape options of the element are used to meet expectations. Both elements have 20 nodes. SOLID186 has three DOFs per node: translation in the x, y, and z directions. Besides, this element also supports plasticity, stress stiffening, large strain, and large deflection capabilities. On the other hand, SOLID226 can be used for coupling of various fields, such as structural-thermal, piezoresistive, piezoelectric, thermal-electric, structural-thermoelectric, and thermal-piezoelectric. It has up to five DOFs per node, translations in x, y, z directions, temperature, and voltage. Thus, this element is widely used for piezoelectric applications, as well as thermoelectric due to its capability of modeling Seebeck, Peltier, Joule heating effects. Another advantage of using these 3-D elements is that they support anisotropic materials. Silicon is the most widely used material in MEMS fabrication processes. This material has widely known anisotropic properties, and considering it as an isotropic material would lead incorrect results [89]. The other material that is used during simulations has piezoelectric properties. Similar to silicon, this material also exhibits anisotropic properties [99] and should be modeled accordingly.

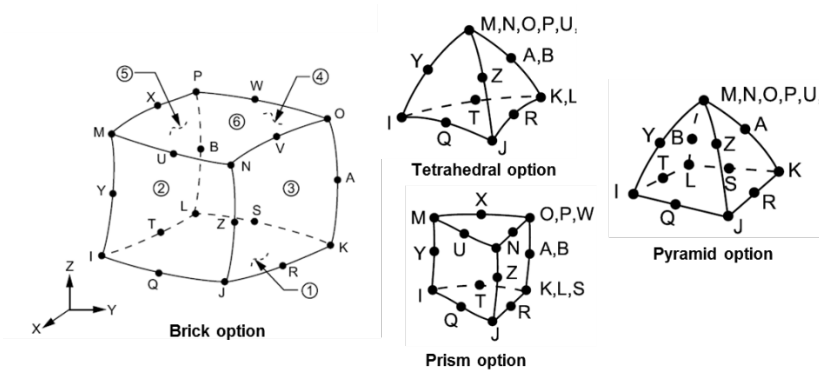

Figure 2.10: SOLID186 structural solid and SOLID226 coupled-field solid geometry with various shape options [100].

After constructing geometry and selecting elements, material properties are input to the model. As mentioned earlier, silicon is not an isotropic material [89], [101–103]. Thus, its elastic behavior depends highly on the orientation of the structure. However, there are various Young's Modulus, E, values for silicon, which range from 130 to 188 GPa. In 2010, Stanford researchers Hopcroft *et al.* conducted a detailed analysis on modeling of silicon material for MEMS structures with a focus on FEM [89]. They stated that if anisotropic crystalline material properties are not considered, two different designs might differ up to 45% in obtained natural frequencies.

Generally, two types of silicon wafers are used in MEMS processes. Depending on the crystal orientation, these wafers are named as (100) and (111). Crystal directions of (100) wafer is shown in

Figure 2.11, and depending on the orientation or placement of the device on the wafer, elastic constants should be used accordingly. Figure 2.12 shows the Young's Modulus and Poisson's ratio values considering the wafer directions.

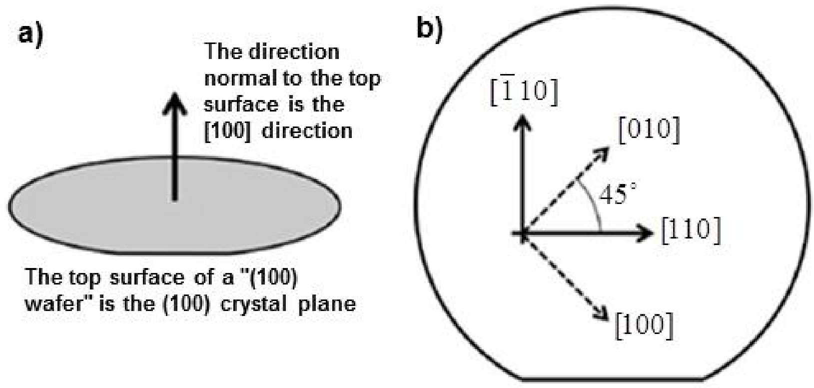

Figure 2.11: Crystal directions of (100) wafer, a) isometric view and [100] direction, b) flat direction and axes [89].

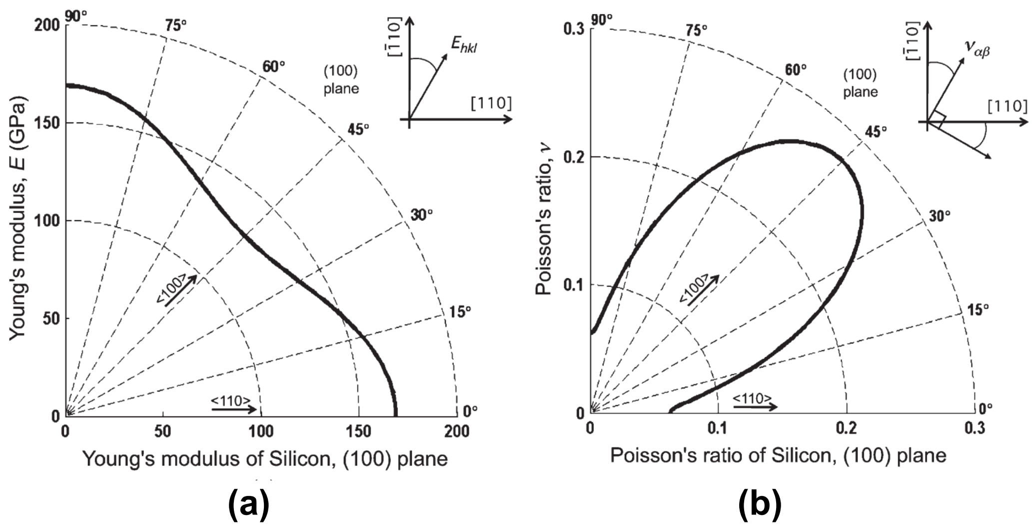

Figure 2.12: a) Young's Modulus, b) Poisson's ratio value with respect to wafer's crystal directions [89], [104–107].

Elasticity of materials can be described using the relation between stress, *σ*, and strain, *ε*, [108]. This relation can be described using compliance, S, or stiffness, C, as given in Equation 2.17. This equation leads to a fourth rank tensor (3^4=81 terms) for anisotropic materials. Luckily, silicon exhibits combination of cubic symmetry. Besides, the equivalence of shear conditions also helps us to describe the material behavior with three independent components. Therefore, elastic properties of the silicon can be described using orthotropic material constants. Simplified form of Equation 2.17 for orthotropic materials is given in Equation 2.18 using stiffness matrix, C. Equation 2.19 is obtained when Young's Modulus and Poisson's ratio values are used considering (100) type silicon wafer [89].

$$\sigma = C\varepsilon \qquad \text{or} \qquad \varepsilon = S\sigma \tag{2.17}$$

$$\begin{bmatrix}\sigma_1\\ \sigma_2\\ \sigma_3\\ \sigma_4\\ \sigma_5\\ \sigma_6\end{bmatrix}=\begin{bmatrix}\dfrac{1-\upsilon_{yz}\upsilon_{zy}}{E_yE_z\Delta} & \dfrac{\upsilon_{yx}+\upsilon_{yz}\upsilon_{zy}}{E_yE_z\Delta} & \dfrac{\upsilon_{zx}+\upsilon_{yx}\upsilon_{zy}}{E_yE_z\Delta} & 0 & 0 & 0\\ \dfrac{\upsilon_{xy}+\upsilon_{xz}\upsilon_{zy}}{E_zE_x\Delta} & \dfrac{1-\upsilon_{zx}\upsilon_{xz}}{E_zE_x\Delta} & \dfrac{\upsilon_{zy}+\upsilon_{zx}\upsilon_{xy}}{E_zE_x\Delta} & 0 & 0 & 0\\ \dfrac{\upsilon_{xz}+\upsilon_{xy}\upsilon_{yz}}{E_xE_y\Delta} & \dfrac{\upsilon_{yz}+\upsilon_{xz}\upsilon_{yx}}{E_xE_y\Delta} & \dfrac{1-\upsilon_{xy}\upsilon_{yx}}{E_xE_y\Delta} & 0 & 0 & 0\\ 0 & 0 & 0 & G_{yz} & 0 & 0\\ 0 & 0 & 0 & 0 & G_{zx} & 0\\ 0 & 0 & 0 & 0 & 0 & G_{xy}\end{bmatrix}\begin{bmatrix}\varepsilon_1\\ \varepsilon_2\\ \varepsilon_3\\ \varepsilon_4\\ \varepsilon_5\\ \varepsilon_6\end{bmatrix} \tag{2.18}$$

$E_x = E_y = 169\ GPa$ $\qquad$ $E_z = 130\ GPa$

$\upsilon_{yz} = 0.36$ $\qquad$ $\upsilon_{zx} = 0.28$ $\qquad$ $\upsilon_{xy} = 0.064$

$G_{yz} = G_{zx} = 79.6\ GPa$ $\qquad$ $G_{xy} = 50.9\ GPa$

$$\begin{bmatrix}\sigma_1\\ \sigma_2\\ \sigma_3\\ \sigma_4\\ \sigma_5\\ \sigma_6\end{bmatrix}=\begin{bmatrix}194.5 & 35.7 & 64.1 & 0 & 0 & 0\\ 35.7 & 194.5 & 64.1 & 0 & 0 & 0\\ 64.1 & 64.1 & 165.7 & 0 & 0 & 0\\ 0 & 0 & 0 & 79.6 & 0 & 0\\ 0 & 0 & 0 & 0 & 79.6 & 0\\ 0 & 0 & 0 & 0 & 0 & 50.9\end{bmatrix}\begin{bmatrix}\varepsilon_1\\ \varepsilon_2\\ \varepsilon_3\\ \varepsilon_4\\ \varepsilon_5\\ \varepsilon_6\end{bmatrix} \tag{2.19}$$

Similarly, piezoelectric materials exhibit anisotropic properties. However, due to the polarization process through the thickness, piezoelectric materials exhibit plane symmetry, and thus can be described using orthotropic relations similar to silicon. This symmetry feature is used to reduce the number of independent coefficients used in the constitutive equations and material properties tensor [109]. Therefore, considering symmetry plane of the piezoceramics as 12-plane, constitutive equations can be simplified as given in Equation 2.20 and Equation 2.21.

$$\begin{bmatrix}S_1\\ S_2\\ S_3\\ S_4\\ S_5\\ S_6\end{bmatrix}=\begin{bmatrix}s_{11} & s_{12} & s_{13} & 0 & 0 & 0\\ s_{12} & s_{11} & s_{13} & 0 & 0 & 0\\ s_{13} & s_{13} & s_{33} & 0 & 0 & 0\\ 0 & 0 & 0 & s_{55} & 0 & 0\\ 0 & 0 & 0 & 0 & s_{55} & 0\\ 0 & 0 & 0 & 0 & 0 & s_{66}\end{bmatrix}\begin{bmatrix}T_1\\ T_2\\ T_3\\ T_4\\ T_5\\ T_6\end{bmatrix}+\begin{bmatrix}0 & 0 & d_{31}\\ 0 & 0 & d_{31}\\ 0 & 0 & d_{33}\\ 0 & d_{15} & 0\\ d_{15} & 0 & 0\\ 0 & 0 & 0\end{bmatrix}\begin{bmatrix}E_1\\ E_2\\ E_3\end{bmatrix} \tag{2.20}$$

$$\begin{bmatrix}D_1\\ D_2\\ D_3\end{bmatrix}=\begin{bmatrix}0 & 0 & 0 & 0 & d_{15} & 0\\ 0 & 0 & 0 & d_{15} & 0 & 0\\ d_{31} & d_{31} & d_{33} & 0 & 0 & 0\end{bmatrix}\begin{bmatrix}T_1\\ T_2\\ T_3\\ T_4\\ T_5\\ T_6\end{bmatrix}+\begin{bmatrix}\varepsilon_{11}^T & 0 & 0\\ 0 & \varepsilon_{11}^T & 0\\ 0 & 0 & \varepsilon_{33}^T\end{bmatrix}\begin{bmatrix}E_1\\ E_2\\ E_3\end{bmatrix} \tag{2.21}$$

Table 2.1: 3-D PZT-5A piezoceramics material properties used in simulations (where ε_0=8.854 pF/m) [41], [110–112].

s_{11}^E	16.40	pm^2/N	d_{31}	-171	pm/V
s_{12}^E	-5.74		d_{33}	374	
s_{13}^E	-7.22		d_{15}	584	
s_{33}^E	18.80		$\varepsilon_{11}^T / \varepsilon_0$	1730	-
s_{55}^E	47.50		$\varepsilon_{33}^T / \varepsilon_0$	1700	
s_{66}^E	44.30				

SOLID226 element is used for variety of coupling finite element analysis. When 1001 option of the element is chosen, it can be used to integrate the piezoelectric constitutive equations into simulations. This element can be used within static, modal, harmonic, and transient analysis when piezoelectric option is enabled. Besides, upon enabling piezoelectric option, orthotropic material properties are required to define material type, as well as piezoelectric coupling and dielectric coefficients [100]. Piezoelectric material properties are supplied by the manufacturers and are mostly available in the literature [41], [110–112]. Among variety of material options, PZT-5A and PZT-5H are the most commonly used. In this regard, during simulations PZT-5A is considered due to its superior properties (high Curie temperature and high piezoelectric strain coefficient) and availability, which will be discussed in more detail in the Chapter 3. Material properties of PZT-5A are given in Table 2.1. However, piezoelectric material properties supplied from manufacturers are not compatible with the ANSYS piezoelectric material model [113]. ANSYS requires input piezoelectric data to be compatible with the stress, T, based constitutive equations as given in Equation 2.22. Therefore, in order to compute appropriate inputs, a translation procedure through the piezoelectric constitutive equations is required. Using strain, *S*, based constitutive equations, Equations 2.23, 2.24, and 2.25 can be written. As a result, the input values required by ANSYS (c^E, ε^S, e) can be written by comparing Equation 2.22 with Equations 2.24 and 2.25. Obtained relationships are given in Equations 2.26, 2.27, and 2.28. After obtaining the required material properties, a macro-scale piezoelectric energy harvester prototype is manufactured to verify the model as will be discussed in next section.

$$\begin{Bmatrix} T \\ D \end{Bmatrix} = \begin{bmatrix} c^E & -e \\ e^t & \varepsilon^S \end{bmatrix} \begin{Bmatrix} S \\ E \end{Bmatrix} \tag{2.22}$$

$$\{S\} = \left[s^E\right]\{T\} + [d]\{E\} \tag{2.23}$$

$$\{T\} = \left[s^E\right]^{-1}\{S\} - \left[s^E\right]^{-1}[d]\{E\} \tag{2.24}$$

$$\{D\} = [d]^t\left[s^E\right]^{-1}\{S\} + \left(\left[\varepsilon^T\right] - [d]^t\left[s^E\right]^{-1}[d]\right)\{E\} \tag{2.25}$$

$$\left[c^E\right] = \left[s^E\right]^{-1} \tag{2.26}$$

$$\left[\varepsilon^S\right] = \left[\varepsilon^T\right] - [d]^t\left[s^E\right]^{-1}[d] \tag{2.27}$$

$$[e] = \left[s^E\right]^{-1}[d] \tag{2.28}$$

After modeling piezoelectric material with the compatible material properties, structure is meshed. During meshing, it is important to select compatible elements for the surfaces in contact, since mesh patterns of the surfaces should be similar. Chosen elements, SOLID226 and SOLID186 are both 3-D 20-node brick elements. Thus, their mesh capabilities are similar to each other. Developed parametric piezoelectric energy harvester model and its meshed images are shown in Figure 2.13. More discussion about mesh size can be found in Section 2.6.

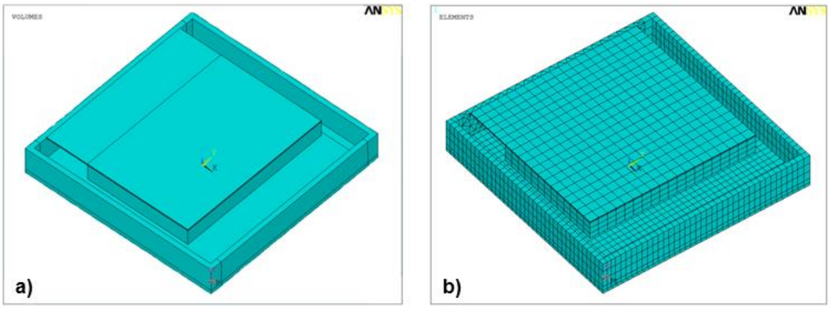

Figure 2.13: Developed parametric MEMS piezoelectric energy harvester model using FEM program, a) unmeshed, b) meshed.

2.4 Verification of the Developed Piezoelectric Material Model

After converting the material properties to a compatible form to be used in the FE program, a macro-scale piezoelectric energy harvester prototype is developed to verify the material model [114–116]. For the development of the prototype, PZT-5A and brass are used as the piezoelectric material and the cantilever structure, respectively. Manufactured prototype is shown in Figure 2.14. During manufacturing of the harvester, conductive epoxy is used to make connection from the bottom of the piezoelectric material. A fixture is designed to hold the structure and connect to the upper and lower surfaces of the piezoelectric material. Dimensions of the manufactured harvester are given in Table 2.2.

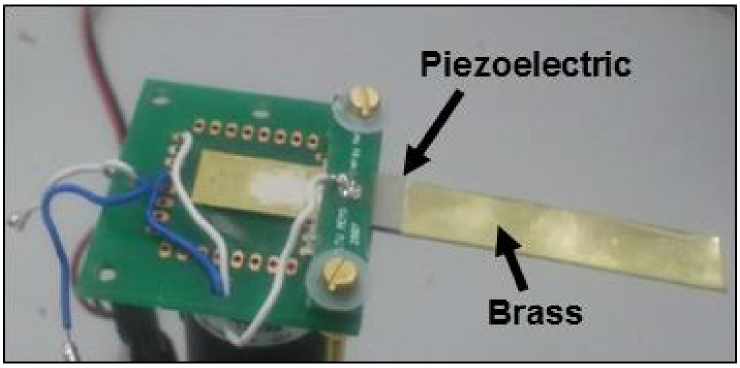

Figure 2.14: Manufactured macro-scale piezoelectric energy harvester prototype [114–116].

Experiment is conducted by mounting the harvester on a shaker. Base displacement of 0.1 mm is given to the structure while sweeping the frequency of vibrations. Damping ratio of 0.095 is obtained by observing bandwidth of electrical output of the piezoelectric material, and used as an input for the simulations [117]. After frequency-sweep analysis, the harvester is simulated with FEM program. Figure 2.15 shows the comparison of the experimental and simulation results of the generated voltage around the natural frequency of the structure. Experimental results showed that natural frequency of the structure is at 109 Hz and 64 V is generated from the piezoelectric material. On the other hand, natural frequency of the simulated structure is at 114 Hz and it can generate 63.7 V at its natural frequency. Therefore, a close-match is obtained for the generated voltage and less than 5% error for the natural frequency even though some of the structural features (e.g. bonding layer) of the harvester were not included in the simulations and coarse mesh (one element through the thickness of the piezoelectric material) of the structure is utilized during simulations. Furthermore, a decrease in the error up to 3% was observed by doubling the node numbers. However, this model took considerably more time for computations and was not used during simulations. Consequently, this study shows that developed piezoelectric material FE model can be used during design and optimization studies of the micro-scale energy harvester. For further improvements of the FE model, model updating strategies can be used [118].

Table 2.2: Dimensions of the manufactured harvester.

	Parameter	Dimension [mm]
Structural layer	*Length*	48.5
	Width	10
	Thickness	0.4
PZT	*Length*	7
	Width	10
	Thickness	0.5

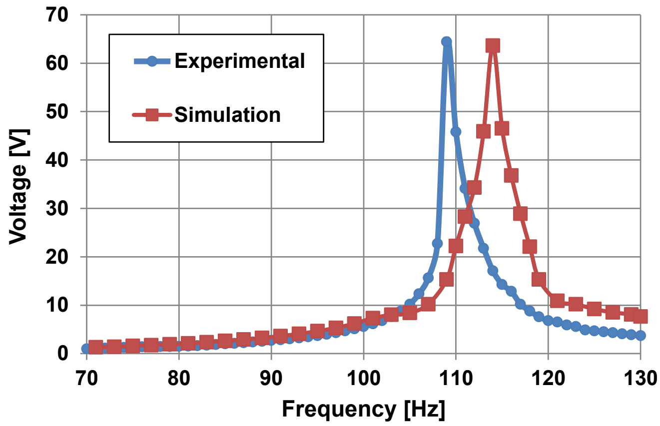

Figure 2.15: Comparison of voltage output versus frequency plot of the experimental results and simulations.

2.5 Modeling of the Eardrum

In the proposed application, the harvester is desired to be mounted onto the eardrum, and it is important to integrate these structures. In Section 2.3, development of the 3-D FE model of the harvester is explained in detail. Accordingly, a FE model of the eardrum is developed in this section. This model will be used during coupling of the harvester and the eardrum structures.
Figure 2.16 shows the peripheral auditory system. The peripheral auditory system consists of outer ear, middle ear, and the inner ear. Passing through these parts, acoustic sound pressure waves are converted to electrical signals, which are send to the brain. Among these parts, eardrum (tympanic membrane) of the middle ear is of key importance, since it transforms acoustic pressure waves into vibrations.

Modeling studies of eardrum dates back to 1800s. First, Helmholtz modeled eardrum using distributed parameter modeling approach, and his theory is based on a curved membrane theory [120].

In 1941, von Bèkesy conducted experiments using capacitive probes for measuring the displacements of the vibrating human eardrum [121]. At the end of this study, researchers conclude that the eardrum

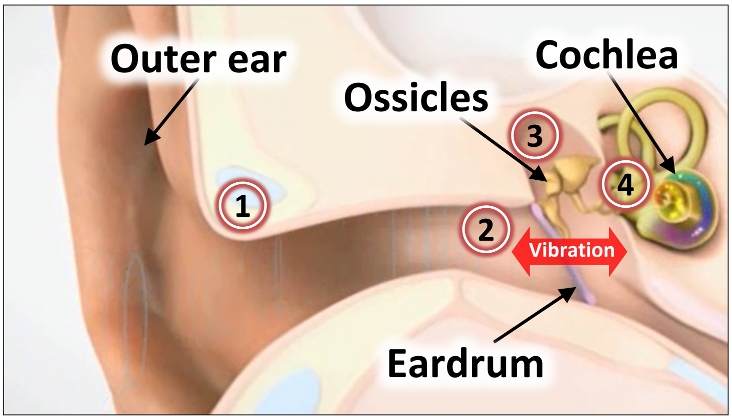

Figure 2.16: Peripheral auditory system [119].

vibrates similar to a stiff plate, and based on this result several researchers implemented a lumped parameter model of the eardrum. Later in 1972, Tonndorf and Khanna disproved the oversimplified lumped models using time-averaged holographic experiments [122]. Starting from 1980, by the development of computer-oriented solutions, FEM programs have been used for modeling of the eardrum [123–129]. FEM has proven itself a powerful tool for studying middle ear mechanics [127], [128], [130], [131], middle ear pathologies [132], and middle ear prostheses [133], [134]. Sun *et al.* developed an FE model of the middle ear and showed that it can be used to predict ossicular mechanism [127]. Figure 2.17 shows the FE model developed by the researchers.

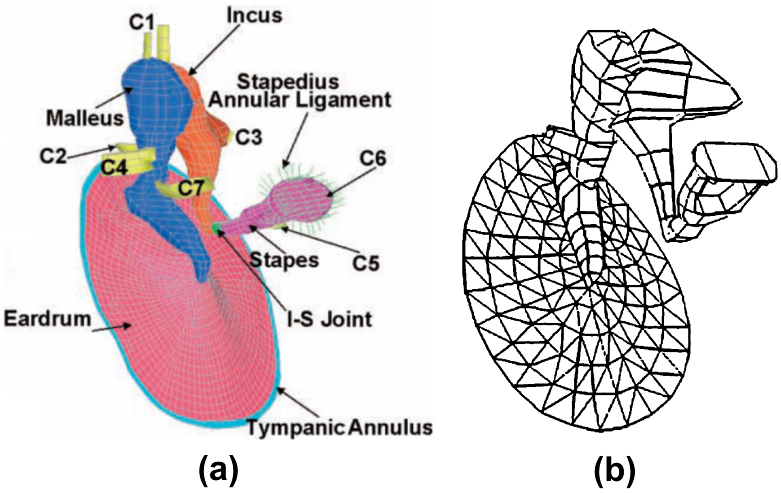

Figure 2.17: FE model of the middle ear for predicting mechanism of ossicular chain a) [127], *b)* [124].

This section aims to develop an FE model of eardrum. As a first step, a membrane model is developed using the FE program. The natural frequency results of the model developed is compared with that of the models using distributed parameter approach. It is shown that developed model can be considered as a base for further analysis required for the development of the eardrum model.

2.5.1 Modeling of a Membrane Using FEM

Dynamics of membranes are widely studied in literature [135–141]. Both distributed parameter models and FE models can be used to determine natural frequencies and mode shapes of membrane structures. Usually, 2-D elements are used in FE models for modeling thin structures. However, a 3-D model of an energy harvester is developed in Section 2.3 to be coupled with the eardrum. Thus, a proper 3-D FE membrane model is required instead of a 2-D model to overcome compatibility issues during coupling. Therefore, as a first step, a 3-D membrane model is developed [142]. A circular membrane with a diameter of 10 mm and thickness of 75 μm is analyzed considering the dimensions of a typical eardrum. Then, the model developed is compared with 2-D FE and distributed parameter membrane models.

For the 3-D membrane structure, the SOLSH190 element, which is suitable for analyzing thin structures is used [100]. Vibration analysis is made to obtain the natural frequencies of the prestressed membrane. Natural frequency of 1 kHz is chosen for verification purposes, which is the first natural frequency of eardrum. In this analysis, prior to modal analysis, membrane is stretched from its boundary by simply giving a predetermined displacement. It is observed that in order to obtain the first mode of the 3-D structure at 1 kHz, 20.6 μm stretching in radial direction is required. A similar analysis is applied to the same membrane modeled using 2-D SHELL181 element.

In order to verify the developed 3-D FE model, a continuous system model is used. The corresponding governing differential equation of the membrane and the well-known equation for the natural modes of circular membrane with clamped boundary are given in Equation 2.29 where n is the number of mode, λ is the eigenvalue of the n^{th} mode, $w(x,y,t)$ is the transverse displacement, ρ is the density, and h is the thickness of the membrane. However, these equations include tension term, T, instead of displacement, which is used as an input during FE analysis. Therefore, an alternative form of the well-known equation is derived by relating tension components to applied stretching displacement. To relate tension components to displacement, General Hooke's Law is used in cylindrical coordinates as given in Equation 2.30:

$$\omega_n = \frac{\lambda_n}{2\pi a}\sqrt{\frac{T}{\rho h}} \tag{2.29}$$

$$\begin{Bmatrix} \sigma_{rr} \\ \sigma_{\theta\theta} \\ \sigma_{zz} \end{Bmatrix} = \frac{2G}{1-2\upsilon}\begin{bmatrix} 1-\upsilon & \upsilon & \upsilon \\ \upsilon & 1-\upsilon & \upsilon \\ \upsilon & \upsilon & 1-\upsilon \end{bmatrix}\begin{Bmatrix} \varepsilon_{rr} \\ \varepsilon_{\theta\theta} \\ \varepsilon_{zz} \end{Bmatrix} \tag{2.30}$$

where σ_{rr}, $\sigma_{\theta\theta}$, σ_{zz}, ε_{rr}, $\varepsilon_{\theta\theta}$, and ε_{zz} are stress and strain in radial, angular, and axial directions respectively, υ is Poisson's ratio, and G is shear modulus. If we assume uniform stretching from the boundary of the circular membrane, twisting effects can be omitted. Thus, $\varepsilon_{\theta\theta}$ becomes equal to ε_{rr} at the boundary of the membrane which is simply the ratio of stretching displacement, x_0, to membrane radius a (x_0/a). Furthermore, since the circular membrane is stretched from its boundary in radial direction, σ_{zz} will be zero. Then, after relating shear modulus, G, with Young's Modulus, E, and Poisson's ratio, υ, using conversion formulas for isotropic materials, stress components σ_{rr} and $\sigma_{\theta\theta}$ can be obtained as in Equation 2.31.

$$\sigma_{rr} = \sigma_{\theta\theta} = \frac{x_0\, E}{a\,(1-\upsilon)} \tag{2.31}$$

Equation 2.31 can also be used to find the stress in the radial and angular direction at the boundary of the circular membrane when tension, T, can be written as multiplication of σ_{rr} with h. Thus, the natural frequency of the circular membrane can be obtained as a function of stretching displacement, x_0, as follows:

$$\omega_n = \frac{\lambda_n}{2\pi}\sqrt{\frac{x_0\, E}{a^3\rho(1-\upsilon)}} \tag{2.32}$$

Comparison of the evaluated natural frequencies using Equation 2.32 and by FE analysis using 2-D and 3-D models is given in Table 2.3. The results represent the natural frequencies when the membrane is stretched with a displacement of 20.6 µm. Membrane material properties are chosen considering a typical eardrum: ρ is 1200 kg/m^3, E is 32 MPa, and υ is 0.3 [143]. It is observed that 2-D FEM results are almost equal to distributed parameter model results (errors are less than 0.1%). Errors obtained using 3-D FEM are considerably higher than those obtained with 2-D model. However, due to requirement of integration of 3-D energy harvester model with 3-D membrane structure, 3-D FE model is used in this study as the percentage error in the fundamental frequency is only about 2%.

Table 2.3: Comparison of natural frequencies of circular membrane with clamped boundary obtained using distributed parameter model (DPM) with those of 2-D and 3-D FE models.

Mode	**DPM**	**2-D FEM**	**3-D FEM**	**% 3-D Error**
ω_{10}	973.86	974.52	1000.10	2.68
ω_{11}	1551.82	1552.38	1612.32	3.90
ω_{12}	2079.89	2079.05	2181.51	4.89
ω_{20}	2235.40	2234.74	2370.82	6.06

2.5.2 Modeling of the Eardrum Using FEM

Although there are discrepancies when compared with the results of DPM and 3-D FEM, 3-D FEM is chosen for modeling of the eardrum. One of the major reasons for this selection is the requirement of coupling of the eardrum model with the energy harvester model. Since mass and stiffness parameters of the energy harvester are comparable to those of the eardrum, using lumped elements or assuming concentrated loads through distributed parameter modeling do not fit the nature of the described problem. On the other hand, FEM is widely used in middle ear mechanics, and it is suitable for the analysis of coupled structures. These features make FEM as the most feasible method for modeling of eardrum.

Being one of the vital components of the human ear, the eardrum converts the acoustical sound pressures into vibrations. It is connected to the smallest bones in the body, and transfers the pressure waves to these bones as mechanical vibrations. The malleus, which is the first bone of the ossicular chain and is attached to the eardrum, starts to vibrate when sound pressures impinge on the eardrum. The eardrum is located at the inner side of the ear canal (auditory canal). Thus, the eardrum plays one of the most important roles in the peripheral auditory system.

The eardrum is positioned at about 55° to the ear canal, and its average thickness is approximately 75 µm (Figure 2.18) [144]. Its shape is elliptical with diameters of about 11 mm and 9 mm. The eardrum has an inward displacement of 1.5 mm at its center, which is associated with its attachment to the malleus [145–148]. The malleus continues through the boundary of the eardrum in a direction corresponding to the 11-o'clock position and 1-o'clock position (when observed from the ear canal) in the left and right ear, respectively [98].

Based on the recent results, unlike the membrane modeled in the previous section, the material properties of the eardrum cannot be assumed as isotropic. Several researchers have conducted research on the elasticity of eardrum [126], [127], [147], [151–158]. In their studies on eardrum modeling, Decraemer and Funnell mentioned mismatch in the displacement of models developed and experiments due to assuming eardrum as an isotropic material [151]. Due to the fibrous structure of the eardrum through radial and circumferential directions, two different elasticity values are used in the literature, namely radial modulus, E_R, and circumferential modulus, E_C. Researchers also stated the importance of considering the tissues called parsa tensa, parsa flaccida, and transition layers of the eardrum for the accuracy of simulations (Figure 2.19a). The parsa tensa is the region where the malleus is attached to the eardrum, and consists of three layers of mucosal layer, fibrous layer, and outer epidermal layer. The pars flaccida, on the other hand, is placed around the upper boundary of the eardrum, and has important acoustical effects. Consequently, orthotropic elasticity values of the various regions on the eardrum (Figure 2.19b) are used during simulations.

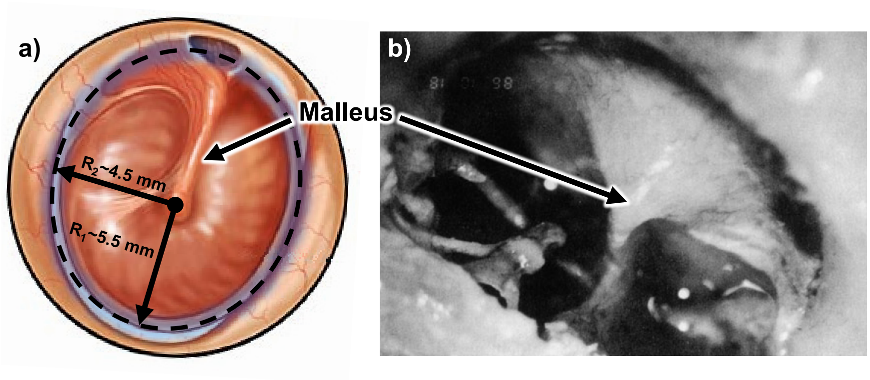

Figure 2.18: Eardrum geometry, a) view of the eardrum through the ear canal and the dimensions of the eardrum [149], *b) view of the eardrum from the middle ear demonstrating the conical shape of the eardrum* [150].

Regarding the Poisson's ratio of the eardrum, Funnell and Laszlo conducted several experiments; however, researchers did not observe any evidence for the effect of the parameter on dynamic behavior of the middle ear system [159]. Besides, up to now, all published results considered the Poisson's ratio for eardrum as close to 0.3 [123], [126], [127], [129], [160]. Therefore, Poisson's ratio is considered as 0.3 for eardrum.

During FE analysis, the vibration response of the structure are obtained by considering the Equation 2.33, where M, K, and C are mass, stiffness, and damping matrices, respectively, f is the nodal force vector, and u is the displacement vector. By constructing the geometry and using relevant material properties, mass and stiffness parameters can be evaluated. For the damping of the material, generally two different methods are considered.

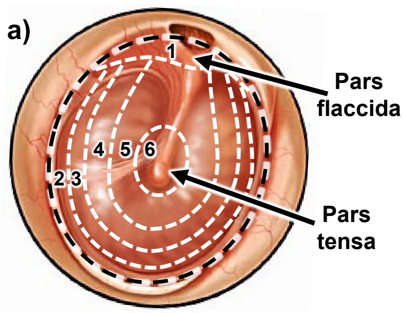

b)

	Young's Modulus [MPa]	
#	**E_C**	**E_R**
1	47	20
2	10	10
3	33.3	26.6
4	26.6	33.3
5	20	40
6	40	40

Figure 2.19: a) Pars flaccida, pars tensa and transition layers of the eardrum [149], *b) respective radial and circumferential modulus ($E_{R,}$ and E_C) values of the corresponding sections within eardrum* [126].

First method is to assume a constant damping ratio. This ratio is dependent on factors such as the geometry, the velocity, temperature, and pressure. Thus, it is best to evaluate the value experimentally [117]. The other method for the damping mechanism is the Rayleigh damping. This method evaluates the damping as a linear combination of mass and stiffness as given in Equation 2.34. In this equation, α and β are the damping parameters. Fortunately, several researchers conducted experiments and observed these values experimentally [161], [162]. The values used during simulations are given in Table 2.4.

$$M\ddot{u} + C\dot{u} + Ku = f \tag{2.33}$$

$$C = \alpha M + \beta K \tag{2.34}$$

Similarly, the malleus should also be modeled and attached to the eardrum. The malleus is one of the smallest bones in the human body, and transfers the vibrations of the eardrum to the ossicles. The material properties and damping parameters used during simulation for the malleus is also studied widely in literature, and are given in Table 2.4.

Table 2.4: Material properties of eardrum and malleus used in simulations.

Structure	Value	Reference
Eardrum		
Density	1.2×10^3 kg/m^3	[124], [126–128], [132]
Poisson's Ratio	0.3	[126–128], [132]
Young's Modulus	See Figure 2.19	
Damping Parameters	α=260 s^{-1}, β=3.7 x 10^{-5} s	[126], [128]
Malleus		
Density (average)	3.59×10^3 kg/m^3	[129], [147]
Poisson's Ratio	0.3	[127], [129], [147]
Young's Modulus	14.1 GPa	[129], [163], [164]
Damping Parameters	α=0 s^{-1}, β=0.75 x 10^{-4} s	[129], [132]

Figure 2.20a shows the FE model of the meshed eardrum structure, which is meshed using free mesh feature of the program. The meshed structure has a total of 6781 nodes and 807 elements. The eardrum structure is simply the integration of several parts, each having different elasticity as depicted in Figure 2.19 and material properties as given in Table 2.4. After developing the eardrum FE model and meshing, the malleus is tilted 16° around its fixed end to obtain the 1.5 mm of depth at the center of the eardrum while the boundary of the membrane is fixed [145–148]. Figure 2.20b shows the contour plot representation of the displacement of the eardrum.

Figure 2.20b shows the contour plot representation of the displacement of the eardrum. The FE model is developed using Ansys FE program. Due to its ability to link two analyses, such as transferring results of a static analysis to a modal analysis, obtained stress and strain values are recorded and transferred to the preceding analysis. After obtaining the respective strain parameters due to the malleus, other unknown mechanical property is studied. This unknown property is the forces on the boundary of the membrane structure. For determining unknown mechanical property, FE program is utilized to adjust the parameters. For this purpose Ansys FE programs “Design of experiments” tool is utilized. This tool adjusts the desired parameters, and desired values such as natural frequency of the structure or strain on the boundary can be observed.

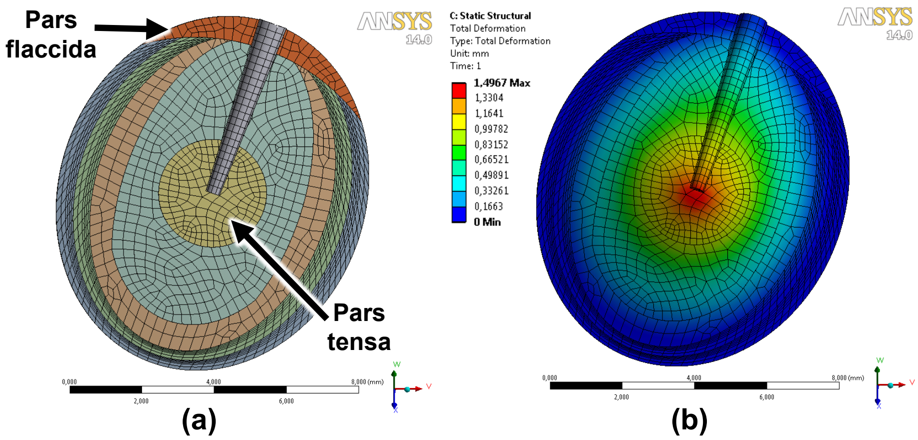

Figure 2.20: a) Meshed FE model of the eardrum showing six different sections of the eardrum including pars flaccida and pars tensa with 6781 nodes, b) static analysis results showing the depth of the central region.

After modeling and development of the corresponding material properties and geometry of the eardrum, the dynamics of the eardrum is considered. The most important issue that affects the dynamics of the FE model of the eardrum is the boundary conditions. These mechanical properties are poorly known and cannot be measured with traditional methods [159]. Up to now, several methods have been utilized to model the middle ear dynamics. These methods are simply based on adjusting the unknown mechanical property to verify the experimental results or known values. One of the utilized methods is to include the tissue covering the eardrum (tympanic annulus) to the model [127], [165]. Sun *et al*. used this method and included the covering tissue to the model, which is considered as an elastic material. Translational movements of the tissue are constrained, and in order to adjust the response of the FE model with the experimental values, the modulus of the tissue is adjusted to 0.6 MPa (with damping values of α=0 s^{-1}, β=0.0001 s). The other method utilized is to represent the boundary conditions of the eardrum by linear and torsional springs [124], [128], [129]. In this method, the nodes at the boundary of the structure are connected to spring elements as shown in Figure 2.21. Then, as in the previous method, the spring constants and damping parameters are adjusted to match with the experimental values. Wada *et al*. developed an eardrum model using this method, and obtained a linear spring stiffness of 4.0 x 10^3 N/m^2 and a torsional spring stiffness of 1.0 x 10^{-3} Nm/m. Another method for modeling eardrum is utilized by Ferris and Prendergast [126]. In their study, rotational movement at the eardrum boundary is constrained while stretching through radial direction.

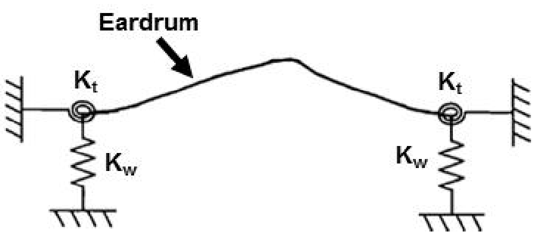

Figure 2.21: Proposed elastic boundary condition models for FE model of eardrum by Wada et al. [124].

In order to understand the dynamics of the eardrum various measurement methods have been utilized. Most popular techniques utilized are laser interferometry [129], [166–169], time-averaged holography [122], [170], [171], and video measuring system [172], [173]. Using these methods, researchers experimentally observed first and second natural frequencies of the eardrum at 996 Hz and 1924 Hz, respectively [124]. Thus, these frequencies are taken as a base for FE model of the eardrum, and corresponding boundary conditions are adjusted accordingly. In this thesis, two methods are studied to model the dynamics of the eardrum. Figure 2.22a shows the optimization routine developed using ANSYS FE program's Workbench module. This routine is used to adjust the parameters such that natural frequencies of the structure match with the published experimental results. These methods are adjusting the spring constants and radial displacements at the boundary of the eardrum. Figure 2.22b shows the conditional representation of the routine. This routine starts with static analysis in order to obtain stress and strain values on the eardrum structure due to the malleus and the boundary conditions (springs or stretching). Then, these values are considered as an initial condition of the subsequent modal analysis. This coupled operation is called as prestressed modal analysis. The modal analysis is used to determine the natural frequencies of the structure. The determined natural frequencies are compared with the referred natural frequencies (996 Hz and 1924 Hz). If the simulated values are not within a 3%, tolerance of the desired values procedure terminates, and parameters are adjusted accordingly. If simulated values satisfy the requirements, the procedure continues with harmonic analysis around the obtained natural frequencies. Harmonic analysis is conducted to obtain the displacement of the eardrum within a frequency range between 400 Hz and 3 kHz with an applied pressure of 0.63 Pa (equivalent of 90 dB SPL).

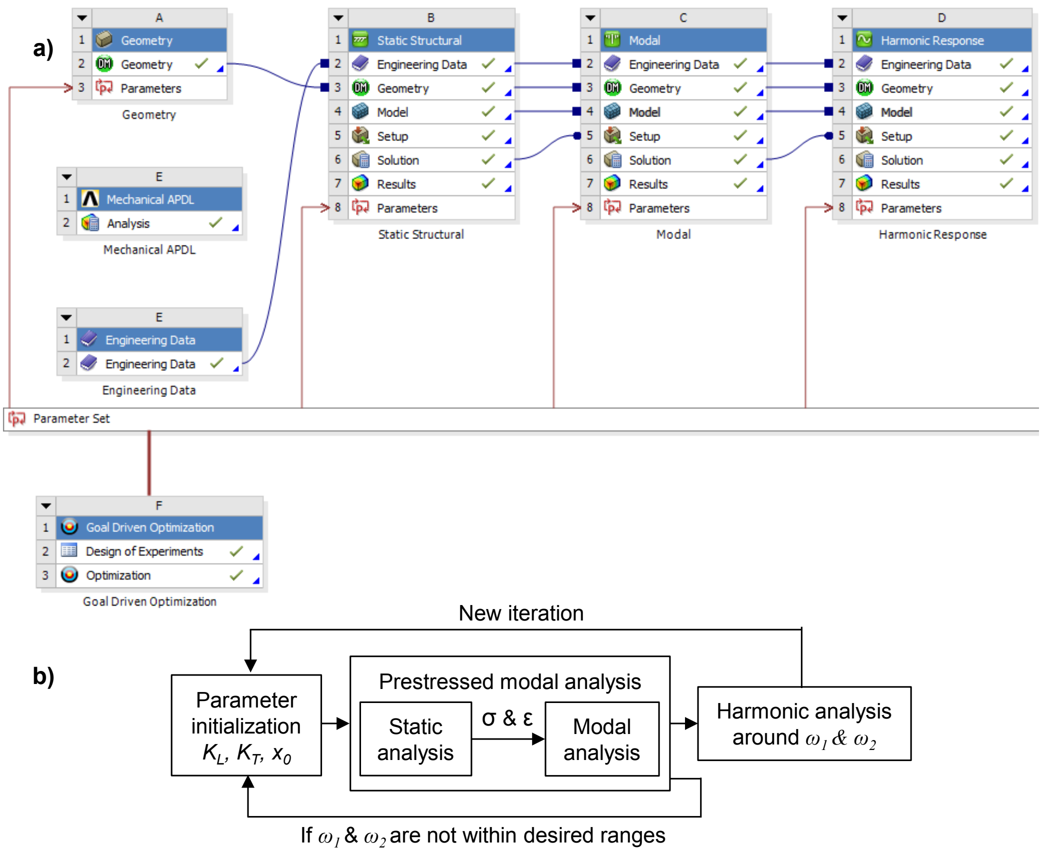

Figure 2.22: a) User interface of the ANSYS Workbench module for the developed optimization routine, b) conditional representation of the developed optimization routine.

During the adjustment of the parameters, importance is given to the first natural frequency, due to its importance for the application. Thus, error of less than 1% and 5% are aimed for the first and second natural frequencies, respectively.

In the first method, springs are coupled to the boundary of the eardrum, and then these spring constants are adjusted until the response of the eardrum model matches with the experimental values. In the second method, the eardrum is stretched from its boundary with a specific displacement in radial direction, which induces stress to the eardrum. This changes the dynamics of the eardrum, and causes change in natural frequency. For the analysis of the former system, an FE model of the eardrum is configured as shown in Figure 2.23a. In this model, linear and torsional springs are attached to the nodes located at the boundary of the eardrum.

ANSYS FE program has special elements for modeling systems with springs and dampers. In this analysis COMBIN14 element is used [100]. It is a 2-node element where nodes are placed at each end point of the spring and damper elements. One of the nodes of the element is attached to the boundary of the eardrum, while the other one is constrained in all directions. Besides, this element is capable of modeling both linear and torsional springs with respective constant damping ratios. Thus, both linear and torsional springs are connected to obtain the spring structure. Then, stiffness parameters are adjusted to match the natural frequencies and displacement patterns of the structure with the published data. Similarly, damping parameters are adjusted to minimize the difference between the experimental and simulated displacement values [129]. Table 2.5 gives the summary of the adjusted parameters. The parameters are adjusted to match the natural frequencies of the FE model with those of the published experimental results. By using the optimum values of the parameters obtained utilizing the first method, the FE model of the eardrum has its first and second natural frequencies at 1002.4 Hz and 1998.2 Hz, respectively.

Table 2.5: Adjusted spring and damping parameters of the eardrum model.

Linear Spring (K_L)			**Torsional Spring (K_T)**			**Damping Ratio (ζ)**		
Min	**Max**	**Step**	**Min**	**Max**	**Step**	**Min**	**Max**	**Step**
1×10^{3}	5×10^{3}	1×10^{2}	1×10^{-5}	5.2×10^{-4}	3×10^{-5}	9×10^{-2}	21×10^{-2}	3×10^{-2}
Optimum value			**Optimum value**			**Optimum value**		
4.2×10^{3}			4.3×10^{-4}			15×10^{-2}		

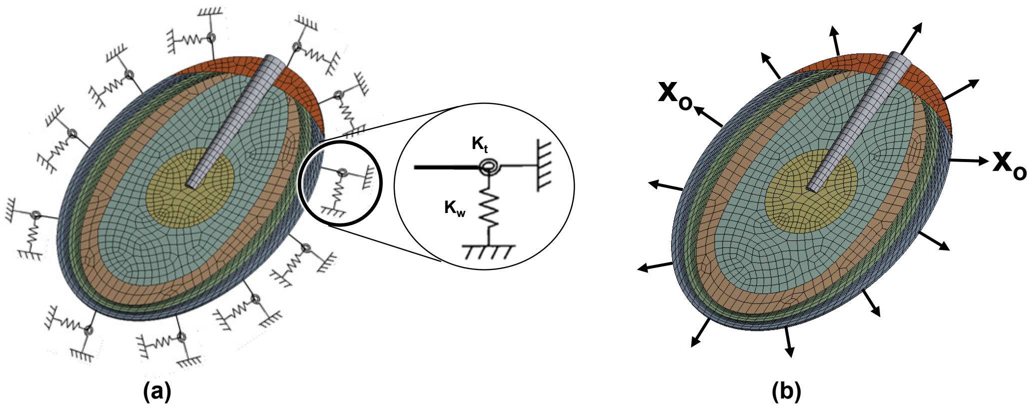

Figure 2.23: FE model of eardrum a) where linear and torsional springs attached to the nodes located at the boundary, b) where a predetermined displacement, x_0, is applied normal to the boundary.

The second method utilized is similar to the one followed in Section 2.5.1. As mentioned earlier, the tension applied to the boundary of a clamped circular membrane changes the dynamics of the structure considerably. Therefore, during FE model development of the eardrum, a stretching with known displacement condition is applied at the boundary to create tension as shown in Figure 2.23b. Unlike the previous method, this method has only one parameter to adjust, which is the displacement.

Vibration analysis is made to obtain the natural frequencies of the prestressed membrane. In this analysis, prior to modal analysis, membrane is stretched from its boundary by simply giving a predetermined displacement normal to the boundary. It is observed that the normal displacement at the boundary of the eardrum should be adjusted to 12.6 µm in order to obtain the first and second modes around 1 kHz and 2 kHz, respectively. As a result, this displacement gives natural frequencies at 1003.5 Hz and 1905.4 Hz.

The method utilized in this part can be developed by using model updating techniques. This method is used to decrease the degree of miscorrelation between experimental data and FE model results [118]. Several points of the structure are investigated during experiments, and their vibration characteristics are compared with that of the FE model results. By utilizing model updating techniques, the discrepancy between the FE model and experiments can be eliminated. However, for modeling of eardrum, experiments are conducted only considering the middle section of the eardrum. Thus, there is not enough data to apply model updating techniques during this study.

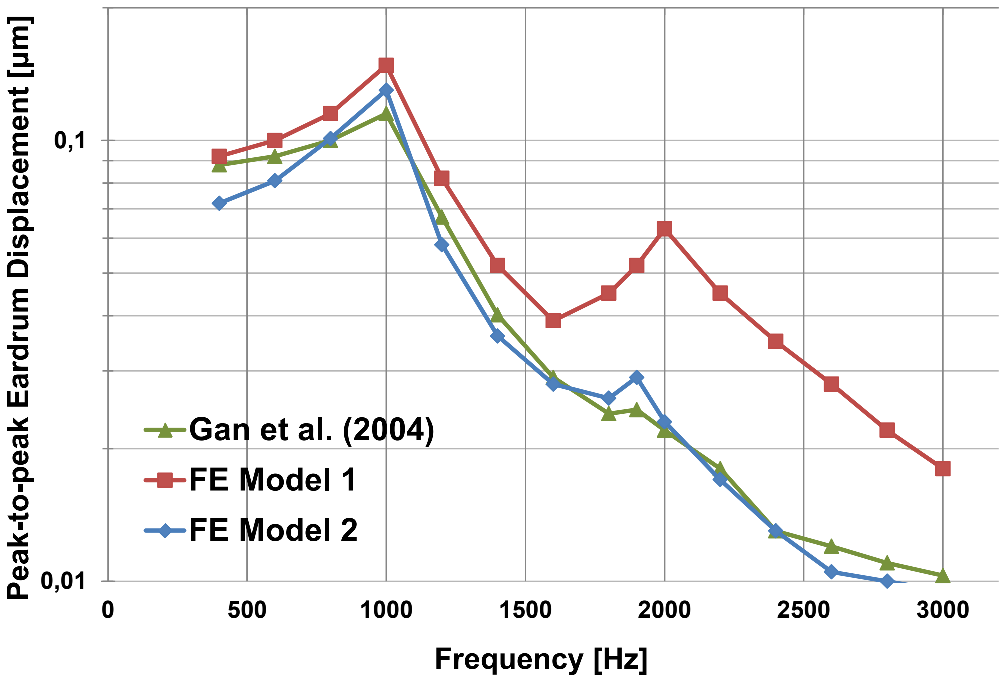

Figure 2.24: Comparison of the developed eardrum FE models with the measured eardrum frequency response curve at 90 dB SPL [129]. *(FE Model 1: springs are attached to the boundary, FE Model 2: stretching displacement is applied to the boundary).*

After optimization of the stiffness and stretching displacement parameters, harmonic analysis results of the structures are compared with the published measured displacement results for the eardrum. In the mostly cited work of Gan *et al.*, eardrum frequency response curves are obtained from 10 samples at 90 dB SPL [129]. Researchers used double laser interferometer technique for the measurement of the eardrum displacements. Comparison of the eardrum frequency response curves between the developed FE models and the measured data is given in Figure 2.24. The former FE model matches the measured data up to 1.6 kHz. However, then, the difference between the displacement of the model with the measured data increases. On the other hand, the latter model where the boundary of the eardrum is stretched with a predetermined frequency results in a close match with the experimental result. Furthermore, since the resonance frequency match better than the first model, it is concluded that the dynamical behavior of the eardrum can be represented more accurately with this model. Thus, second model is considered as a base for the optimization of the dimensions of the energy harvester mounted on the eardrum.

2.6 Optimization of the Harvester Coupled to the Eardrum

After the development of the energy harvester and eardrum FE models, the energy harvester is coupled to the eardrum as in the desired application. In the real application, there are two possible procedures for mounting the harvester on the eardrum. First procedure is removing the malleus (which is a typical middle ear surgical operation) and mounting the harvester on to a uniform surface. Second option is mounting the harvester onto the malleus of the eardrum. During surgical operations, for mounting or gluing applications special types of surgical sealants or adhesives are used. Although mounting the harvester on the malleus would be relatively easier operation for surgeons, this operation requires much more adhesive than the former procedure, where malleus is removed and harvester is mounted on the uniform eardrum surface. Increased adhesive thickness would require an elastic contact model, and there is no sufficient data on this issue. Therefore, during optimization study, it is assumed that the malleus is removed from the eardrum, and the contact between the harvester and the eardrum is assumed as rigid.

Figure 2.25 shows the FE model of the coupled structure, where the harvester is mounted on the eardrum. The eardrum is stretched with the displacement value obtained in the previous section, which is 12.6 µm. Besides, the orientation of the eardrum is arranged such that the angle between the horizontal axis (y-axis) with the eardrum surface is 55° as in the human ear, and gravitational acceleration is applied along the vertical (-z-axis) direction. Considering the symmetry along the malleus, the harvester is mounted along the malleus bone. The dimensions of the case of the harvester are considered as constant with a footprint of 5 mm x 5 mm, as discussed in Section 2.3.

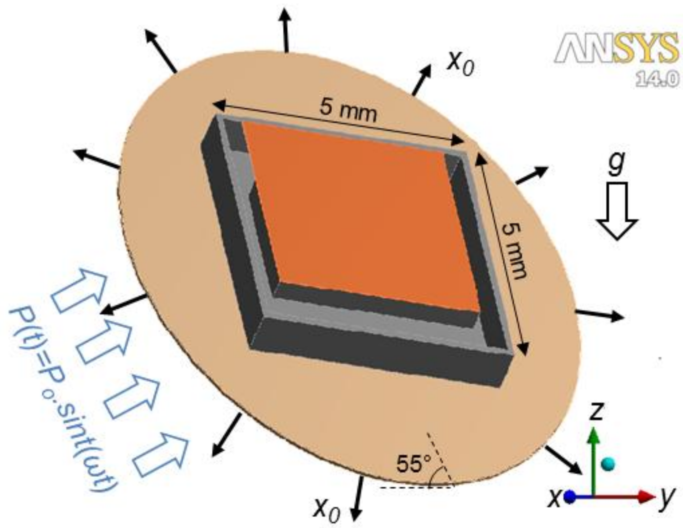

Figure 2.25: FE model of the energy harvester mounted on the eardrum showing the boundary conditions and orientation of the eardrum. Eardrum is oriented at an angle of 55° to the horizontal axis (y-axis), and gravitational acceleration is applied along vertical axis (z-axis). Pressure, P(t), is applied normal to the membrane surface.

After coupling the harvester and the eardrum structures, design parameters of the harvester are optimized to give the maximum voltage output while resonating at various and predetermined frequencies within the band of daily sounds. One of the chosen operation frequency is 1 kHz. The reason for choosing 1 kHz is due to its abundance as discussed in Section 2.1. Design variables to be optimized, constants, and objective function of the optimization problem of the energy harvester are summarized in Table 2.6.

Table 2.6: Design variables, constants, and objective function for the optimization of energy harvester. ([a] The PZT thickness is taken as a variable for the case where excitation frequency is 1 kHz. Then, after optimum results are obtained for 1 kHz, for the optimization studies considering other excitation frequencies, it is taken as a constant and equal to the optimum value considering 1 kHz.)

	Parameter	Unit	Minimum	Maximum
Design variables	Beam length	mm	3.5	4.25
	PZT length	mm	1	4.25
	PZT thickness [a]	µm	10	50
	Tipmass length	mm	0.1	3.5
Constants	Beam width	mm	4 mm (due to fabrication issues)	
	Beam thickness	µm	10 µm (due to SOI wafer specifications)	
	Tipmass thickness	µm	350 µm (due to SOI wafer specifications)	
Objective	Voltage	V	Maximize voltage	

Schematic representation of the cantilever structure is similar to the one given in Figure 2.8; therefore, it is not repeated in this section. Designs are based on the assumption of utilizing (100)-type silicon-on-insulator (SOI) wafer type for the fabrication. The thickness of the layers of the SOI wafer are assumed as 10 µm, 2 µm, and 350 µm of device layer, buried-oxide layer, and handle layer, respectively. Therefore, parameters such as beam thickness, and tipmass thickness are considered as constant due to the fabrication issues. Furthermore, beam width is constrained due to bonding operation. Flip-chip bonding tool is used for bonding process, and it is experienced that in order to use the tool properly, at least one of the dimensions of the bonded material should be larger than 3 mm. Therefore, beam widths of all devices are considered as constant due to the mentioned issue. On the other hand, it should be noted that the wafer flat is assumed to be parallel to the width of the cantilever structure; thus, orthotropic material properties are used accordingly as described in Section 2.3. Similar to the one described in previous section, an optimization routine is developed using FEM program, which is summarized in Figure 2.26. The objective function of the optimization is defined as maximizing the voltage output of the piezoelectric material when the coupled structure is excited with 100 dB SPL (equal to 2 Pa) at 1 kHz frequency as well as several other predetermined frequencies within the hearing band (750 Hz and 1.5 kHz).

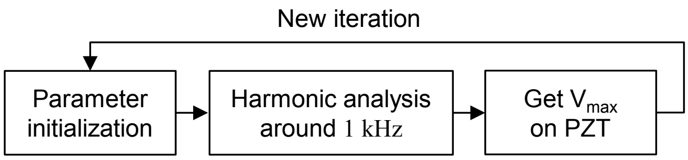

Figure 2.26: Schematic representation of the optimization routine.

The FE program offers several optimization methods and tools, such as sub-problem approximation, first-order optimization, sweep, and factorial tool. During the optimization studies of the harvester, first-order method is utilized. Among other methods, first-order optimization is widely used for structural optimization problems, and it is more computationally demanding and accurate [174], [175]. This method makes use of derivative information and penalty functions. Using these, search direction and gradient computations are updated in each iteration. During optimizations, developed routine is executed 2000 times consecutively to find the global maximum value for voltage within desired dimensions.

It is obvious that the time required for the optimization process is heavily dependent on the meshing of the structure. Initially, free mesh pattern was used, which requires shorter time periods. However, it is observed that as the dimensions vary during the optimization process, patterns of the free mesh also changes. In addition, since the micro-scale harvester has a high length-to-thickness ratio, most free mesh patterns formed only two elements through the thickness of the beam. In fact, stress on the piezoelectric material is critical for obtaining the voltage value. Therefore, a predetermined meshing pattern is also embedded into optimization code to control the meshing of the structure. On the other hand, there is a trade-off between accuracy and simulation time. Stress values of the piezoelectric material are observed while changing the number of elements through the thickness. It is observed that stress value converges (within 3%) after having five elements through the thickness of the piezoelectric and cantilever beam structures. Therefore, it is decided to use five elements through the thickness of the piezoelectric material and silicon cantilever beam as shown in Figure 2.27. The resulting optimum parameters of the energy harvester considering excitation frequencies within the hearing band are listed in Table 2.7. It should also be noted that, PZT thickness parameter is taken as a variable in the beginning. During grinding process, all of the bonded PZT pieces are thinned down to equal thickness. Therefore, after optimum parameters are obtained for 1 kHz frequency, the optimum PZT thickness value is taken as a constant.

The optimized parameters are given in Table 2.7 along with the maximum voltage values (for 100 dB SPL excitation) and natural frequencies of the harvester and the coupled structure. From the table, it can be seen that maximum voltage of 223.4 mV, 188.2 mV, and 122.6 mV is generated when the coupled structure is excited with 100 dB SPL at frequencies of 1.5 kHz, 1 kHz, and 750 Hz, respectively. It should be noted that these values can be improved if the generator operates under vacuum environment, which is also required for the real application.

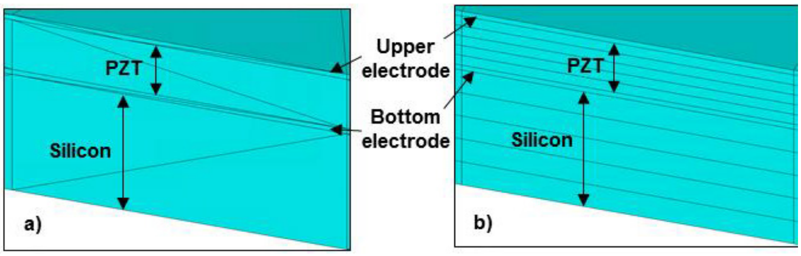

Figure 2.27: View through the thickness of the harvester with a) free meshed structure, a) sweep meshed structure.

Table 2.7: Optimized parameters for frequencies of 1.5 kHz, 1 kHz, and 750 Hz for (100)-type SOI wafer with 10µm/2µm/350µm device, buried-oxide, and handle layer thickness, where excitation of 100 dB SPL is applied.

Parameter	Unit	1500 Hz	1000 Hz	750 Hz
Beam length	mm	4.25	4.25	4.25
PZT length	mm	4.15	2	1
PZT thickness	µm	25	25	25
Tipmass length	mm	2.7	2.15	1.48
ω_1 harvester	Hz	571.1	520.2	200.4
ω_1 coupled		283.5	300.4	315.0
ω_2 coupled		498.4	512.2	510.1
ω_3 coupled		530.0	560.8	598.7
ω_4 coupled		1478.6	1020.1	754.3
Maximum voltage	mV	223.4	188.2	122.6

Figure 2.28 shows the first four mode shapes of the coupled structure. In order to generate the maximum voltage from the piezoelectric material, stress induced through the piezoelectric material should be maximized. It can be seen from first, second, and third mode shapes that the resulting relative displacement between the tips of the cantilever beams are relatively smaller than that of the fourth mode shape. Therefore, much more stress is induced through the piezoelectric material for the fourth mode shape. Besides, if the coupled structure is considered as a two-degree-of-system, the first and fourth mode shapes corresponds to (1,1) and (1,-1) modes of the lumped system. In this sense, the latter mode of the lumped system would result in much more relative displacement between the tip

of the harvester and the membrane structure. Clearly, this is the reason why optimization results converged to the case where the frequency of the fourth mode shape matches with the excitation frequency.

In addition to the optimized values given above, the developed method of optimization is used for the optimization of the structures where different fabrication constraints are applied. For instance, when a regular Si wafer is used instead of an SOI wafer, the design parameters and obtained mode shapes change considerably (due to increased wafer, and hence tip mass thickness). During fabrication of the harvester, initially prime wafers were used instead of SOI wafers. Therefore, design parameters are also obtained for the prime wafers using the same optimization routine and method described above. In this sense, constants of the design, which are beam thickness, beam width, and tipmass thickness, are taken as 15 μm, 4 mm, and 550 μm, respectively. Furthermore, due to the constraints in the grinding step of, PZT thickness is also considered as constant at 50 μm.

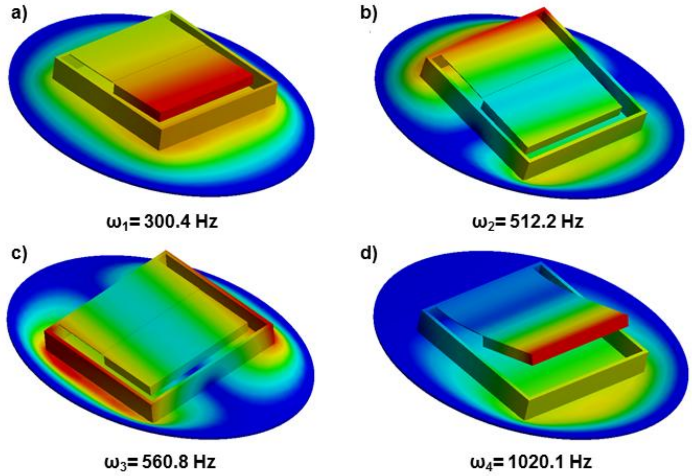

Figure 2.28: First four mode shapes of the coupled structure, which is optimized by using an excitation frequency of 1 kHz.

2.7 Summary of the Chapter

In this chapter, first, proposed application to alleviate or eliminate the recharge/replacement of battery problem of conventional cochlear implants is explained. Then, modeling, design, and optimization studies for the proposed application are explained. Various methods for modeling piezoelectric energy harvesters are discussed, and reasons for choosing FE modeling are elaborated. FE model of the piezoelectric energy harvester is explored. Next, studies on modeling of the eardrum are given. After the development of the eardrum and the harvester FE models, these structures are coupled. Finally, dimensions of the harvester are optimized for various sound frequencies.

CHAPTER 3

FABRICATION AND EXPERIMENTATION OF MEMS PIEZOELECTRIC ENERGY HARVESTER

At the beginning of this chapter, various methods for fabricating micro-scale piezoelectric transducers are discussed. The chapter continues to elaborate on the challenges and issues in the bonding of the preferred piezoelectric material. Next, fabrication of the designed MEMS harvester is explained in detail. Eventually, the chapter ends with the experimental results.

Figure 3.1 shows the cross-sectional view of the MEMS structure. The structure is a fixed-free type of cantilever beam with a tipmass at the free-end. Tipmass is used to lower the natural frequency of the harvester and to increase the induced strain on piezoelectric material. The piezoelectric material is bonded around the anchor, and depending on the design, it is bonded partially or fully on the beam.

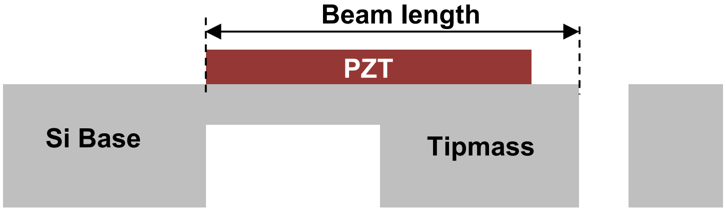

Figure 3.1: Cross-section of MEMS harvester structure.

Several materials are employed in literature for the fabrication of piezoelectric transducers. Among other available materials, bulk piezoceramics are advantageous for their high power output potential and are utilized in this study. Proposed fabrication flow in this thesis consists of two main parts: integration of bulk piezoceramics into MEMS and forming cantilever structure with tip mass. Although the latter is easily achievable via standard MEMS processes (such as DRIE), the former process yields constraints. These constraints are temperature and thickness, and arise from the features of the bulk piezoceramics. In order to overcome these constraints, the fabrication flow consists of processes such as low temperature bonding (via conductive layers), thinning of the bonded piezoceramics, and lithography over thick structures. For this purpose, various methods are studied. Finally, empirically validated processes are integrated to the fabrication process.

3.1 Piezoelectric MEMS Fabrication Methods

Various methods are utilized to fabricate piezoelectric microsystems. These methods differ based on the utilized piezoelectric material. Major differences of the methods are also summarized in Table 3.1.

Table 3.1: Comparison of various piezoelectric materials used for the fabrication of energy harvesters [37], [176].

	Coupling coefficient (k_{31}^2)	Strain coefficient (d_{31}) [pm/V]	Process temperature [°C]	Material thickness [μm]
Bulk Piezoceramics	0.09 – 0.65	100 – 1200	250 – 350	> 130 μm
Sol-gel Method	0.04 – 0.09	16 – 100	400 – 800	< 2 – 4 μm
Epitaxial PZT	0.09 – 0.15	49 – 140	600 – 650	< 3 μm
Sputtered PZT	0.07 – 0.15	28 – 150	450 – 650	< 2 – 4 μm
Screen-printed PZT	0.05 – 0.10	60 – 130	650 – 900	10 – 100

Among these methods, sol-gel is one the most common method used for fabrication of piezoelectric MEMS devices. The reason for its popularity is its ease of fabrication. It is coated onto a wafer with a spin coating process similar to resist coating. However, after coating process, a high-temperature annealing process is required, which is around 700 °C. This temperature profile is required to form a cubic structured piezoelectric material; thus, a small charge difference occurs between each unit cell. On the other hand, the applied high-temperature profile also results in more thermal stress in the final structure. Figure 3.2 shows the piezoelectric harvester structures fabricated with sol-gel method, where beams are curled due to the high temperature profile. Even, the mismatch of the coefficient of thermal expansion of the piezoelectric film and base structure (usually a conductive layer on silicon) might result in micro-cracks or delamination [37].

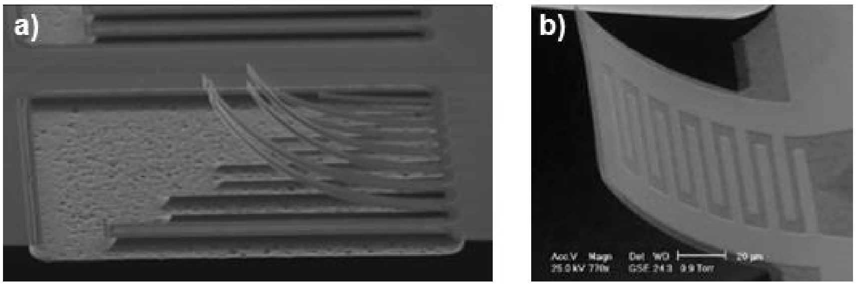

Figure 3.2: SEM images of curled beams fabricated via sol-gel PZT coating method, a) array of cantilevers [177]*, b) piezoelectric beam with interdigitated electrodes* [43].

Other widely used method for the fabrication of piezoelectric MEMS is epitaxial growth. For the integration of piezoelectric materials into MEMS processes, in McKee *et al.*'s widely referred work, a procedure for the growth of piezoelectric layer, $Pb(Zr_{0.2}Ti0.8)O_3$, on silicon substrate is summarized [178]. Several researchers used this method for the fabrication of piezoelectric energy harvesters, and growth up to 3 μm-thick PZT layer [179], [180]. However, high-temperature profile (around 650 °C) is also the case for this process; thus, it should be taken into consideration during fabrication.

Another method used for piezoelectric MEMS devices is sputtering. This method is also similar to the conventional metal sputtering processes, but requires a separate chamber to prevent contamination issues. Similar to sol-gel and epitaxial growth methods, only thin layers (<3 μm) can be obtained with this method. Furthermore, high-temperature (600-650 °C) is again a problem that should be considered while using this method [37].

Above mentioned thin-film methods are relatively easier processes with respect to other methods. However, the major disadvantage is that these methods are able to growth piezoelectric layers of ~4 μm at most, which results in lower voltage outputs. Screen-printing technique is studied by several researcher to overcome this issue [181–185]. Figure 3.3 represents the screen-printing technique. In this method, PZT slurry is prepared similar to the sol-gel method. However, instead of spin-coating process, a stencil is utilized to form patterns on the substrate surface. Thus, the thickness of the structures can be defined via the stencil height. This method clearly eliminates the thickness constraint of the previously mentioned thin-film methods. However, in order to polarize the screen-printed PZT, high-temperature profile is also required which may lead to stress-related problems.

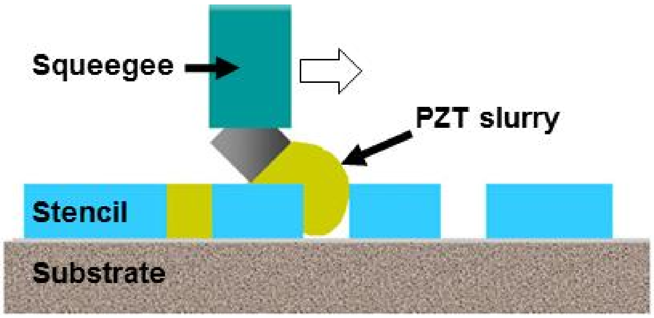

Figure 3.3: Screen printing technique [186].

For the mentioned methods, the requirement of high-temperature profile not only results in high-stressed final films, but also causes problems such as volatility of PbO [187] and diffusion of Pb through the electrode layer [188]. Besides, unrepeatable polarization processes results in disorientation of the crystal structures, which causes degradation of piezoelectric properties or low strain coefficient. Among these methods, bulk piezoceramics have recently received great attention due to their low temperature processes and relatively higher coupling coefficient and charge capacity [97], [189], [190]. These parameters are important for the power output of the piezoelectric materials. Besides, these bulk piezoceramics materials are commercially available with wide range of thickness; thus, thickness problem can be eliminated as well as unrepeatable polarization problem. The mentioned advantages of the bulk piezoceramics make it a promising candidate for energy harvesting applications. Recently, Aktakka *et al*. developed a process for the integration of bulk piezoceramics for fabrication of energy harvesters and various transducers [97].

As seen from the Table 3.1, bulk piezoceramics provide relatively higher coupling coefficient and charge capacity, which are also desirable in energy harvesting applications. Therefore, bulk piezoceramics are utilized in this study for the fabrication of micro-scale piezoelectric energy harvester due to its superior properties. However, these advantages came with price, and this method has some drawbacks. These drawbacks are: handling of the bulk piezoceramics material, requirement of low temperature bonding with conductive layers, and thinning of the ceramics to desirable ranges. In the following sections, these issues will be addressed and solutions developed through empirical research will be proposed.

3.2 Bonding of Bulk Piezoceramics to Silicon

The challenge in bonding of the bulk piezoceramics is due to its Curie temperature (350°C for PZT-5A). In this sense, a low-temperature bonding method is essential to prevent degrading of piezoelectric properties. Therefore, prior to fabrication process, a low temperature conductive bonding method is studied. In the scope of this study, three different bonding methods are evaluated. Initially, a wafer-level integration method is proposed utilizing parylene material. This method utilizes parylene as an interlayer material and arbitrary shaped structures can be attached to handling wafer at room temperature and without any applied pressure [191], [192]. However, the subsequent process would require a vacuum bonder to be utilized. Since, indium metal is used for the subsequent process, the wafer-level attachment method is not preferred due to contamination issues of indium metal. Other two methods for bonding of piezoceramics are gold (Au) thermocompression and gold-indium (AuIn) intermetallic compound formation. These methods are preferred, since they do not require a dedicated vacuum bonder and can be applied via other devices.

For the bonding process, SET FC150 flip-chip bonder device is used (Figure 3.4). This device is used for chip-to-chip and chip-to-wafer bonding processes via thermocompression, ultrasonic, and adhesive bonding methods [193]. Utilizing this device, bonding operations requiring temperature and force levels of up to 450 °C and 500 N can be accomplished with variety of chip and substrate sizes. In fact, the bonding process of the PZT-5A should not exceed the Curie temperature of the material (350 °C). Therefore, both temperature and force levels of the device are adequate for the desired bonding operation.

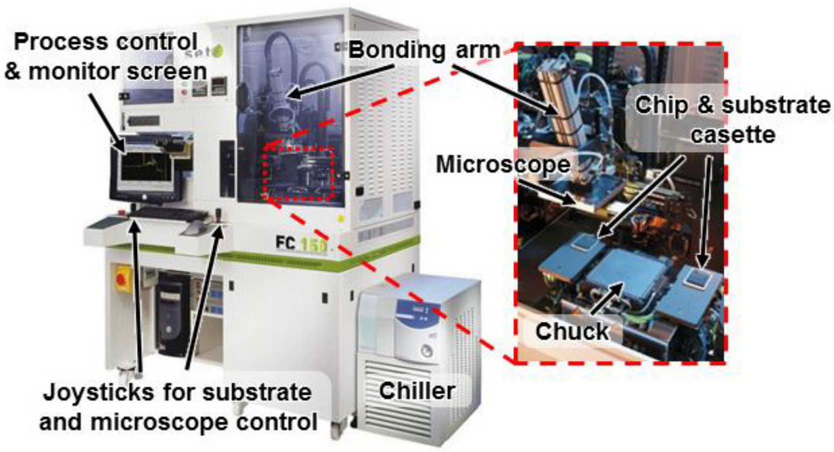

Figure 3.4: SET FC150 flip chip bonder system [193].

3.2.1 Gold Thermocompression Bonding

Up to now, various bonding methods have been investigated by researchers for bonding of bulk piezoceramics to silicon or glass wafers. Some of these methods utilize surface activation [194], epoxy resin [195], AuSn [196], or Cytop [197]. However, these methods have some drawbacks such as nonconductive and nonpatternable bonding layer, voids in the bonding layer, and high temperatures and stress during bonding operation [37]. Gold thermocompression method is one of the most widely used methods for bonding of silicon wafers [198–202]. It is mostly used for packaging applications, where hermetic bonding is desired. Besides, the metal interlayer makes it possible create interconnects, and gold is the most popular thermocompression metal due to its oxidation resistant property and low modulus [198]. This method is mainly a function of pressure and temperature. During bonding, as temperature increases, the metal softens. Meanwhile, application of pressure increases the bondability of the surface, and bonding occurs at lower temperatures than the melting point of the metal interlayer. Bonding recipes including various temperature and pressure values ranging from 300 °C to 450 °C and 0.06 MPa to 7 MPa have been reported [203–206].

To observe relation between temperature and pressure on bonding quality, various temperature and pressure values were investigated. Temperature values of 450 °C, 350 °C, 300 °C, 275 °C, and 250 °C were utilized while pressure values of 6 MPa, 3 MPa, and 1.5 MPa were applied. Additionally, to observe the effect of O_2 plasma cleaning, some of the samples were bonded after treating their surface with O_2 plasma. For the bonding trials, a silicon wafer is coated with Cr/Au (20nm/150nm), and diced. Chip and substrate sizes of 4 x 4 mm^2 and 6 x 6 mm^2 are used. Five to seven samples were prepared for each profile.

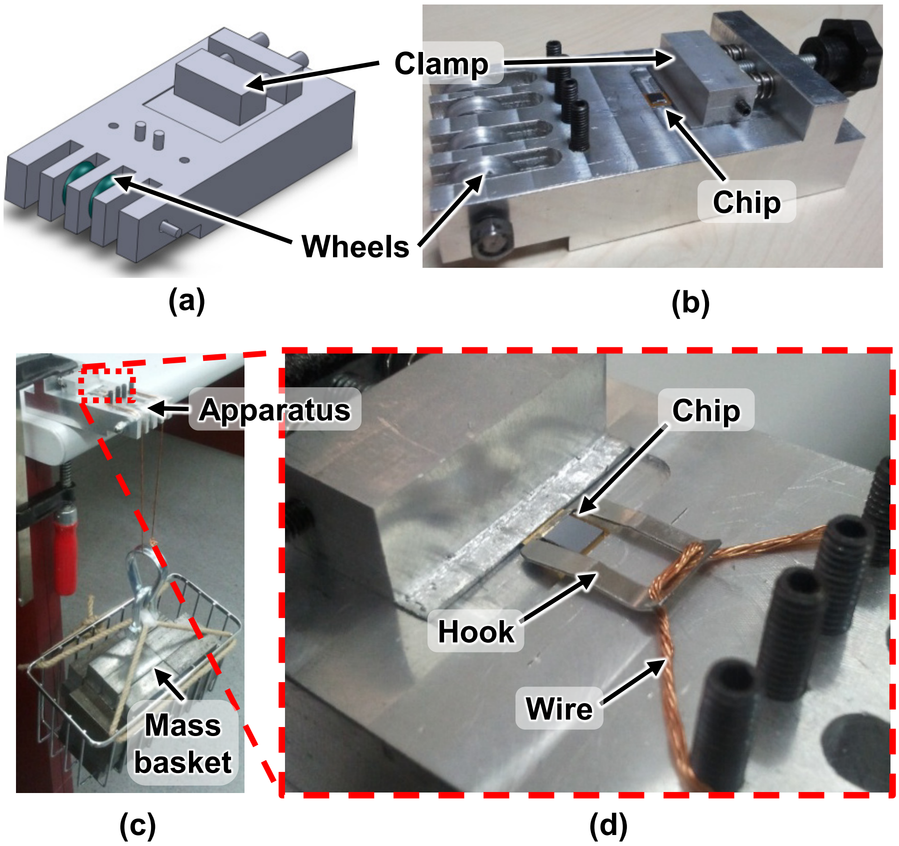

Figure 3.5: a) CAD model of the designed shear test apparatus, b) manufactured apparatus, c-d) experimental setup for the shear test measurement of gold thermocompression-bonded samples.

In order to quantify bonding quality, a shear test apparatus is designed and manufactured as seen in Figure 3.5a-b. The apparatus is designed such that the lower part of the bonded structure, which has footprint of 6 x 6 mm^2, is fixed via a clamp mechanism. Figure 3.5c-d gives the experimental setup. The shear test apparatus is fixed to a table with a clamp. Shear force is applied to the smaller chip (placed on the upper side) via a specially designed hook, which is connected to copper wire. At the other end of the wire, a basket is tied where masses of 175±1 g each are placed to control the applied shear force, which results in shear strength step of 0.0759 MPa for the given dimensions. Figure 3.6 shows one of the sets of the bonded samples before and after the test.

Figure 3.7 gives the experimental results. Samples bonded with temperatures of 250 °C and 275 °C with bonding pressures of 3 MPa and 1.5 MPa, did not withstand even the smallest applied pressure step. When bonding pressure is held constant, the effect of temperature is considerable within 250 °C to 300 °C and 350 °C to 450 °C. On the other hand, there is only a small increase in the shear strength when increasing the bonding temperature from 300 °C to 350 °C, which is one of the critical temperature ranges for the purpose of the required bonding method. Consequently, it is observed that for the bonding temperature below the Curie temperature of PZT-5A (>350 °C), the gold thermocompression method can give strengths of up to 3 MPa. However, this strength is not enough for the subsequent grinding process. In this sense, another bonding method is studied for the bonding of bulk piezoceramics to silicon.

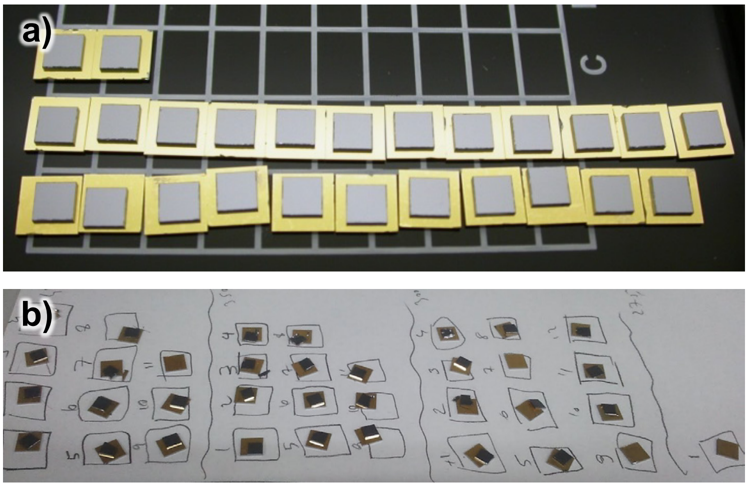

Figure 3.6: Gold thermocompression bonding a) samples before shear test, b) cracked samples after shear test.

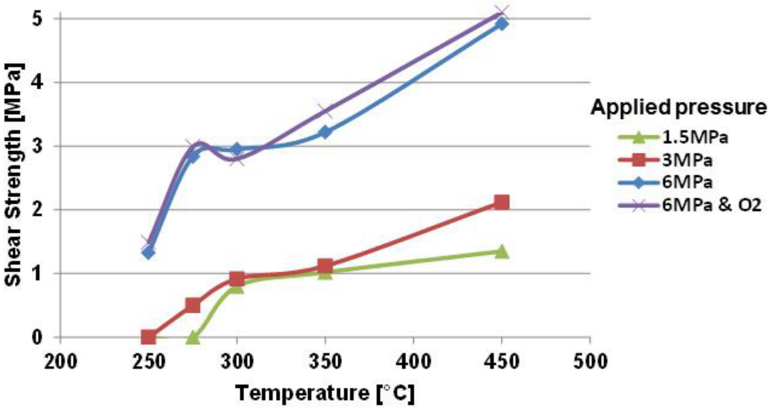

Figure 3.7: Experimental results of the bonded samples with gold thermocompression method.

3.2.2 Bonding Using Gold-Indium Intermetallic Compound

The other investigated bonding method utilizes gold-indium (AuIn) intermetallic compound. Welch *et al*. from the University of Michigan developed a low-temperature and patternable bonding method utilizing gold-indium and this method is called transient liquid phase (TLP) solder bonding [207]. In this method, a low-melting point metal (indium) is used, which melts around 156 °C. The bonding layer is formed by sandwiching indium between two parent metals such as gold. As the temperature and pressure increases, indium diffuses through the parent metal and reacts. Depending on the weight percentage of the metals, re-melting point of the final composition increases considerably. Aktakka *et al*. from the same group utilized this method for the fabrication of a micro-scale vibration energy harvester [176]. A wafer-level bonding method is also proposed for integration of piezoceramics into MEMS.

For the development of the AuIn bonding, firstly 7 cm x 7 cm piezoelectric sheet is coated with Cr/Au/In/Au (50nm/400nm/3μm/300nm). Therefore, indium is sandwiched between two gold layers, and oxidation of the indium is prevented. Then, coated piezoelectric sheet is diced. Diced samples are bonded to gold coated substrates via flip-chip bonder. As in the gold thermocompression method, several temperature and pressure profiles have been applied. First, temperature of 160 °C with

1.5 MPa have been applied, but this result in unsatisfactory results. It was observed that the molten indium metal during bonding could not reach the surface of the substrate as expected, and voids occur. Then, temperature is increased to 210 °C and various pressure values were investigated. Eventually, at 2.5 MPa satisfactory bonding occurred. In order to quantify the measurement, previously manufactured shear test setup was used. However, due to relatively low thickness of the PZT (160 µm) samples with respect to silicon (525 µm), the hook mechanism did not work. Furthermore, manufactured thin hook mechanisms did not survive under applied loads. Therefore, the bonded samples were investigated by performing the subsequent grinding process. Recent study on bonding of piezoelectric materials to Si using AuIn compound showed that an average shear strength of 4.44 MPa can be achieved [37]. In this study, bonded PZT pieces are thinned down to tens of microns using AuIn bonding method.

Disco Corp.'s DAG810 single-axis grinder machine is used for thinning process (Figure 3.8a). For thinning of ceramic materials, manufacturer's recommended recipe was utilized. Important parameters are, spindle speed, chuck speed, and spindle feed rate, which are 4000 rpm, 100 rpm, and 0.5µm/s respectively. Figure 3.8b shows one of the thinned samples and its close-up view around the edge. With this recipe, 160 µm-thick PZT was thinned down to 20 µm, which was bonded with the developed method. In this regard, developed bonding and grinding methods are utilized during the fabrication of energy harvester.

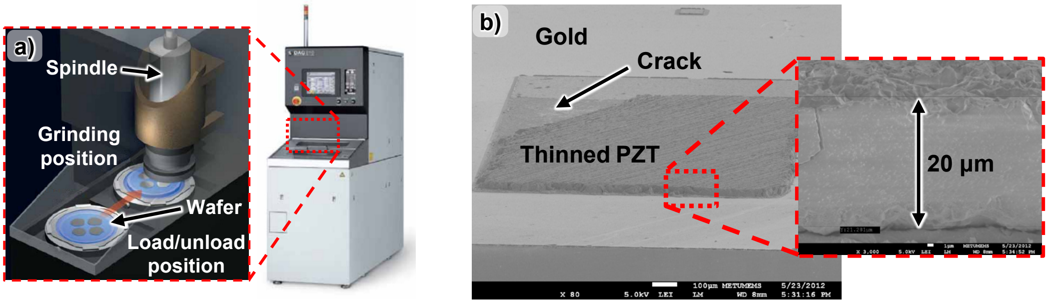

Figure 3.8: a) Disco DAG810 grinder machine [208]*, b) PZT sample thinned to 20 µm on gold surface.*

3.3 Fabrication of MEMS Piezoelectric Energy Harvester

As mentioned earlier, bulk piezoceramics are preferred in this study due to their higher output voltage and power levels. Several piezoelectric materials are commercially available and their major properties, especially the important ones for energy harvesting applications and fabrication, are summarized in Table 3.2. As shown in the table, PMN-PT has the highest values for all the parameters. Having high strain coefficient, d_{31}, is highly desired in harvesting applications, since it provides higher voltage outputs. Besides, having higher elastic compliance, PMN-PT has the lowest modulus among the presented materials; thus, makes it possible to develop structures with lower natural frequency. It can also be seen that the mentioned parameters of PZT-5H are also more favorable than PZT-5A for energy harvesting applications. On the other hand, Curie temperatures of PMN-PT and PZT-5H are considerably lower than that of PZT-5A. Curie temperature is the most important parameter when considering the fabrication process. Because, if the temperature of the material exceeds its Curie temperature, the material loses its piezoelectric properties. A low temperature bonding method (~200 °C) is developed to prevent this situation, as described in previous section. However, PMN-PT and PZT-5H cannot be processed even with this low temperature bonding method. Thus, among other high-performance bulk piezoceramics, PZT-5A is chosen due to its compatibility with the fabrication process.

Table 3.2: Comparison of material properties of commonly used piezoelectric materials [41], [111], [209]. *([a] CT: Curie temperature)*

	d_{31} [pm/V]	s_{11}^E [pm^2/N]	$\varepsilon_{33}^T/\varepsilon_0$	ρ [kg/m^3]	CT^a [°C]
PZT-5A	-171	16.4	1700	7750	350
PZT-5H	-274	16.5	3400	7500	230
PMN-PT	-2252	127	5000	7900	130

PZT-5A materials are supplied from Piezo Systems Inc., in a form of 7 cm x 7 cm sheets (Catalog number: T105-A4E-602). Upper and bottom surface of the sheets are coated with nickel. Prior to fabrication, piezoelectric sheets are coated with Cr/Au/In/Au (50nm/0.4µm/3µm/0.2µm). Deposition of these metal layers are required due to the bonding process, as discussed in Section 3.2. After the deposition process, the piezoelectric sheet is diced and cleaned before the fabrication process.

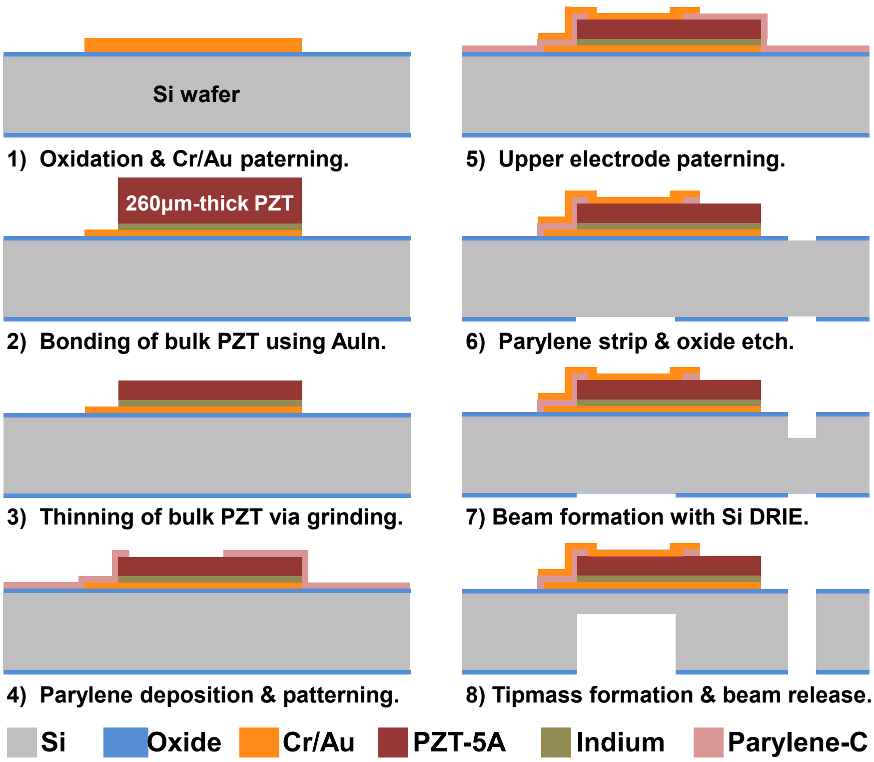

Figure 3.9: Fabrication flow of the MEMS piezoelectric energy harvester [12].

Figure 3.9 shows the fabrication flow of the MEMS piezoelectric energy harvester [97]. A 6-mask process flow is developed, and a (100) Si prime wafer was utilized for the fabrication. Initially, both sides of the wafer are coated with 0.5 µm SiO_2 via STS LPCVD system to provide electrical insulation. The metal deposition step starts with dehydration of the wafer. Then, Bestec sputtering system is utilized for the deposition of the metal layers. First, Cr layer is deposited resulting in thickness of ~10 nm. Second, Au layer is deposited for 50 sec, which results in thickness of ~50 nm. After the metal deposition step, S1813 type of resist is used at 4000 rpm in spin coating system. After the development process, Nanoplus O_2 plasma system is used to ensure the resist-free surface of the exposed area. Then, prior to metal etch process, hard bake is done to make the resist stiffer and prevent delamination of resist during etching. Finally, etching is done via commercial metal etchants (Figure 3.9-1).

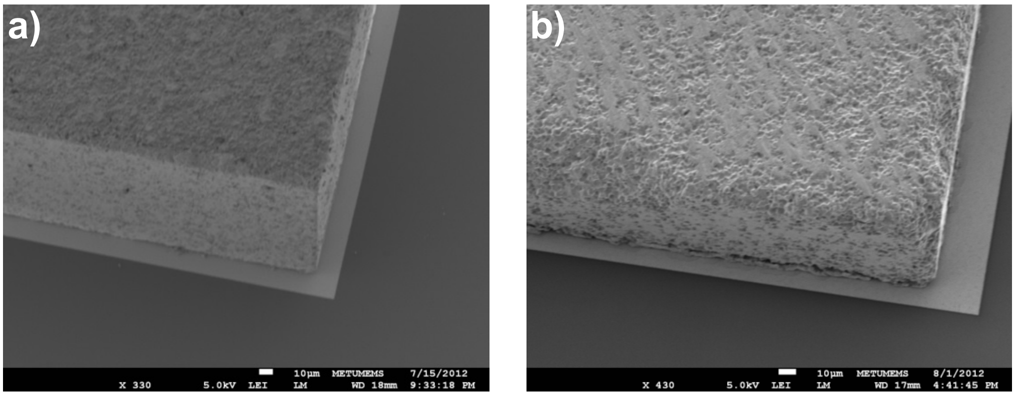

Figure 3.10: Bonded PZT sample a) before thinning, b) after thinning.

After the metal patterning process, diced PZT's are bonded to the process wafer as described in Section 3.2 via a flip-chip bonder device (Figure 3.9-2). After the bonding process, 260 µm-thick PZT pieces are thinned down to 50±2 µm via a grinder system (Figure 3.9-3). Figure 3.10 shows the bonded PZT before and after the thinning process. Surface roughness of around 2-3 µm was observed after the grinding method. The surface roughness can be decreased by using a wheel that is better suited for ceramics. Besides, the drawback of the surface roughness can be eliminated with deposition of thicker metal layer on PZT surface.

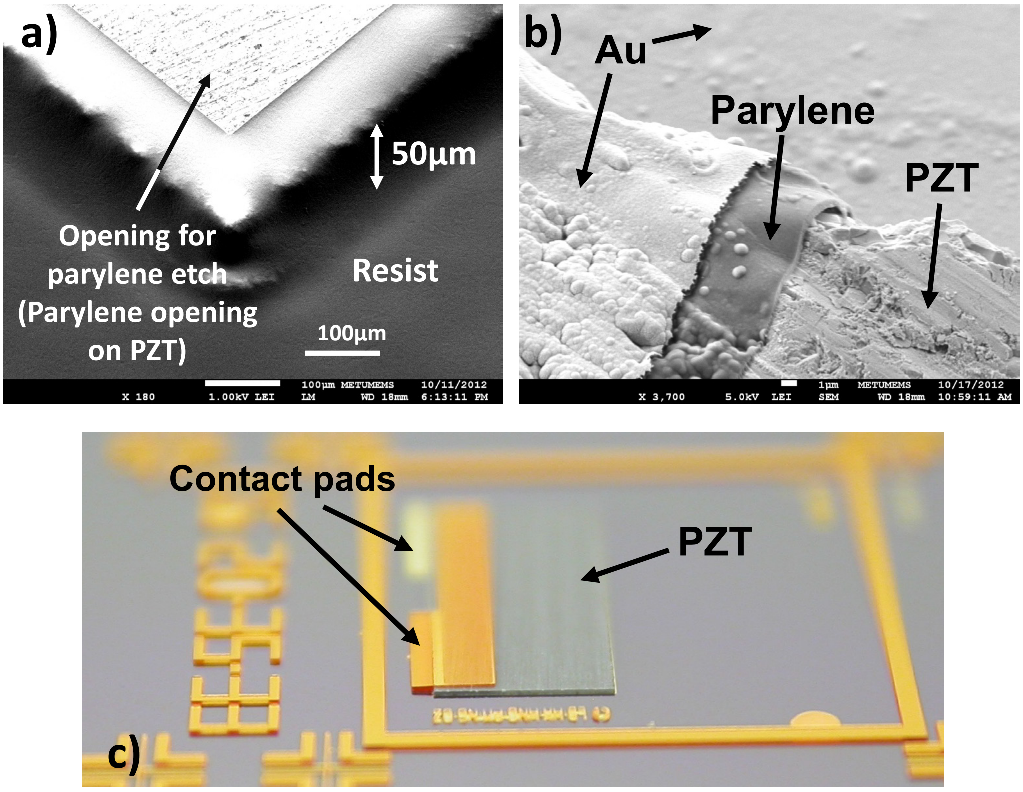

Figure 3.11: a) SEM image of lithography process on a 50 µm-thick PZT on Si, b) close-up view of the upper electrode through PZT edge, c) side view of the harvester after metal patterning.

After the thinning process, 5 µm-thick parylene is coated. The purpose of using parylene is to eliminate short circuit and provide insulation between upper and bottom electrode. Patterning of parylene layer with a standard spin-coated PR mask is not trivial due to thick PZT structures. For such structures, spray coating is advantageous. Therefore, spray coating device is utilized instead of conventional spin coating. Figure 3.11a shows successfully coated 50 µm-thick PZT edge with PR. After lithography step, parylene is etched from the top of the PZT (Figure 3.9-4) with reactive ion etching (RIE). To ensure the removal of parylene, energy dispersive x-ray spectroscopy (EDX) is used. By using this method, the surface materials can be understood. When EDX signals of the top of the PZT surface was acquired, dominant elements were lead (Pb), zirconium (Zr), and titanium (Ti), which are found in PZT-5 ($Pb(Zr_{0.2}Ti0.8)O_3$). Then, metal layers of Cr/Au (50nm/400nm) are deposited via Bestec sputtering system (Figure 3.9-5). Figure 3.10b shows the PZT edge, where gold layer of upper electrode deposited on parylene to ensure isolation of the sidewalls.

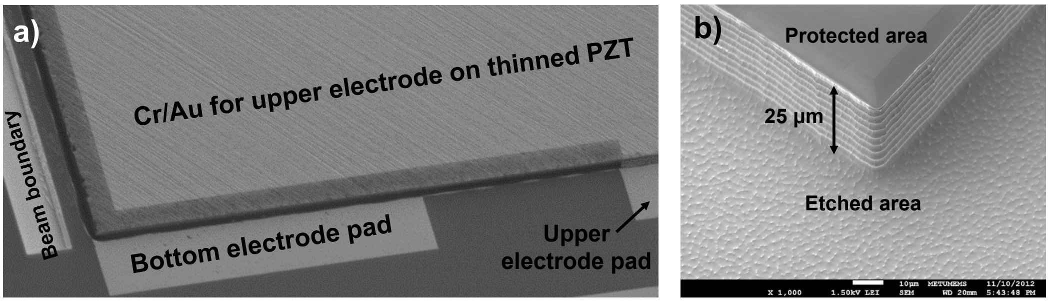

Figure 3.12: SEM image of the harvester showing a) PZT, contact pads, and Si-etched region, b) close-up view from the corner of the cantilever after frontside DRIE.

After upper metal patterning, parylene strip is performed with parylene RIE process (Figure 3.9-6). Then, once again, spray coating is used for lithography. Oxide layer on the front side is patterned with buffered hydro-fluoric acid (BHF) solution. To define the beam dimensions, deep reactive ion etching (DRIE) process is utilized to etch 25 µm silicon from the frontside to form the cantilever beam (Figure 3.9-7 and Figure 3.12b).

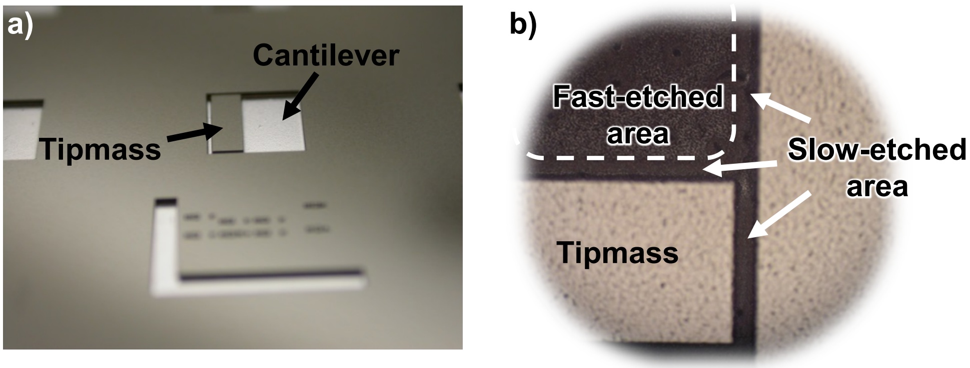

Figure 3.13: Image of the backside of the wafer showing a) tipmass and cantilever structure in the midst of backside DRIE process, b) fast and slow-etched areas.

Similar to the preceding step, backside of the wafer is patterned for oxide etch and Si DRIE processes. Prior to the etching, process wafer is attached to an alumina wafer to prevent the front-side of the wafer and gas leakage during process. During backside silicon DRIE, it is observed that the etch rate is faster in the middle of the exposed area. On the other hand, the area close to the sidewalls is etched slowly. This results in the beam thickness values lower than expected. Figure 3.13a shows image from the backside of the wafer, where Figure 3.13b shows the fast-etched and slow-etched areas. Finally, through silicon etch is done from the backside of the wafer and beams are released (Figure 3.9-8). Figure 3.14 shows the final image of the process wafer.

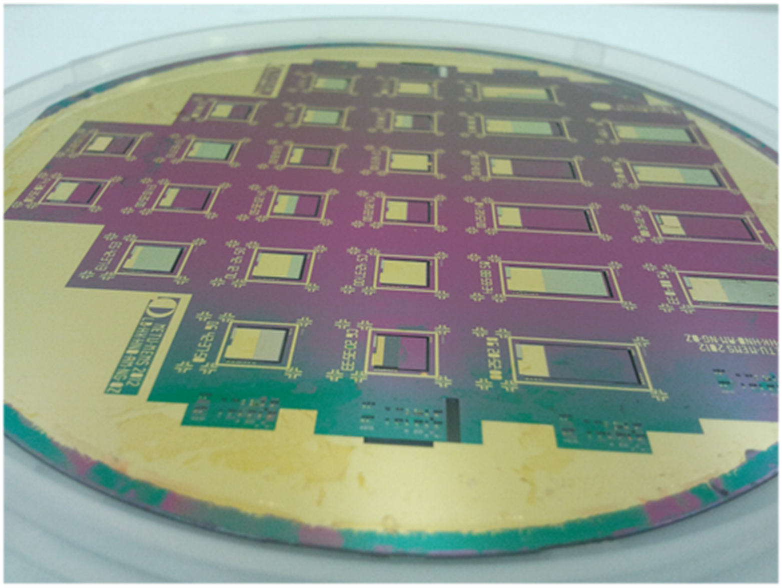

Figure 3.14: Final image of the frontside of the process wafer.

Figure 3.15a shows the cross-sectional view of the fabricated harvester. Due to nonuniform backside DRIE step, the regions close to sidewalls are etched faster than the middle section of the etched region. This results in nonuniform beam thickness, and affects the dynamics of the harvester. Furthermore, the neutral axis of the harvester also varies through the beam length, which might possible degrade the performance of the harvester. Figure 3.15b shows the proposed method of fabrication to prevent nonuniformity. In this process, an SOI wafer is utilized with the same fabrication flow explained in this section. The main difference is the buried-oxide layer between Si handle layer and device layer. The buried-oxide layer acts as an etch stop during the frontside and backside DRIE steps. Therefore, nonuniformity during Si etch process can be prevented.

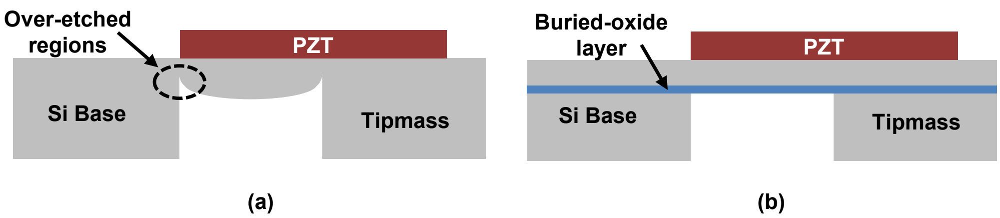

Figure 3.15: Cross-sectional view of a) the fabricated harvester showing over-etched regions around sidewalls, b) the harvester fabricated using SOI wafer.

3.4 Experimental Results

Figure 3.16 shows the experimental setup for the characterization of the fabricated devices. The setup consists of a shaker, a controller system for the shaker, and an oscilloscope. The shaker is vibrated at various frequencies and acceleration levels via the controller system. While vibrating the output voltage of the fabricated devices are measured with the oscilloscope.

Figure 3.17 shows released harvesters with footprint of 6x6 mm^2. In order to investigate the performance of the harvester, it is assembled to a PCB, and mounted on a shaker table. The device is tested under various acceleration (g) levels while varying the frequency of the vibration.

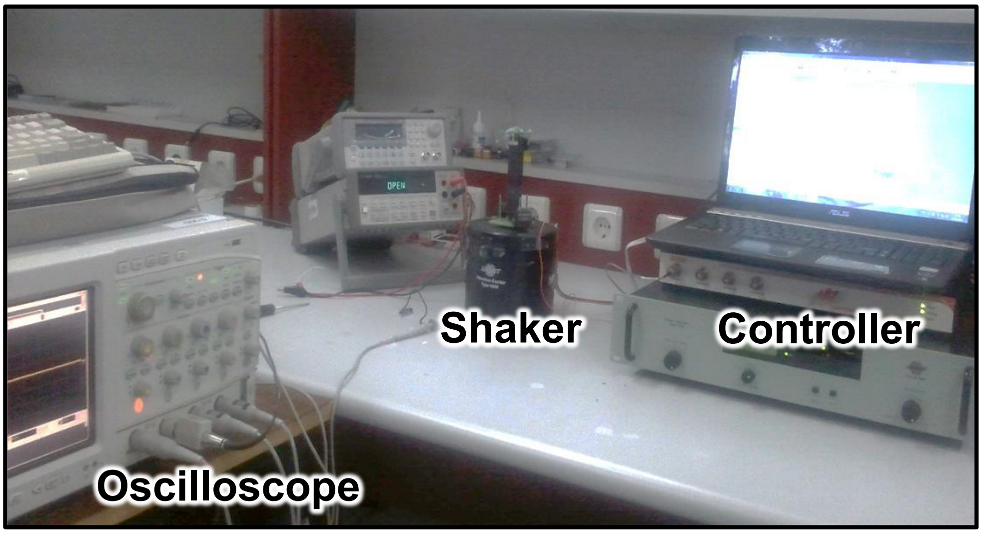

Figure 3.16: Experimental setup for characterization of the harvesters.

The first natural frequency of the MEMS piezoelectric energy harvester was observed at 474 Hz, unlike the simulated value of 550 Hz. The reason of the resonance shift is the non-uniform beam thickness resulting from the final backside DRIE process. The non-uniformity on the beam thickness decreased the thickness of the beam around 5 to 10 μm. Thus, the experimental value is lower than the simulated value.

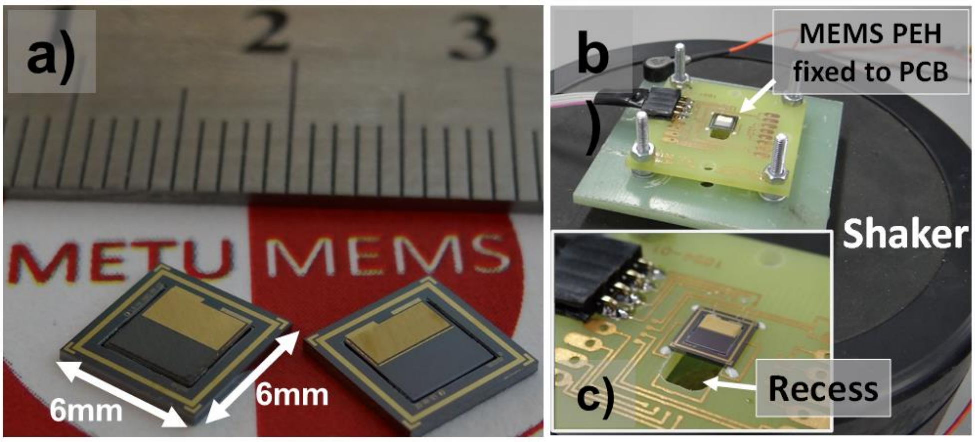

Figure 3.17: a) Fabricated MEMS piezoelectric energy harvesters with 6x6 mm^2 footprint and 20 mm^3 volume, b) MEMS harvester assembled to PCB and mounted on shaker table, c) close-up view of the MEMS harvester on PCB showing recess below the tipmass.

Figure 3.18a shows the generated voltage waveform from the energy harvester at 474 Hz vibration with an acceleration of 0.1g. The generated rms voltage and power are 588 mV and 1.33 μW, respectively for a resistive load of 260 kΩ. The output voltage of the harvester at low acceleration levels is of major importance when the operation medium of the cochlear implants is considered. Regarding Figure 3.18, the value of the generated voltage at 0.1g acceleration is adequate for operation of rectifier circuitry and storage. Moreover, the power output of the harvester can be further increased by increasing the beam thickness uniformity via backside DRIE process optimization: the non-uniform beam thickness shifts the neutral axis of the composite beam, thus reducing the induced stress and the voltage output on the PZT.

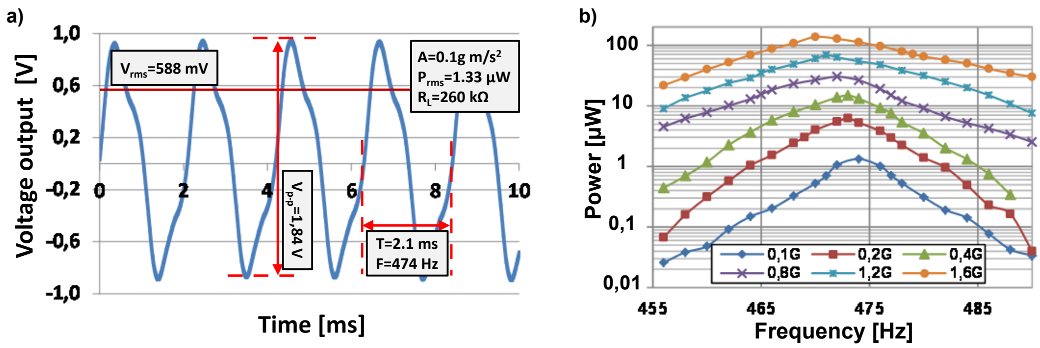

Figure 3.18: a) Generated voltage waveform from the MEMS harvester at its resonance frequency with an input acceleration of 0.1g, b) rms power output at various g levels.

Figure 3.18b shows the effect of vibration frequency and acceleration levels on the power output. The harvester is tested under acceleration levels ranging from 0.1g to 1.6g. A maximum power of 137.5 µW_{RMS} is obtained at 1.6g, while this value decreases to 1.33 µW at 0.1g. It is observed that increased acceleration levels cause an increase in the bandwith, as expected, since it also causes an increase in air damping. Besides, a shift in natural frequency is also observed. This decrease in the natural frequency is a common issue observed in ferroelectric materials, and is due to ferro-elastic hysteresis properties of piezoelectric materials [37], [210].

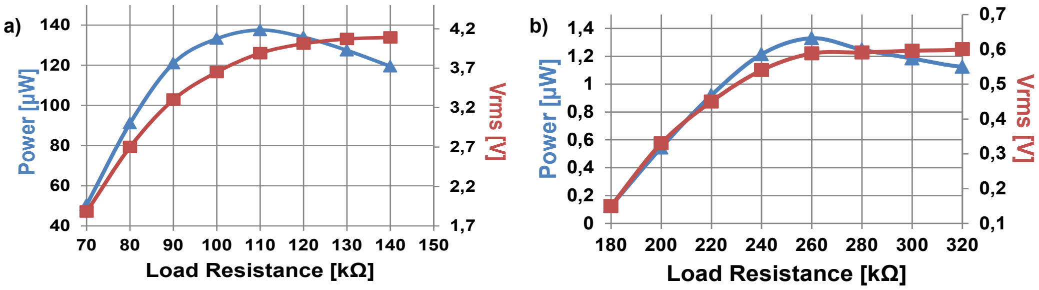

Figure 3.19: Generated rms power and voltage vs. the load resistance at a) 1.6g, b) 0.1g.

Figure 3.19 shows the voltage and power output of the harvester under 1.6g and 0.1g acceleration levels. Due to the mentioned ferro-elastic hysteresis of the piezoelectric materials, and their inherent variable capacitance behavior, under various conditions (such as acceleration, frequency) optimal conditions of the harvester changes. Therefore, various optimal resistances should be found for each case. The optimal load resistance of harvester is investigated under various g-levels. While the structure resonates under 1.6 or 0.1g, the load resistance values are shifted from 70 kΩ to 320 kΩ. Power outputs of the harvester are calculated by considering V_{RMS} values. For the case where input acceleration is 1.6g, it is found that the load resistance of 110 kΩ gives the maximum power output of 137.5 µW. For the latter case, where the input acceleration is 0.1g, maximum power of 1.33 µW is obtained when load resistance of 260 kΩ is used.

The weight of the harvesters vary between 20 to 30 mg depending on the tipmass. This is an acceptable value for a typical middle ear prosthesis. For instance, weight of Medel Corp.'s Vibrant Soundbridge, commercial middle ear hearing prosthesis, is 25 mg [211].

For further investigation of the performance of the fabricated energy harvester is compared with the state-of-the-art MEMS piezoelectric energy harvesters. For comparison purposes, a normalized power density (NPD) formulation is widely used in literature, which is given in Equation 3.1.

Table 3.3 summarizes the performance of the currently developed harvesters with that of the fabricated harvester.

$$NPD = \frac{Power}{Volume \cdot Acceleration^2} \qquad \left[\frac{\mu W}{mm^3 g^2}\right] \tag{3.1}$$

Table 3.3: Comparison of the fabricated MEMS harvester with the state-of-the-art piezoelectric micro generators.

Ref.	Method	Proof Mass	Acc. g (m/s^2)	Vol. mm^3	f_{RES} Hz	Power μW	NPD $\mu W/g^2/mm^3$
This work	Bulk Piezocermics	Si	0.1	20	474	1.3	6.65
			1.6		470	137.5	2.69
[97]		Si	0.1	27	427	1.8	6.74
			1.5		415	160.8	2.65
		W	0.1		167	2.74	10.02
			1.5		154	205.0	3.37
[212]		Si	1	75.7	364	109.4	1.45
				119.8	203	115.5	0.96
[213]	Sol-gel	Si	2	0.65	461	2.2	0.82

The fabricated harvester performed second best result among the harvester using bulk piezoceramics and Si proof mass. However, performance of the fabricated harvester can be improved by performing a uniform backside DRIE process at the last step of the fabrication process (Figure 3.15). This nonuniform process results in variations in the beam thickness along the beam length. Therefore, neutral axis of the beam changes which degrades the voltage output of the harvester. On the other hand, advantage of utilizing bulk piezoceramics instead of sol-gel method can be seen from the comparison chart. The harvester fabricated with sol-gel method has an NPD value of 0.82 even vibrating at 2g. The best performance among the harvesters is obtained by increasing the tipmass weight. An NPD value of 10.02 is achieved by utilizing tungsten tipmass instead of Si [97].

3.5 Summary of the Chapter

In this chapter, fabrication of the MEMS piezoelectric energy harvester is explained. Various methods for bonding are discussed and preferred methods are justified with experiments. Then, conventional MEMS fabrication methods are employed to fabricate the harvester. At the end of the chapter, characterization results of the harvester are given.

CHAPTER 4

DEVELOPMENT OF FULLY IMPLANTABLE AND SELF-POWERED COCHLEAR IMPLANT

This chapter exploits another application of the proposed method of converting eardrum vibrations to electricity is exploited. The chapter starts by giving a brief information about the anatomy of the ear, hearing, and hearing impairment. Then, other drawbacks of the cochlear implants arising due to the external components are pointed, such as damage risk and aesthetic issues. Finally, the proposed application is explained in detail for the development of fully implantable and self-powered cochlear implants, which eliminates several drawbacks of the conventional cochlear implants.

4.1 Anatomy of the Ear

Sound is an oscillation of pressure that is transmitted through a solid, gas, or liquid. The scientific name of the sensing of sound is called audition. As one of the most vital parts of the human sensory system, auditory system helps humans to hear the sound. The audible sound frequency range for humans is between 20 – 20.000 Hz. The auditory system is composed of two main parts, namely peripheral and central auditory system as shown in Figure 4.1. Peripheral auditory system starts with the outer ear, and converts the time and frequency information of the sound pressure waves into action potentials that are used to stimulate the auditory nerve. This information is then transferred to the central auditory system, starting from the cochlear nucleus to the auditory cortex, which is located roughly around Brodmann areas 41 and 42 of the human brain (Figure 4.1b) [98].

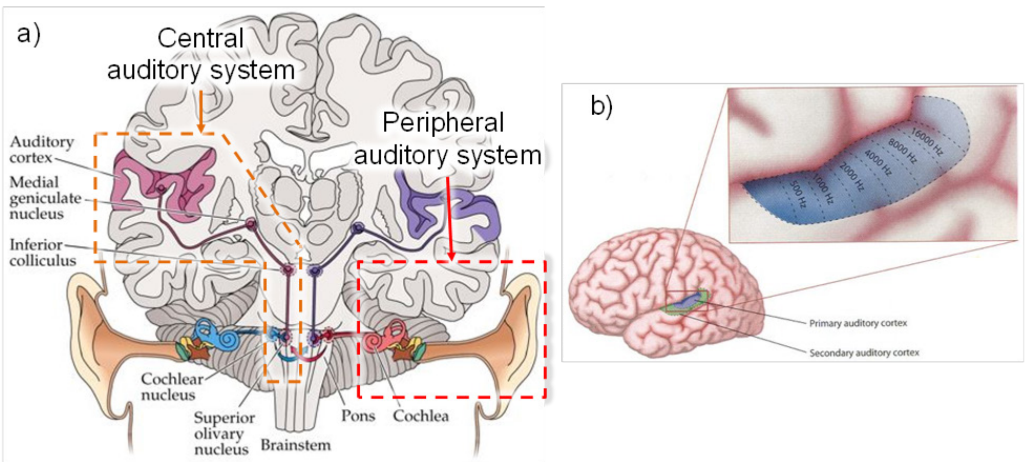

Figure 4.1: The peripheral and central auditory system, b) Broadmann areas 41 and 42 of the human brain where primary and secondary auditory cortex is located.

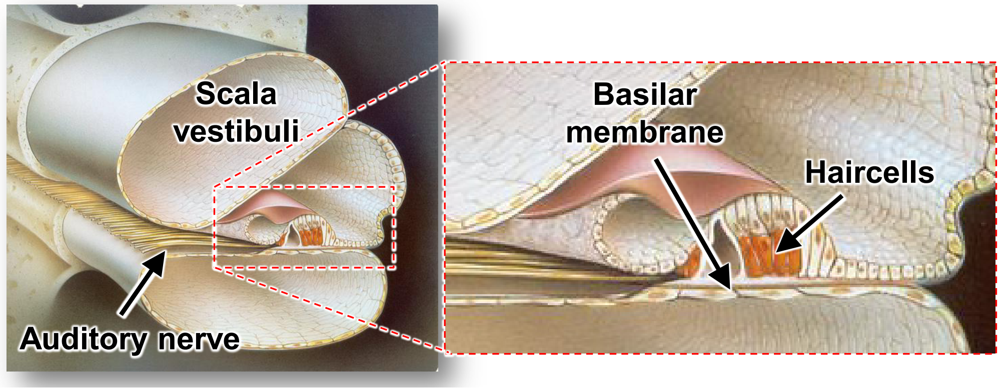

Figure 4.2: Cross-sectional view of the cochlea.

The peripheral auditory system consists of the outer ear, the middle ear, and the inner ear. All these parts play an important role for converting the sound pressure waves into electrical signals. Of interest to the subject of this chapter, the inner ear is composed of the cochlea and non-auditory structures such as vestibular canals, which contributes to balance and the sense of spatial orientation. The cochlea is a 2.5-turn spiral shaped structure, and is divided into three chambers called scala vestibuli, scala tympani, and scala media along its length (Figure 4.2). Both the scala vestibuli and the scala tympani contain a fluid named perilymph, while the scala media contains endolymph. These fluids contain sodium and potassium, which are useful to generate electrical potential for stimulation.

Furthermore, the organ of corti, which has sensory cells called hair cell, is placed on the basilar membrane. The hair cells are the sensory receptors and their function is to generate electrical potential when a sound pressure wave is received. Human basilar membrane has roughly 3.500 inner hair cells and 12.000 outer hair cells. Outer hair cells provide positive mechanical feedback amplification, and this effect is termed as cochlear amplification. Inner hair cells are about 10 to 50 µm in length and they generate electrical stimuli from fluid pressure. The generated electrical signals are used to stimulate the auditory nerve (cochlear nerve), which carries electrical signals to the brain.

4.2 Hearing

The peripheral auditory system is shown in Figure 4.3a. As described earlier, the human peripheral auditory system is capable of sensing sound frequencies ranging from 20 Hz to 20.000 Hz (Figure 4.3b). Firstly, the incoming sound pressure waves hit the pinna (outer ear), and the pinna funnels the incoming sound pressures to the ear canal. The ear canal carries the filtered sound pressure waves to the middle ear. When a sound is directed through the ear canal, the eardrum vibrates depending on the frequency of the sound and converts acoustic sound pressures to mechanical vibrations as explained in Chapter 2.

Ossicles work as a lever mechanism and amplify the mechanical energy applied to the cochlea via stapes. The end section of the stapes is termed as footplate, and is attached to the oval window of the cochlea. Cochlea is responsible from the frequency discrimination of incoming sounds. Upon the vibrations of the oval window, basilar membrane starts to oscillate as well as the cochlear fluid. Depending on the frequency of the sound, specific portions of the basilar membrane resonate (Figure 4.4), and resonating portion causes movement of the hair cells at that section as shown in Figure 4.3c.

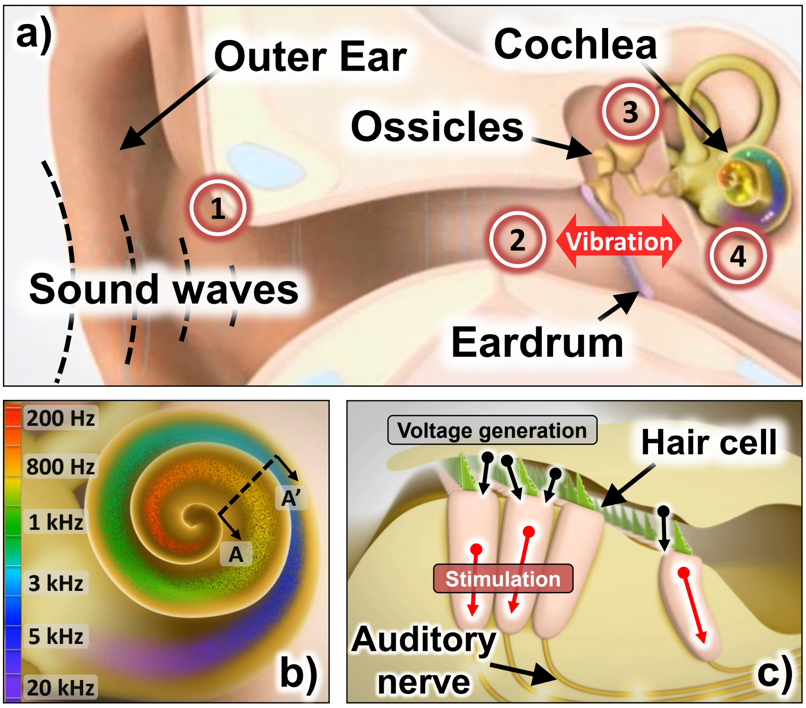

Figure 4.3: a) The peripheral auditory system, b) frequency band of the cochlea, c) voltage generation via haircells and stimulation of auditory nerve within the cochlea.

Deflection of the hair cells causes positively charged ions found in the endolymph to enter the cell. After a chemical reaction, voltage is generated resulting in stimulation of the auditory nerve (Figure 4.3c). Stimulation signals are transferred to the brain, and finally incoming sound is heard.

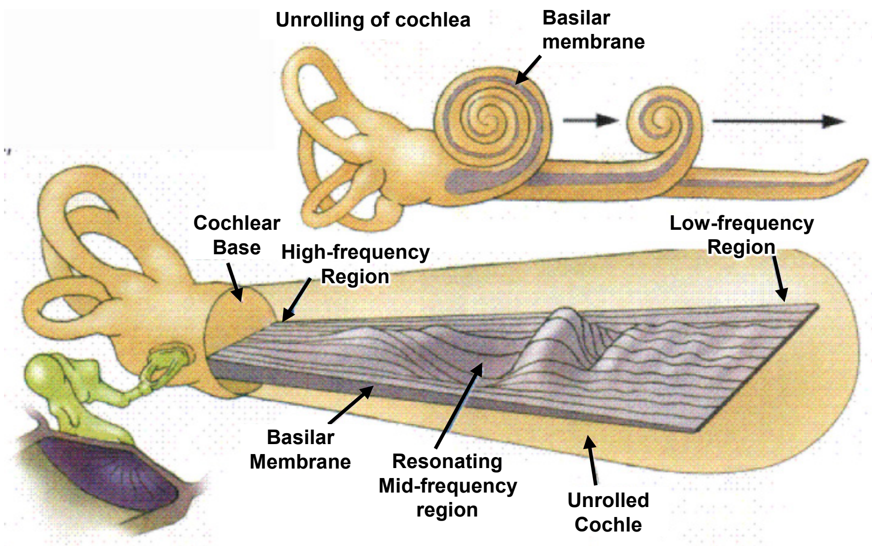

Figure 4.4: Representation of resonating section within basilar membrane [214].

4.3 Hearing Impairment and Cochlear Implants

Deafness is a partial or total inability to hear, and can be classified into three groups as conductive, sensorineural, and mixed deafness. Conductive deafness occurs when sound is not reaching the cochlea. Some of the reasons for this inability are ear canal malformation, malfunction of the ossicles or dysfunction of the eardrum [215]. This type of impairment mostly results in attenuation in the sound level. Sensorineural deafness is mostly due to damage to the hair cells [216]. Damaged hair cells cannot generate voltage required for stimulation, thus resulting in severe-to-profound hearing impairment. Mixed deafness is combination of the conductive and sensorineural type deafness.

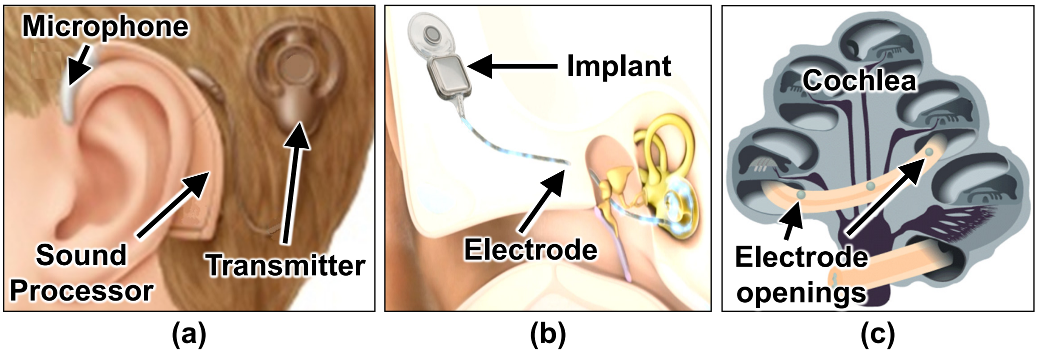

Figure 4.5: Conventional cochlear implants a) external components, b) internal components, c) electrode array placed through the cochlea [217].

Conductive deafness can be treated via hearing aids, which amplify the sound levels through the ear canal. However, sensorineural deafness requires treatment that is more complicated. For the treatment of this type of impairment, cochlear implants have been used for more than 40 years, and today implanted in approximately 220.000 individuals worldwide. Conventional cochlear implants are used for the treatment of the severe-to-profound deafness or sensorineural hearing loss, which results from missing or damaged hair cells. However, utilization of these systems replaces almost all of the natural hearing mechanism with electronic hearing, even though most parts of the hearing system (such as the eardrum and ossicles) are operational. Figure 4.5 shows components of cochlear implants and their placement. Cochlear implants consist of 3 main parts. First part is external to the head, and mounted to the ear. This part is composed of a microphone, a sound processor, a battery, and a transmitter. Second part is the implant, and is surgically implanted into the head. Third part is the electrode, which is placed all the way through the cochlea. The operation of a typical cochlear implant is as follows: microphone, which is mounted on the ear, converts the incoming acoustic sound pressure to electrical signal. Sound processor processes the incoming signals and divides the sounds into a number channels depending on the number of electrode stimulation openings. Then, processed signals are transmitted to the implant wirelessly via the transmitter. Implant receives and sends the signals to the electrode. Finally, electrode stimulates the auditory nerve through the openings placed around the corresponding sound frequency. 8-channel cochlear implants are widely used and are enough for patients to hear daily sounds. Nowadays companies provide up to 20-channel cochlear implants, which provide patients to hear even high frequency musical sounds.

Although, cochlear implants provide hearing to the patients, they have some drawbacks such as battery recharge/replacement problem [9], damage risk of external components [10], especially if exposed to water (shower, rain, pool, etc.), and aesthetic concerns [8]. These drawbacks prevent patients' continuous access to sound. Therefore, researchers in this area try to eliminate this problem via fully implantable middle ear prosthesis systems. Zurcher *et al.* from the Case Western University proposed a MEMS accelerometer, which can be used as an implantable middle ear microphone [56]. The device is used to sense the frequency of the vibrations of the eardrum or the ossicles and supplies the generated signals to the processor. The researchers also proposed to implant all electronic components of the conventional cochlear implants, such as processor, power management unit, and battery. Although, this method proposes a fully implantable system, it does not eliminate the battery replacement/recharge problem. Besides, placing all electronic components inside the skin might not be an easy operation for the surgeon. Another method is proposed by Luo *et al.* from the University of Washington in 2013 [218]. In this study, a MEMS piezoelectric transducer is designed for intracochlear applications. A 1-mm wide and 10-mm long probe is designed to be served as an acoustic actuator in aqueous environment. However, energy related problems are not emphasized in this study. In this regard, a cochlear implant system is desired which is not only fully implantable but also self-powered. The proposed method in the Chapter 2 is aimed to eliminate the energy related problems of the conventional cochlear implants. On the other hand, it cannot eliminate the external components of the cochlear implants. Therefore, in the next section a new method will be explained to eliminate both energy related and external components' damage risk problems.

4.4 Proposed Application: Utilizing Multi-Frequency Energy Harvester Mounted on the Eardrum for Development of a Fully Implantable and Self-Powered Cochlear Implant

Figure 4.6 conceptually depicts the proposed method and placement of the MEMS harvester implanted to the middle ear, more specifically inner side of the eardrum [11–13]. The harvester consists of several cantilever beams each resonating at a specific frequency within hearing band. In this sense, the frequency selectivity of the method is similar to that of cochlea (Figure 4.7a-b); thus, can be thought of an electromechanical system that is mimicking the natural operation of the cochlea.

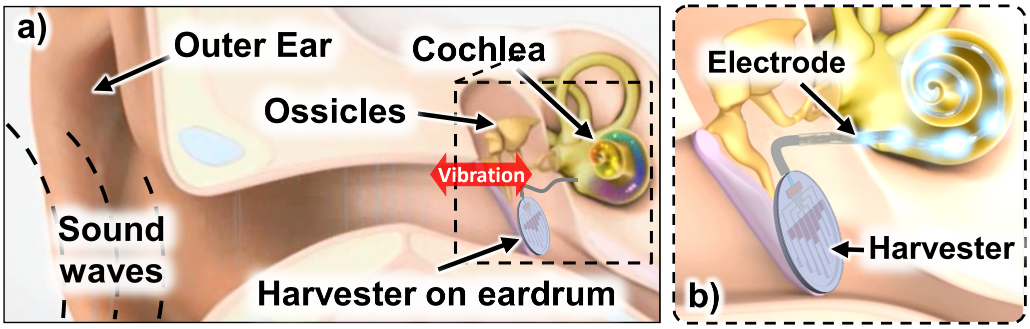

Figure 4.6: a) Proposed method and placement of MEMS multi-frequency harvester for stimulating auditory nerve [11–13], *b) close-up view of the middle ear showing the harvester and electrode array for stimulating via the generated electrical signals of predetermined frequency* [217].

When an acoustic sound pressure impinges on the eardrum, the harvester starts to vibrate. The vibration triggers the cantilever beams with matching resonance frequencies. Triggered beams generate an electrical output considerably higher than those of the other cantilevers. Generated voltage is transferred to the corresponding section of the auditory nerve via the electrode, and the stimulation of the nerve occurs.

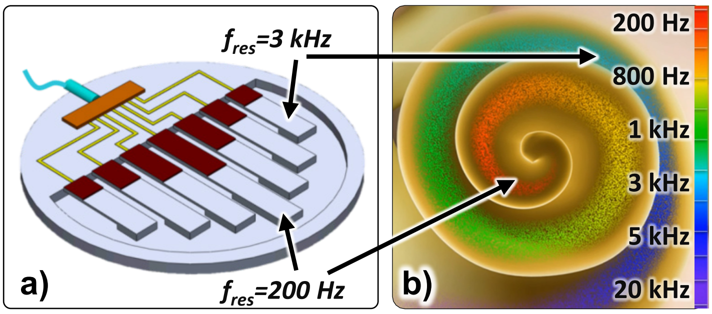

Figure 4.7: a) Proposed multi-frequency MEMS harvester that natural frequency of each cantilever corresponds to a frequency band in cochlea, similar to a frequency discretized cochlea model, b) frequency range of cochlea [217].

Electrical output of each cantilever is connected to the relevant section of the cochlea through a conventional electrode array structure, which is depicted in Figure 4.8. The necessary voltage for stimulation is between -50 to -100 mV, proportional to the incoming SPL.

The proposed method makes use of the operational organ (eardrum), and generates required signal directly from them. Therefore, being a self-powered system, this method eliminates the need for battery and provides patients' continuous access to sound. In addition, being a fully implantable system, there is no damage risk for the outer components as in the conventional cochlear implants. Thus, patients do not have to take out the external components of the cochlear implants when they enter to an aqueous environment, such as pool, shower, or rain. Besides, this method also eliminates patients' aesthetic concerns, since the implant is not visible from outside of the body.

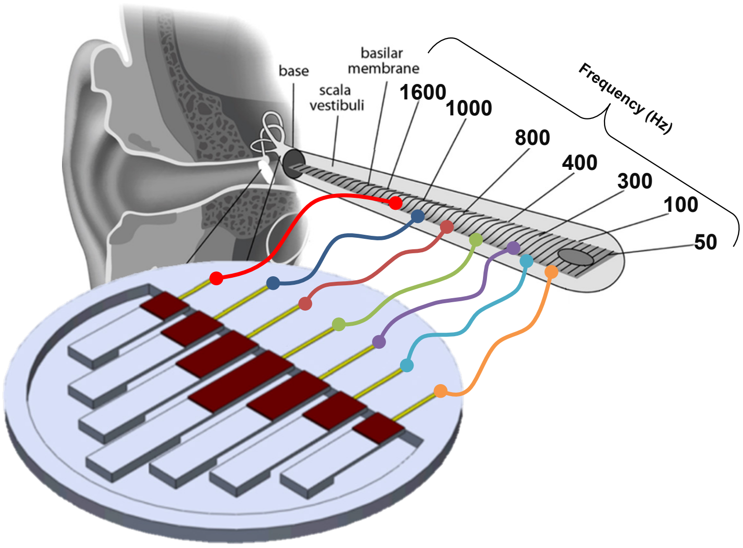

Figure 4.8: Image showing voltage connections of the cantilevers with the corresponding frequency band within the cochlea.

Another advantage of the proposed system is that it can be customized according to the patient's needs. The level of hearing loss varies from person to person. In some cases, a person might experience a hearing loss for high frequency sounds, and vice versa. With the proposed method, it is possible to design a custom CI for each patient since the number and resonance frequency of the cantilevers, and the placement of the electrodes inside cochlea can be adjusted according to the malfunctioning region. On the other hand, the healthy region maintains its natural hearing function independent of the implant.

Consequently, with the proposed method in this chapter, it is possible to develop a fully implantable system mimicking the natural operation of the cochlea, which eliminates damage risk of the outer components of the conventional cochlear implants. Furthermore, being a fully implantable system, aesthetic concerns of the patients are also disregarded. Another advantage of the system is its ability to generate electricity from the eardrum vibrations; thus eliminating the need for battery. In this regard, a continuous access to sound can be provided to the patients.

4.5 Summary of the Chapter

In this chapter, a new type of cochlear implant is proposed. Being a fully implantable device, the proposed method eliminates the damage risk of the conventional cochlear implants. Besides, by making use of the generated electrical signals of cantilever beams with predetermined frequency, it is able to supply its own energy, thus eliminating the battery need of cochlear implants. The concept and the details of the proposed application are explained.

CHAPTER 5

CONCLUSIONS AND FUTURE WORK

In this research, a micro-scale piezoelectric energy harvester is developed to convert the eardrum vibrations to electricity. Two novel applications of the proposed method are explained. For this purpose, modeling, design, simulation, optimization, and fabrication of the harvester are presented. Accomplished tasks with this research can be summarized as follows:

- A novel application of energy harvesting is proposed, which is converting the eardrum vibrations to electricity. Two possible use of the proposed application is mentioned. First one is to supply electrical power with the generated electricity to eliminate the battery need of the cochlear implants. Second one is to transfer the generated frequency-discriminated electrical signals to the corresponding sections within the cochlea via a multi-frequency harvester which electromechanically mimics the operation of cochlea. Therefore, with the application of the second method, it is possible to develop a new generation fully implantable and self-powered cochlear implant.
- Theory of piezoelectric energy harvesters is examined to understand the proper modeling and design approach for the subject of the thesis. For this purpose, lumped parameter modeling, distributed parameter modeling, and finite element modeling (FEM) approaches are investigated. Among these methods, FEM is chosen for the further modeling attempts due to its flexibility and applicability to the operational conditions.
- Important points of the modeling are explained in detail, such as material models and element types. For the verification of the developed models, a macro-scale prototype is fabricated and tested.
- An FE model of the energy harvester is explained considering the fabrication issues, such as used wafer type, relative placement of the harvester with respect to the wafer flat, and orientation of the piezoelectric material.
- Due to the comparable mass and stiffness parameters of the harvester with those of the eardrum, it is decided to analyze the dynamics of the coupled structure, instead of considering the dynamics of the energy harvester alone. Thus, a circular membrane model is developed using FE modeling to form a basis for the eardrum model. For verification of the developed model, well-known natural frequency formula is modified to compare the developed model with the distributed parameter model.
- After development of the membrane model via FEM, eardrum is modeled considering the dynamics of the middle ear. Important aspects of the eardrum, and its model are emphasized and discussed in detail. Two different methods are used to fit the theoretical results obtained with the developed model to the published experimental results. In order to adjust the unknown mechanical parameters of the system, an optimization routine is developed using built-in tools of the FE program.

- The harvester model and the eardrum model are incorporated in FE environment, and their coupled behavior is investigated for further analysis. Moreover, the gravitational effects and orientation of the eardrum is considered in the simulations. It is observed that instead of the first transverse mode of the coupled structure, second transverse mode (corresponds to fourth natural frequency) gives the highest voltage from the piezoelectric material due to the opposite motion of the coupled structures.
- For the optimization of the design parameters, an optimization routine is developed utilizing the built-in optimization tool of the FE program. Several aspects of the chosen optimization method is pointed. Besides, meshing features of the models are emphasized, due to its considerable effect on the optimization time. Optimization of the harvester is accomplished considering several sound frequencies within the hearing band (750 Hz, 1 kHz, and 1.5 kHz). Furthermore, developed routine is used to optimize design parameters considering fabrication issues, such as used wafer type.
- For the fabrication of optimized harvester, among several methods, bulk piezoceramics is chosen due to its high piezoelectric strain constant and charge capacity, low-temperature process. Especially its high voltage output is desirable for the proposed application.
- Several methods are mentioned for integration of bulk piezoceramics. Among these methods, gold thermocompression and gold-indium bonding are investigated. In order to quantify the shear strength of the bonded chips, a shear test apparatus is designed and manufactured. Then, it is experimentally shown that the gold thermocompression method cannot be used for the bonding of piezoceramics due to its high temperature requirement for desirable shear strength. On the other hand, gold-indium bonding method is shown to survive even under grinding process, which is the subsequent process in the fabrication flow.
- After obtaining satisfactory results with the gold-indium bonding method, a fabrication flow is developed. In order to handle and process brittle structures, such as PZT, a wafer-level integration method is developed via parylene coating at room temperature and zero applied pressure, which is explained in detail in Appendix A. However, to prevent contamination issues, flip-chip bonding device is used during bonding process, which is also described in detail. Then, thinning of the bonded piezoceramics is done via a grinder system and bonded PZT's are thinned down from 260 μm to 20 μm. Then, following standard MEMS fabrication processes, a MEMS piezoelectric energy harvester is fabricated.
- The harvester is assembled to a PCB and mounted to shaker table to investigate its performance under variety of acceleration levels. The harvester is tested under acceleration levels ranging from 0.1g to 1.6g. It is experimentally shown that the fabricated harvester is able to generate up to 137.5 μW and 1.33 μW of rms power under acceleration levels of 1.6g and 0.1g when connected to resistive loads of 110 kΩ and 260 kΩ, respectively.
- In order to compare the performance of the fabricated harvester with the state-of-the-art MEMS piezoelectric energy harvesters, widely referred normalized power density (NPD) formula is utilized. It is shown that fabricated device yields the best result for 0.1g and the second best for 1.6g among other published harvesters. Furthermore, several reasons that might affect the performance are mentioned. Especially, non-uniform beam thickness is thought to be the major reason for the shift of the resonance frequency and lower voltage output. It is concluded that, it is possible to increase the performance of the harvester by optimizing the process parameters.

Future work of the presented research can be summarized as follows:

- *In-vivo* and *in-vitro* experiments should be conducted and clinical data should be obtained for performance measurements of the harvester.
- The developed eardrum model should be experimentally verified to obtain a more accurate representation of the coupled structure.

- Although flip-chip bonding device gives flexibility during bonding process, a wafer-level bonding is required for batch processing.
- Further investigation of bonding processes is required in order to characterize their long-time behavior. Oxidation of the indium layer degrades the bonding quality; thus, indium coating process should be utilized for better bonding results. Due to the limited access to the indium evaporator, it could not be characterized sufficiently. On the other hand, various bonding methods such as AuSn can be utilized in order to increase the bonding quality.
- Grinding process should be optimized for further thinning of the PZT structures. Due to the limited access to the device, standard ceramic parameters are utilized as well as standard grinding wheels. Therefore, the thinning process could not be optimized accordingly, resulting in increased thickness and surface roughness.
- Optimization of the backside DRIE process is required to obtain cantilever beam structures with uniform thickness.
- Performance of the fabricated harvester should be investigated while bonded to an eardrum and clinical data should be obtained.
- Another batch should be processed with SOI wafers.
- Packaging of the device should be considered during fabrication process.
- Depending on the obtained voltage forms, an electronic circuitry can be developed to shape the obtained waveforms.

REFERENCES

[1] K. D. Wise, "Integrated sensors, microactuators, and microsystems (MEMS)," *Special Issue of the IEEE Proceedings*, pp. 1531–1787, 1998.

[2] R. Amirtharajah, J. Collier, J. Siebert, B. Zhou, and A. Chandrakasan, "DSPs for Energy Harvesting Sensors: Applications and Architectures," *IEEE Pervasive Computing*, vol. 4, no. 3, pp. 72–79, Jul. 2005.

[3] G. Voskerician, M. S. Shive, R. S. Shawgo, H. von Recum, J. M. Anderson, M. J. Cima, and R. Langer, "Biocompatibility and biofouling of MEMS drug delivery devices," *Biomaterials Journal*, vol. 24, no. 11, pp. 1959–1967, May 2003.

[4] G. Kotzar, M. Freas, P. Abel, A. Fleischman, S. Roy, C. Zorman, J. M. Moran, and J. Melzak, "Evaluation of MEMS materials of construction for implantable medical devices," *Biomaterials Journal*, vol. 23, no. 13, pp. 2737–2750, Jul. 2002.

[5] S. Takeuchi, T. Suzuki, K. Mabuchi, and H. Fujita, "3D flexible multichannel neural probe array," *Journal of Micromechanics and Microengineering*, vol. 14, no. 1, pp. 104–107, 2004.

[6] M. R. Prausnitz, "Microneedles for transdermal drug delivery," *Advanced Drug Delivery Reviews*, vol. 56, no. 5, pp. 581–7, Mar. 2004.

[7] J. Bryzek, R. Mayer, and P. Barth, "Disposable blood pressure sensors with digital on-chop laser trimming," in *Proceedings Intl. Conf. Solid-State Sens. Actuators Microsystems (Transducers)*, 1988, pp. 121–122.

[8] M. K. Cosetti and S. B. Waltzman, "Cochlear implants: current status and future potential," *Expert Review of Medical Devices*, vol. 8, no. 3, pp. 389–401, May 2011.

[9] F.-G. Zeng, S. Rebscher, W. Harrison, X. Sun, and H. Feng, "Cochlear implants: system design, integration, and evaluation," *IEEE Reviews in Biomedical Engineering*, vol. 1, pp. 115–42, Jan. 2008.

[10] J. P. Harris, J. P. Anderson, and R. Novak, "An outcomes study of cochlear implants in deaf patients. Audiologic, economic, and quality-of-life changes," *Archives of Otolaryngology-Head & Neck Surgery*, vol. 121, no. 4, pp. 398–404, Apr. 1995.

[11] L. Beker, N. Goksu, and H. Kulah, "An energy harvesting cochlear implant," WO2013081560, patent pending.

[12] L. Beker, O. Zorlu, N. Goksu, and H. Kulah, "Stimulating auditory nerve with MEMS harvesters for fully implantable and self-powered cochlear implants," in *Proceedings Intl. Conf. Solid-State Sens. Actuators Microsystems (Transducers)*, 2013.

[13] L. Beker, Ö. Zorlu, N. Goksu, and H. Kulah, "A MEMS transducer for fully implantable and self-powered cochlear implant," *Journal of Microelectromechanical Systems*, to be submitted.

[14] K. Najafi, T. Galchev, E. E. Aktakka, R. L. Peterson, and J. McCullagh, "Microsystems for energy harvesting," in *Proceedings Intl. Conf. Solid-State Sens. Actuators Microsystems (Transducers)*, 2011, pp. 1845–1850.

[15] S. Roundy, "Energy scavenging for wireless sensor nodes with a focus on vibration to electricity conversion," Ph.D Thesis, University of California, Berkeley, 2003.

[16] S. Roundy, P. Wright, and K. Pister, "Micro-electrostatic vibration-to-electricity converters," in *Proceedings Intl. Mechanical Engineering Congress & Exposition (IMECE)*, 2002.

[17] M. Stordeur and I. Stark, "Low power thermoelectric generator-self-sufficient energy supply for micro systems," in *Proceedings Intl. Conf. Thermoelectrics*, 1997, pp. 575–577.

[18] N. S. Shenck and J. A. Paradiso, "Energy scavenging with shoe-mounted piezoelectrics," *IEEE Micro*, vol. 21, no. 3, pp. 30–42, 2001.

[19] A. Mehra, A. A. Ayon, I. A. Waitz, M. A. Schmidt, and C. M. Spadaccini, "A six-wafer combustion system for a silicon micro gas turbine engine," *Journal of Microelectromechanical Systems*, vol. 9, no. 4, pp. 517–527, Dec. 2000.

[20] K. A. Cook-Chennault, N. Thambi, and A. M. Sastry, "Powering MEMS portable devices—a review of non-regenerative and regenerative power supply systems with special emphasis on piezoelectric energy harvesting systems," *Smart Materials and Structures*, vol. 17, no. 4, p. 043001, Aug. 2008.

[21] R. Torah, P. Glynne-Jones, M. Tudor, T. O'Donnell, S. Roy, and S. Beeby, "Self-powered autonomous wireless sensor node using vibration energy harvesting," *Measurement Science and Technology*, vol. 19, no. 12, pp. 1–8, Dec. 2008.

[22] P. Glynne-Jones, M. J. Tudor, S. P. Beeby, and N. M. White, "An electromagnetic, vibration-powered generator for intelligent sensor systems," *Sensors and Actuators A: Physical*, vol. 110, no. 1–3, pp. 344–349, Feb. 2004.

[23] W. Shen, S. Zhu, and Y. Xu, "An experimental study on self-powered vibration control and monitoring system using electromagnetic TMD and wireless sensors," *Sensors and Actuators A: Physical*, vol. 180, pp. 166–176, Jun. 2012.

[24] P. C.-P. Chao, "Energy harvesting electronics for vibratory devices in self-powered sensors," *IEEE Sensors Journal*, vol. 11, no. 12, pp. 3106–3121, Dec. 2011.

[25] D. Zhu, S. P. Beeby, M. J. Tudor, and N. R. Harris, "A credit card sized self powered smart sensor node," *Sensors and Actuators A: Physical*, vol. 169, no. 2, pp. 317–325, Oct. 2011.

[26] M. Wischke, M. Masur, M. Kroner, and P. Woias, "Vibration harvesting in traffic tunnels to power wireless sensor nodes," *Smart Materials and Structures*, vol. 20, no. 8, pp. 1–8, 2011.

[27] C. B. Williams and R. B. Yates, "Analysis of a micro-electric generator for microsystems," *Sensors and Actuators A: Physical*, vol. 52, no. 1, pp. 8–11, 1996.

[28] C. B. Williams, C. Shearwood, M. A. Harradine, P. H. Mellor, T. S. Birch, and R. B. Yates, "Development of an electromagnetic micro-generator," *IEEE Proceedings Circuits, Devices and Systems*, vol. 148, no. 6, p. 337, 2001.

[29] M. El-hami, P. Glynne-Jones, N. M. White, M. Hill, S. Beeby, E. James, A. D. Brown, and J. N. Ross, "Design and fabrication of a new vibration-based electromechanical power generator," *Sensors and Actuators A: Physical*, vol. 92, no. 1–3, pp. 335–342, Aug. 2001.

[30] X. Cao, W.-J. Chiang, Y.-C. King, and Y.-K. Lee, "Electromagnetic energy harvesting circuit with feedforward and feedback DC–DC PWM boost converter for vibration power generator system," *IEEE Transactions on Power Electronics*, vol. 22, no. 2, pp. 679–685, Mar. 2007.

[31] S. Roundy and E. Takahashi, "A Planar electromagnetic energy harvesting transducer using a multi-pole magnetic plate," *Sensors and Actuators A: Physical*, vol. 195, pp. 98–104, Mar. 2013.

[32] C. R. Saha, T. O'Donnell, H. Loder, S. Beeby, and J. Tudor, "Optimization of an electromagnetic energy harvesting device," *IEEE Transactions on Magnetics*, vol. 42, no. 10, pp. 3509–3511, Oct. 2006.

[33] H. Kulah and K. Najafi, "An electromagnetic micro power generator for low-frequency environmental vibrations," in *Proceedings IEEE Intl. Conf. Micro Electro Mechanical Systems (MEMS)*, 2004, pp. 237–240.

[34] I. Sari, "Design, fabrication and implementation of a vibration based MEMS energy scavenger for wireless microsystems," Ph.D. Thesis, Middle East Technical University, 2008.

[35] Ö. Zorlu, E. T. Topal, and H. Kulah, “A vibration-based electromagnetic energy harvester using mechanical frequency up-conversion method,” *IEEE Sensors Journal*, vol. 11, no. 2, pp. 481–488, Feb. 2011.

[36] T. Galchev, H. Kim, and K. Najafi, “Micro power generator for harvesting low-frequency and nonperiodic vibrations,” *Journal of Microelectromechanical Systems*, vol. 20, no. 4, pp. 852–866, 2011.

[37] E. E. Aktakka, “Integration of Bulk Piezoelectric Materials into Microsystems,” University of Michigan, Ph.D. Thesis, 2012.

[38] P. Basset, D. Galayko, P. Mahmood, F. Marty, A. Dudka, and T. Bourouina, “A batch-fabricated and electret-free silicon electrostatic vibration energy harvester,” *Journal of Micromechanics and Microengineering*, vol. 19, no. 11, 2009.

[39] IEEE, “IEEE standards on piezoelectricity,” 1987.

[40] G. Lippmann, “Principe de la conservation de l’ecetricite,” *Annales de Chimie et de Physique*, vol. 24, p. 145, 1881.

[41] A. Erturk and D. J. Inman, *Piezoelectric energy harvesting*. Wiley, 2011.

[42] M. Renaud, “Piezoelectric Energy Harvesters for Wireless Sensor Networks,” Ph.D. Thesis, Katholieke University, 2009.

[43] Y. B. Jeon, R. Sood, J. -h. Jeong, and S.-G. Kim, “MEMS power generator with transverse mode thin film PZT,” *Sensors and Actuators A: Physical*, vol. 122, no. 1, pp. 16–22, Jul. 2005.

[44] A. Hajati, “Ultra Wide-Bandwidth Micro Energy Harvester,” Massachusetts Institute of Technology, Ph.D. Thesis, 2011.

[45] R. R. Richardson, J. A. Miller, and W. M. Reichert, “Polyimides as biomaterials: preliminary biocompatibility testing,” *Biomaterials Journal*, vol. 14, no. 8, pp. 627–635, Jan. 1993.

[46] S. Nancy, “Literature review: biological safety of Parylene C,” *Medical Plastics and Biomaterials*, vol. 3, pp. 30–35, 1996.

[47] K. J. Rebello, “Applications of MEMS in surgery,” *Proceedings of the IEEE*, vol. 92, no. 1, pp. 43–55, Jan. 2004.

[48] I. Ladabaum, X. Jin, H. T. Soh, A. Atalar, and B. T. Khuri-Yakub, “Surface micromachined capacitive ultrasonic transducers,” *IEEE Transactions on Ultrasonics, Ferroelectrics, and Frequency Control*, vol. 45, no. 3, pp. 678–90, Jan. 1998.

[49] I. G. Mina, H. Kim, I. Kim, S. K. Park, K. Choi, T. N. Jackson, R. L. Tutwiler, and S. Trolier-McKinstry, “High frequency piezoelectric MEMS ultrasound transducers,” *IEEE Transactions on Ultrasonics, Ferroelectrics, and Frequency Control*, vol. 54, no. 12, pp. 2422–30, Dec. 2007.

[50] O. Oralkan, A. S. Ergun, J. A. Johnson, M. Karaman, T. H. Lee, and B. T. Khuri-Yakub, “Volumetric ultrasound imaging using 2-D CMUT arrays,” *IEEE Transactions on Ultrasonics, Ferroelectrics and Frequency Control*, vol. 50, no. 11, pp. 1581–1594, Nov. 2003.

[51] J. Knight, J. McLean, and F. L. Degertekin, “Low temperature fabrication of immersion capacitive micromachined ultrasonic transducers on silicon and dielectric substrates,” *IEEE Transactions on Ultrasonics, Ferroelectrics and Frequency Control*, vol. 51, no. 10, pp. 1324–1333, Oct. 2004.

[52] S. Shelton, M.-L. Chan, H. Park, D. Horsley, B. Boser, I. Izyumin, R. Przybyla, T. Frey, M. Judy, K. Nunan, F. Sammoura, and K. Yang, “CMOS-compatible AlN piezoelectric micromachined ultrasonic transducers,” in *IEEE Intl. Symposium on Ultrasonics*, 2009, pp. 402–405.

[53] F. N. Pirmoradi, K. Ou, J. K. Jackson, K. Letchford, J. Cui, K. T. Wolf, F. Graber, T. Zhao, J. A. Matsubara, H. Burt, M. Chiao, and L. Lin, “Controlled delivery of antiangiogenic drug to human eye tissue using a MEMS device,” in *Proceedings IEEE Intl. Conf. Micro Electro Mechanical Systems (MEMS)*, 2013, pp. 1–4.

[54] W. H. O. (WHO), “Deafness and hearing loss estimates,” 2013. [Online]. Available: http://www.who.int/mediacentre/factsheets/fs300/en/index.html. [Accessed: 11-Mar-2013].

[55] J. Georgiou and C. Toumazou, “A 126-/spl mu/W cochlear chip for a totally implantable system,” *IEEE Journal of Solid-State Circuits*, vol. 40, no. 2, pp. 430–443, Feb. 2005.

[56] M. A. Zurcher, D. J. Young, M. Semaan, C. A. Megerian, and W. H. Ko, “MEMS middle ear acoustic sensor for a fully implantable cochlear prosthesis,” in *Proceedings IEEE Intl. Conf. Micro Electro Mechanical Systems (MEMS)*, 2007, pp. 11–14.

[57] “Online hearing tests, hearing exams, free sound booth hearing test.” [Online]. Available: http://www.stanfordhearingaids.com/online-hearing-test.php. [Accessed: 10-May-2013].

[58] L. Gu, “Low-frequency piezoelectric energy harvesting prototype suitable for the MEMS implementation,” *Microelectronics Journal*, vol. 42, no. 2, pp. 277–282, Feb. 2011.

[59] A. Erturk and D. J. Inman, “Issues in mathematical modeling of piezoelectric energy harvesters,” *Smart Materials and Structures*, vol. 17, no. 6, 2008.

[60] A. M. Flynn and S. R. Sanders, “Fundamental limits on energy transfer and circuit considerations for piezoelectric transformers,” *IEEE Transactions on Power Electronics*, vol. 17, no. 1, pp. 8–14, 2002.

[61] N. E. DuToit, B. L. Wardle, and S. G. Kim, “Design considerations for MEMS-scale piezoelectric mechanical vibration energy harvesters,” *Journal of Integrated Ferroelectrics*, vol. 71, no. 1, pp. 121–160, Jul. 2005.

[62] S. Priya, “Advances in energy harvesting using low profile piezoelectric transducers,” *Journal of Electroceramics*, vol. 19, no. 1, pp. 167–184, Mar. 2007.

[63] F. M. Daqaq, J. M. Renno, J. R. Farmer, and D. J. Inman, “Effects of system parameters and damping on an optimal vibration-based energy harvester,” in *Proceedings AIAA/ASME/ASCE/AHS/ASC Structures, Structural Dynamics, and Materials Conference*, 2007.

[64] A. Erturk, “Electromechanical Modeling of Piezoelectric Energy Harvesters,” Ph.D. Thesis, Virginia Polytechnic Institute and State University, 2009.

[65] J. W. Strutt, *The theory of sound*. London, UK: MacMillan Company, 1894.

[66] G. Wang, “Analysis of bimorph piezoelectric beam energy harvesters using Timoshenko and Euler-Bernoulli beam theory,” *Journal of Intelligent Material Systems and Structures*, vol. 24, no. 2, pp. 226–239, Sep. 2012.

[67] F. Lu, H. P. Lee, and S. P. Lim, “Modeling and analysis of micro piezoelectric power generators for micro-electromechanical-systems applications,” *Smart Materials and Structures*, vol. 13, no. 1, 2004.

[68] J. H. Lin, X. M. Wu, T. L. Ren, and L. T. Liu, “Modeling and simulation of piezoelectric MEMS energy harvesting device,” *Integrated Ferroelectrics*, vol. 95, no. 1, pp. 128–141, Dec. 2007.

[69] H. Wang and Q. Meng, “Analytical modeling and experimental verification of vibration-based piezoelectric bimorph beam with a tip-mass for power harvesting,” *Mechanical Systems and Signal Processing*, vol. 36, no. 1, pp. 193–209, Mar. 2013.

[70] S.-N. Chen, G.-J. Wang, and M.-C. Chien, “Analytical modeling of piezoelectric vibration-induced micro power generator,” *Mechatronics*, vol. 16, no. 7, pp. 379–387, Sep. 2006.

[71] N. W. Hagood, W. H. Chung, and A. Von Flotow, “Modelling of piezoelectric actuator dynamics for active structural control,” *Journal of Intelligent Material Systems and Structures*, vol. 1, no. 3, pp. 327–354, Jul. 1990.

[72] H. A. Sodano, G. Park, and D. J. Inman, “Estimation of electric charge output for piezoelectric energy harvesting,” *Strain*, vol. 40, no. 2, pp. 49–58, May 2004.

[73] A. Erturk and D. J. Inman, “Issues in mathematical modeling of piezoelectric energy harvesters,” *Smart Materials and Structures*, vol. 17, no. 6, 2008.

[74] J. Ajitsaria, S. Y. Choe, D. Shen, and D. J. Kim, "Modeling and analysis of a bimorph piezoelectric cantilever beam for voltage generation," *Smart Materials and Structures*, vol. 16, no. 2, 2007.

[75] P. J. Cornwell, "Enhancing power harvesting using a tuned auxiliary structure," *Journal of Intelligent Material Systems and Structures*, vol. 16, no. 10, pp. 825–834, Oct. 2005.

[76] A. Erturk and D. J. Inman, "A distributed parameter electromechanical model for cantilevered piezoelectric energy harvesters," *Journal of Vibration and Acoustics*, vol. 130, no. 4, p. 041002, Aug. 2008.

[77] A. Erturk and D. J. Inman, "An experimentally validated bimorph cantilever model for piezoelectric energy harvesting from base excitations," *Smart Materials and Structures*, vol. 18, no. 2, 2009.

[78] W. C. Young, *Roark's formulas for stress and strain*. New York: McGraw-Hill Professional, 1989.

[79] J. Reddy, *An introduction to the finite element method*. McGraw-Hill Science/Engineering/Math, 2005.

[80] F. Shi, P. Ramesh, and S. Mukherjee, "Simulation methods for micro-electro-mechanical structures (MEMS) with application to a microtweezer," *Computers & Structures*, vol. 56, no. 5, pp. 769–783, Sep. 1995.

[81] E. Carrera, "Theories and finite elements for multilayered, anisotropic, composite plates and shells," *Archives of Computational Methods in Engineering*, vol. 9, no. 2, pp. 87–140, Jun. 2002.

[82] B. Bhushan and G. B. Agrawal, "Stress analysis of nanostructures using a finite element method," *Nanotechnology*, vol. 13, no. 4, 2002.

[83] R. Krondorfer, Y. K. Kim, J. Kim, C.-G. Gustafson, and T. C. Lommasson, "Finite element simulation of package stress in transfer molded MEMS pressure sensors," *Microelectronics Reliability*, vol. 44, no. 12, pp. 1995–2002, Dec. 2004.

[84] Q.-M. Wang, Z. Yang, F. Li, and P. Smolinski, "Analysis of thin film piezoelectric microaccelerometer using analytical and finite element modeling," *Sensors and Actuators A: Physical*, vol. 113, no. 1, pp. 1–11, Jun. 2004.

[85] K. I. Tserpes and P. Papanikos, "Finite element modeling of single-walled carbon nanotubes," *Composites Part B: Engineering*, vol. 36, no. 5, pp. 468–477, Jul. 2005.

[86] G. Wei, Y. Shouwen, and H. Ganyun, "Finite element characterization of the size-dependent mechanical behaviour in nanosystems," *Nanotechnology*, vol. 17, no. 4, 2006.

[87] A. Duwel, R. N. Candler, T. W. Kenny, and M. Varghese, "Engineering MEMS resonators with low thermoelastic damping," *Journal of Microelectromechanical Systems*, vol. 15, no. 6, pp. 1437–1445, Dec. 2006.

[88] N. Stojanovic, E. B. K. Washington, J. M. Berg, M. W. Holtz, and H. Temkin, "Thin-film thermal conductivity measurement using microelectrothermal test structures and finitee-element-nodel-based data analysis," *Journal of Microelectromechanical Systems*, vol. 16, no. 5, pp. 1269–1275, Oct. 2007.

[89] M. A. Hopcroft, W. D. Nix, and T. W. Kenny, "What is the Young's Modulus of silicon?," *Journal of Microelectromechanical Systems*, vol. 19, no. 2, pp. 229–238, Apr. 2010.

[90] R. Anzalone, G. D'Arrigo, M. Camarda, C. Locke, S. E. Saddow, and F. La Via, "Advanced Residual Stress Analysis and FEM Simulation on Heteroepitaxial 3C–SiC for MEMS Application," *Journal of Microelectromechanical Systems*, vol. 20, no. 3, pp. 745–752, Jun. 2011.

[91] P. C. Miranda, M. Hallett, and P. J. Basser, "The electric field induced in the brain by magnetic stimulation: a 3-d finite-element analysis of the effect of tissue heterogeneity and

anisotropy," *IEEE Transactions on Biomedical Engineering*, vol. 50, no. 9, pp. 1074–1085, Sep. 2003.

[92] C. R. Sovinec, A. H. Glasser, T. A. Gianakon, D. C. Barnes, R. A. Nebel, S. E. Kruger, D. D. Schnack, S. J. Plimpton, A. Tarditi, and M. S. Chu, "Nonlinear magnetohydrodynamics simulation using high-order finite elements," *Journal of Computational Physics*, vol. 195, no. 1, pp. 355–386, Mar. 2004.

[93] J. L. Pérez-Aparicio and H. Sosa, "A continuum three-dimensional, fully coupled, dynamic, non-linear finite element formulation for magnetostrictive materials," *Smart Materials and Structures*, vol. 13, no. 3, 2004.

[94] A. Benjeddou, "Advances in piezoelectric finite element modeling of adaptive structural elements: a survey," *Computers & Structures*, vol. 76, no. 1–3, pp. 347–363, Jun. 2000.

[95] S. Narayanan and V. Balamurugan, "Finite element modelling of piezolaminated smart structures for active vibration control with distributed sensors and actuators," *Journal of Sound and Vibration*, vol. 262, no. 3, pp. 529–562, May 2003.

[96] Z. K. Kusculuoglu and T. J. Royston, "Nonlinear modeling of composite plates with piezoceramic layers using finite element analysis," *Journal of Sound and Vibration*, vol. 315, no. 4–5, pp. 911–926, Sep. 2008.

[97] E. E. Aktakka, R. L. Peterson, and K. Najafi, "Thinned-PZT on SOI process and design optimization for piezoelectric inertial energy harvesting," in *Proceedings Intl. Conf. Solid-State Sens. Actuators Microsystems (Transducers)*, 2011, pp. 1649–1652.

[98] S. A. Gelfand, *Hearing: an introduction to psychological and physiological acoustics*. CRC Press, 2009, p. 312.

[99] B. Jaffe, W. R. Cook, and H. L. Jaffe, *Piezoelectric ceramics*. London, UK: Academic Press, 1971.

[100] ANSYS, "ANSYS Elements Reference," Canonsburg, PA, 2005.

[101] C. Liu, *Foundations of MEMS*. Prentice Hall, 2005.

[102] S. D. Senturia, *Microsystem design*. Springer, 2000.

[103] M. J. Madou, *Fundamentals of microfabrication and nanotechnology*. CRC Press, 2011.

[104] H. J. McSkimin and P. Andreatch, "Elastic moduli of silicon vs hydrostatic pressure at 25.0°C and − 195.8°C," *Journal of Applied Physics*, vol. 35, no. 7, p. 2161, 1964.

[105] J. J. Wortman and R. A. Evans, "Young's Modulus, Shear Modulus, and Poisson's Ratio in Silicon and Germanium," *Journal of Applied Physics*, vol. 36, no. 1, p. 153, Jan. 1965.

[106] J. Hall, "Electronic effects in the elastic constants of n-type silicon," *Journal of Applied Physics*, vol. 161, no. 3, pp. 756–761, Sep. 1967.

[107] W. A. Brantley, "Calculated elastic constants for stress problems associated with semiconductor devices," *Journal of Applied Physics*, vol. 44, no. 1, p. 534, Jan. 1973.

[108] A. C. Ugural and S. K. Fenster, *Advanced strength and applied elasticity*. Elsevier Science Ltd, 1975, p. 448.

[109] J. F. Nye, *Physical properties of crystals: their representation by tensor and matrices*. United Kingdom: Oxford University Press, 1957.

[110] E. Heinonen, J. Juuti, and S. Leppävuori, "Characterization and modelling of 3D piezoelectric ceramic structures with ATILA software," *Journal of the European Ceramic Society*, vol. 25, no. 12, pp. 2467–2470, Jan. 2005.

[111] P. S. Inc, "PSI-5A4E Piezoceramic Sheets and Plates." [Online]. Available: http://www.piezo.com/prodsheet1sq5A.html. [Accessed: 16-Apr-2013].

[112] Efunda, "Properties of Piezo Material Lead Zirconate Titanate (PZT-5A)." [Online]. Available:

http://www.efunda.com/materials/piezo/material_data/matdata_output.cfm?Material_ID=PZT-5A. [Accessed: 29-Apr-2013].

[113] L. Beker, A. Muhtaroglu, H. N. Ozguven, and H. Kulah, "Finite element modeling of MEMS piezoelectric energy harvester," in *Proceedings NSTI Nanotech Modeling Simulation of Microsystems (MSM)*, 2012, pp. 633–636.

[114] L. Beker, H. Kulah, and A. Muhtaroglu, "Piezoelectric cantilever prototype for energy harvesting in computing applications," in *IEEE Intl. Conf. Energy Aware Computing (ICEAC)*, 2011.

[115] L. Beker, O. Zorlu, H. Kulah, and A. Muhtaroglu, "Hybrid energy harvesting from keyboard," in *IEEE Intl. Conf. Energy Aware Computing (ICEAC)*, 2011.

[116] L. Beker, A. Muhtaroglu, and H. Külah, "A novel method for piezoelectric energy harvesting from keyboard," in *Proceedings SPIE Smart Structures and Materials NDE*, 2012.

[117] H. Hosaka, K. Itao, and S. Kuroda, "Damping characteristics of beam-shaped micro-oscillators," *Sensors and Actuators A: Physical*, vol. 49, no. 1–2, pp. 87–95, Jun. 1995.

[118] M. T. Kozak, "Investigation of Model Updating Technigues and their Applications to Aircraft Structures," M.Sc. Thesis, Middle East Technical University, 2006.

[119] "Auditory system - Wikipedia, the free encyclopedia." [Online]. Available: http://en.wikipedia.org/wiki/Auditory_system. [Accessed: 01-May-2013].

[120] H. L. F. Helmholtz, "The mechanism of the middle-ear ossicles and of the eardrum," *Pflugers Arch. Gesamte Physiol. Menschentiere (Bonn)*, vol. 1, no. 1, 1873.

[121] G. Von Bèkesy, "On the measurement of the amplitude of vibration of the ossicles with a capacitive probe," *Akustishe Zeitschrift*, 1941.

[122] J. Tonndorf and S. M. Khanna, "Tympanic membrane vibrations in human cadaver ears studied by time-averaged holography," *The Journal of the Acoustical Society of America*, vol. 52, no. 4B, p. 1221, Oct. 1972.

[123] T. H. J. Lesser and K. R. Williams, "The tympanic membrane in cross section: a finite element analysis," *The Journal of Laryngology and Otology*, vol. 102, pp. 209–214, 1988.

[124] H. Wada, T. Metoki, and T. Kobayashi, "Analysis of dynamic behavior of human middle ear using a finite-element method," *The Journal of the Acoustical Society of America*, vol. 92, no. 6, p. 3157, Dec. 1992.

[125] W. R. J. Funnell, "Low-frequency coupling between eardrum and manubrium in a finite-element model," *The Journal of the Acoustical Society of America*, vol. 99, no. 5, p. 3036, May 1996.

[126] P. Ferris and P. J. Prendergast, "Middle-ear dynamics before and after ossicular replacement," *Journal of Biomechanics*, vol. 33, no. 5, pp. 581–590, May 2000.

[127] Q. Sun, R. Z. Gan, K.-H. Chang, and K. J. Dormer, "Computer-integrated finite element modeling of human middle ear," *Biomechanics and Modeling in Mechanobiology*, vol. 1, no. 2, pp. 109–22, Oct. 2002.

[128] T. Koike, H. Wada, and T. Kobayashi, "Modeling of the human middle ear using the finite-element method," *The Journal of the Acoustical Society of America*, vol. 111, no. 3, p. 1306, Mar. 2002.

[129] R. Z. Gan, B. Feng, and Q. Sun, "Three-Dimensional finite element modeling of human ear for sound transmission," *Annals of Biomedical Engineering*, vol. 32, no. 6, pp. 847–859, Jun. 2004.

[130] A. Eiber, "Mechanical modeling and dynamical behavior of the human middle ear," *Audiology & Neuro-otology*, vol. 4, no. 3–4, pp. 170–7, 1999.

[131] N. Elkhouri, H. Liu, and W. R. J. Funnell, "Low-frequency finite-element modeling of the gerbil middle ear," *Journal of the Association for Research in Otolaryngology*, vol. 7, no. 4, pp. 399–411, Dec. 2006.

[132] R. Z. Gan, Q. Sun, B. Feng, and M. W. Wood, “Acoustic-structural coupled finite element analysis for sound transmission in human ear--pressure distributions,” *Medical Engineering & Physics*, vol. 28, no. 5, pp. 395–404, Jun. 2006.

[133] A. Eiber, C. Breuninger, J. Jorge, H. Zenner, and M. Maasen, “On the optimal coupling of an implantable hearing aid – measurements and simulations,” in *Proceedings Int. Symposium Middle Ear Mechanics in Research and Otology*, A. Eiber and A. Huber, Eds. Singapore: World Scientific Publishing Co. Pte. Ltd., 2006, pp. 246–252.

[134] G. Schimanski, U. Steinhardt, and A. Eiber, “Development of a new clip-piston prosthesis for the stapes,” in *Proceedings Int. Symposium Middle Ear Mechanics in Research and Otology*, A. Eiber and A. Huber, Eds. Singapore: World Scientific Publishing Co. Pte. Ltd., 2006, pp. 237–245.

[135] O. L. Roufaeil and D. J. Dawe, “Rayleigh-ritz vibration analysis of rectangular mindlin plates subjected to membrane stresses,” *Journal of Sound and Vibration*, vol. 85, no. 2, pp. 263–275, Nov. 1982.

[136] C. W. Wu and W.-H. Chen, “Extension of spline wavelets element method to membrane vibration analysis,” *Computational Mechanics*, vol. 18, no. 1, pp. 46–54, May 1996.

[137] W. B. Krantz, R. R. Bilodeau, M. E. Voorhees, and R. J. Elgas, “Use of axial membrane vibrations to enhance mass transfer in a hollow tube oxygenator,” *Journal of Membrane Science*, vol. 124, no. 2, pp. 283–299, Feb. 1997.

[138] C. Zhu, “Modeling of ultrasonic enhancement on membrane distillation,” *Journal of Membrane Science*, vol. 176, no. 1, pp. 31–41, Aug. 2000.

[139] L. S. Pan, T. Y. Ng, G. R. Liu, K. Y. Lam, and T. Y. Jiang, “Analytical solutions for the dynamic analysis of a valveless micropump — a fluid–membrane coupling study,” *Sensors and Actuators A: Physical*, vol. 93, no. 2, pp. 173–181, Sep. 2001.

[140] G. R. Buchanan and J. Peddieson, “A finite element in elliptic coordinates with application to membrane vibration,” *Thin-Walled Structures*, vol. 43, no. 9, pp. 1444–1454, Sep. 2005.

[141] Y. S. Choya, J. Huang, L. Huang, and Y. Zhou, “An experimental study of flow induced vibration on a tensioned membrane,” *Journal of Mechanical Science and Technology*, vol. 21, no. 9, pp. 1359–1366, Sep. 2007.

[142] L. Beker, H. N. Ozguven, and H. Kulah, “Optimization of an energy harvester coupled to a vibrating membrane,” in *Proceedings Intl. Modal Analysis Conference and Exposition on Structural Dynamics (IMAC)*, 2013.

[143] J. Aernouts, J. A. M. Soons, and J. J. J. Dirckx, “Quantification of tympanic membrane elasticity parameters from in situ point indentation measurements: validation and preliminary study,” *Hearing Research*, vol. 263, no. 1–2, pp. 177–82, May 2010.

[144] J. A. Donaldson and J. M. Miller, *Anatomy of the ear*. Philadelphia: Saunders, 1973.

[145] M. Sundberg, “Optical methods for typanic membrane characterisation,” Ph.D. Thesis, Linköping University, 2008.

[146] C. D. Bluestone, “Physiology of the middle ear and eustachian tube,” in *Otolaryngology*, M. M. Paparella and D. A. Shumrick, Eds. Philadelphia: WB Saunders, 1991.

[147] I. Kirikae, *The structure and function of the middle ear*. Tokyo: University of Tokyo Press, 1960.

[148] J. J. J. Dirckx and W. F. Decraemer, “Interferometer for eardrum shape measurement, based on projection of straight line rulings,” *Lasers in Medical Science*, vol. 15, no. 2, pp. 131–139, Mar. 2000.

[149] “Pathophysiology of chronic otitis media.” [Online]. Available: http://nandanursingdiagnoses.blogspot.com/2012/07/pathophysiology-of-chronic-otitis-media.html. [Accessed: 05-May-2013].

[150] K. H. Hüttenbrink, "Biomechanical aspects of the middle ear reconstruction," in *Middle Ear Surgery, Recent Advances and Future Directions*, K. Jahnke, Ed. Stuttgart, Germany: Georg Thieme Verlag, 2003, pp. 23–51.

[151] W. F. Decraemer and W. R. J. Funnell, "Anatomical and mechanical properties of the tympanic membrane," in *Chronic Otitis Media. Pathogenesis-Oriented Therapeutic Management*, Amsterdam, Netherlands: Kugler Publications, 2008, pp. 51–84.

[152] J. A. N. Buytaert, J. E. F. Aernouts, and J. J. J. Dirckx, "Indentation measurements on the eardrum with automated projection moiré profilometry," *Optics and Lasers in Engineering*, vol. 47, no. 3–4, pp. 301–309, Mar. 2009.

[153] D. J. Lim, "Tympanic membrane: electron microscopic observation part I: pars tensa," *Acta Otolaryngologica*, vol. 66, no. 1, pp. 181–198, Jul. 1968.

[154] D. J. Lim, "Tympanic membrane part II.: pars flaccida," *Acta Otolaryngologica*, vol. 66, no. 1, pp. 515–532, Jul. 1968.

[155] J. Fay, S. Puria, W. F. Decraemer, and C. Steele, "Three approaches for estimating the elastic modulus of the tympanic membrane," *Journal of Biomechanics*, vol. 38, no. 9, pp. 1807–15, Sep. 2005.

[156] N. P. Daphalapurkar, C. Dai, R. Z. Gan, and H. Lu, "Characterization of the linearly viscoelastic behavior of human tympanic membrane by nanoindentation," *Journal of the Mechanical Behavior of Biomedical Materials*, vol. 2, no. 1, pp. 82–92, Jan. 2009.

[157] H. J. Beer, M. Bornitz, J. Drescher, R. Schmidt, and H. J. Hardtke, "Finite element modeling of the human eardrum and applications," in *Middle Ear Mechanics in Research and Otosurgery*, K. H. Hüttenbrink, Ed. Dresden, Germany: Department of Oto-Rhino-Laryngology, Dresden University of Technology, 1996, pp. 40–47.

[158] P. J. Prendergast, P. Ferris, H. J. Rice, and A. W. Blayney, "Vibro-acoustic modelling of the outer and middle ear using the finite-element method," *Audiology & Neuro-otology*, vol. 4, no. 3–4, pp. 185–91, 1999.

[159] W. R. Funnell and C. A. Laszlo, "A critical review of experimental observations on ear-drum structure and function," *Journal for Oto-Rhino-Laryngology and Its Related Specialties*, vol. 44, no. 4, pp. 181–205, Jan. 1982.

[160] H. Wada and T. Kobayashi, "Dynamical behavior of middle ear: theoretical study corresponding to measurement results obtained by a newly developed measuring apparatus," *Journal of the Acoustical Society of America*, vol. 87, no. 1, p. 237, Jan. 1990.

[161] T. Koike, H. Wada, T. Kobayashi, and T. Takasaka, "Finite-element method (FEM) analysis of human middle-ear," in *Proceedings of the ARO Meeting*, 1996, p. 778.

[162] Q. Sun, "Computer-integrated finite element modeling and simulation of human middle ear," Ph.D. Thesis, University of Oklahoma, Norman, 2001.

[163] G. Herrmann and H. Liebowitz, "Mechanics of bone fractures," in *Fracture: An Advanced Treatise*, H. Liebowitz, Ed. New York: Academic Press, 1972, pp. 772–840.

[164] A. D. Speirs, M. A. Hotz, T. R. Oxland, R. Häusler, and L. P. Nolte, "Biomechanical properties of sterilized human auditory ossicles," *Journal of Biomechanics*, vol. 32, no. 5, pp. 485–91, May 1999.

[165] K. R. Williams, A. W. Blayney, and H. J. Rice, "Development of a finite element model of the middle ear," *Revue de Laryngologie - Otologie - Rhinologie*, vol. 117, no. 3, pp. 259–64, Jan. 1996.

[166] A. M. Huber, C. Schwab, T. Linder, S. J. Stoeckli, M. Ferrazzini, N. Dillier, and U. Fisch, "Evaluation of eardrum laser doppler interferometry as a diagnostic tool," *The Laryngoscope*, vol. 111, no. 3, pp. 501–7, Mar. 2001.

[167] T. J. F. Buunen, "Laser–Doppler velocity meter applied to tympanic membrane vibrations in cat," *The Journal of the Acoustical Society of America*, vol. 69, no. 3, p. 744, Mar. 1981.

[168] K. R. Whittemore, S. N. Merchant, B. B. Poon, and J. J. Rosowski, "A normative study of tympanic membrane motion in humans using a laser Doppler vibrometer (LDV)," *Hearing Research*, vol. 187, no. 1–2, pp. 85–104, Jan. 2004.

[169] R. L. Goode, M. Killion, K. Nakamura, and S. Nishihara, "New knowledge about the function of the human middle ear: development of an improved analog model," *The American Journal of Otology*, vol. 15, no. 2, pp. 145–54, Mar. 1994.

[170] J. T. Cheng, A. A. Aarnisalo, E. Harrington, M. D. S. Hernandez-Montes, C. Furlong, S. N. Merchant, and J. J. Rosowski, "Motion of the surface of the human tympanic membrane measured with stroboscopic holography," *Hearing Research*, vol. 263, no. 1–2, pp. 66–77, May 2010.

[171] S. M. Khanna, "Tympanic membrane vibrations in cats studied by time-averaged holography," *The Journal of the Acoustical Society of America*, vol. 51, no. 6B, p. 1904, Jun. 1972.

[172] H. Aritomo, "Ossicular vibration in human temporal bones," *Nihon Jibiinkoka Gakkai Kaiho*, vol. 92, no. 9, pp. 1359–70, Sep. 1989.

[173] K. Gyo, H. Aritomo, and R. L. Goode, "Measurement of the ossicular vibration ratio in human temporal bones by use of a video measuring system," *Acta Otolaryngologica*, vol. 103, no. 1, pp. 87–95, Jul. 1987.

[174] K. Dems, "First- and second-order shape sensitivity analysis of structures," *Structural Optimization*, vol. 3, no. 2, pp. 79–88, Jun. 1991.

[175] ANSYS, "Mechanical APDL and Mechanical Applications Theory Reference," Canonsburg, PA, 2010.

[176] E. E. Aktakka, R. L. Peterson, and K. Najafi, "A CMOS-compatible piezoelectric vibration energy scavenger based on the integration of bulk PZT films on silicon," in *IEEE Intl. Electron Devices Meeting (IEDM)*, 2010, pp. 31.5.1–31.5.4.

[177] A. A. Frederick, "Analysis and fabrication of MEMS tunable piezoelectric resonators," M.Sc. Thesis, University of Pittsburgh, 2006.

[178] R. McKee, F. Walker, and M. Chisholm, "Crystalline oxides on silicon: the first five monolayers," *Physical Review Letters*, vol. 81, no. 14, pp. 3014–3017, Oct. 1998.

[179] D. Isarakorn, A. Sambri, P. Janphuang, D. Briand, S. Gariglio, J. M. Triscone, F. Guy, J. W. Reiner, C. H. Ahn, and N. F. de Rooij, "Epitaxial piezoelectric MEMS on silicon," *Journal of Micromechanics and Microengineering*, vol. 20, no. 5, 2010.

[180] K. Morimoto, I. Kanno, K. Wasa, and H. Kotera, "High-efficiency piezoelectric energy harvesters of c-axis-oriented epitaxial PZT films transferred onto stainless steel cantilevers," *Sensors and Actuators A: Physical*, vol. 163, no. 1, pp. 428–432, Sep. 2010.

[181] M. Stamos, N. Nicoleau, R. Torah, J. Tudor, N. R. Harris, A. Niewiadomski, and S. P. Beeby, "Screen printed piezoelectric generator for helicopter health and usage monitoring systems," in *Proceedings Intl. Conf. Micro and Nanotechnology for Power Generation and Energy Conversion (PowerMEMS)*, 2008.

[182] Y. Jeon, J. Chung, and K. No, "Fabrication of PZT thick films on silicon substrates for piezoelectric actuator," *Journal of Electroceramics*, vol. 4, no. 1, pp. 195–199, Mar. 2000.

[183] C. G. Hindrichsen, R. Lou-Møller, K. Hansen, and E. V. Thomsen, "Advantages of PZT thick film for MEMS sensors," *Sensors and Actuators A: Physical*, vol. 163, no. 1, pp. 9–14, Sep. 2010.

[184] R. Dorey, R. Whatmore, S. Beeby, R. Torah, and N. White, "Screen-printed PZT composite thick films," *Integrated Ferroelectrics*. Taylor & Francis, 2004.

[185] R. Lou-Moeller, C. C. Hindrichsen, L. H. Thamdrup, T. Bove, E. Ringgaard, A. F. Pedersen, and E. V. Thomsen, "Screen-printed piezoceramic thick films for miniaturised devices," *Journal of Electroceramics*, vol. 19, no. 4, pp. 333–338, Mar. 2007.

[186] LTCC, "Prototyping via filling." [Online]. Available: http://www.ltcc.de/en/prototyping_vfi.php. [Accessed: 10-May-2013].

[187] S. Fusihimi and T. Ikeda, "Phase Equilibrium in the System PbO-TiO2-ZrO2," *Journal of the American Ceramic Society*, vol. 50, no. 3, pp. 129–132, Mar. 1967.

[188] Y. Shichi, S. Tanimoto, T. Goto, K. Kuroiwa, and Y. Tarui, "Interaction of PbTiO3 films with Si substrate," *Japanese Journal of Applied Physics*, vol. 33, no. Part 1, No. 9B, pp. 5172–5177, Sep. 1994.

[189] P. Janphuang, D. Isarakorn, D. Briand, and N. F. de Rooij, "Energy harvesting from a rotating gear using an impact type piezoelectric MEMS scavenger," in *Proceedings Intl. Conf. Solid-State Sens. Actuators Microsystems (Transducers)*, 2011, pp. 735–738.

[190] J. Ruan, V. Quintero, A. Felipe, P. Janphuang, D. Isarakorn, D. Briand, and N. F. de Rooij, "PZT thick sheet on flexible plastic substrate for vibration energy harvesting," in *Proceedings Intl. Conf. Micro and Nanotechnology for Power Generation and Energy Conversion (PowerMEMS)*, 2011, pp. 151–154.

[191] L. Beker, O. Zorlu, and H. Kulah, "A room temperature, zero force, wafer-level attachment method for MEMS integration," in *Proceedings IEEE Intl. Conf. Micro Electro Mechanical Systems (MEMS)*, 2013, pp. 267–270.

[192] L. Beker, O. Zorlu, and H. Kulah, "A parylene coating based room temperature wafer-level attachment method for MEMS integration with zero applied force," Accepted to *Sensors and Actuators A: Physical*, 2013.

[193] Smart Equipment Technologies (SET) Corp., "FC 150 Data Sheet," 2009.

[194] H. Takagi, R. Maeda, and T. Suga, "Room-temperature wafer bonding of Si to LiNbO3, LiTaO3 and Gd3Ga5O12 by Ar-beam surface activation," *Journal of Micromechanics and Microengineering*, vol. 11, no. 4, 2001.

[195] G. Tang, J. Liu, H. Liu, Y. Li, C. Yang, D. He, V. DzungDao, K. Tanaka, and S. Sugiyama, "Piezoelectric MEMS generator based on the bulk PZT/silicon wafer bonding technique," *Physica Status Solidi A*, vol. 208, no. 12, pp. 2913–2919, Dec. 2011.

[196] K. T. Turner, R. Mlcak, D. C. Roberts, and S. M. Spearing, "Bonding of Bulk Piezoelectric Material to Silicon Using a Gold-Tin Eutectic Bond," *Proceedings of Materials Research Society (MRS)*, vol. 687, p. B3.2, Mar. 2001.

[197] Z. Wang, J. Miao, C. W. Tan, and T. Xu, "Fabrication of piezoelectric MEMS devices-from thin film to bulk PZT wafer," *Journal of Electroceramics*, vol. 24, no. 1, pp. 25–32, Mar. 2008.

[198] C. H. Tsau, S. M. Spearing, and M. A. Schmidt, "Fabrication of wafer-level thermocompression bonds," *Journal of Microelectromechanical Systems*, vol. 11, no. 6, pp. 641–647, 2002.

[199] M. M. V Taklo, P. Storas, K. Schjolberg-Henriksen, H. K. Hasting, and H. Jakobsen, "Strong, high-yield and low-temperature thermocompression silicon wafer-level bonding with gold," *Journal of Micromechanics and Microengineering*, vol. 14, no. 7, 2004.

[200] S. X. Jia, J. Wu, J. Zhu, and Y. X. Wang, "Study on the gold-gold thermocompression bonding for wafer-level packaging," *Advanced Materials Research*, vol. 60–61, pp. 325–329, Mar. 2009.

[201] J. Jellison, "Effect of surface contamination on the thermocompression bondability of gold," *IEEE Transactions on Parts, Hybrids, and Packaging*, vol. 11, no. 3, pp. 206–211, 1975.

[202] K. Stamoulis, C. H. Tsau, and S. M. Spearing, "Low-temperature wafer-level gold thermocompression bonding: modeling of flatness deviations and associated process optimization for high yield and tough bonds," in *SPIE MOEMS-MEMS Micro & Nanofabrication*, 2005, pp. 42–52.

[203] B. K. Kurman and S. G. Mita, “Gold-Gold (Au-Au) thermocompression (TC) bonding of very large arrays,” in *Proceedings Intl. Conf. Electronic Components and Technology*, 1992, pp. 883–889.

[204] C. H. Tsau, M. A. Schmidt, and S. M. Spearing, “Fabrication process and plasticity of gold-gold thermocompression bonds,” in *Proceedings Intl. Symposium Semiconductor Wafer Bonding*, 2001.

[205] C. H. Tsau, M. A. Schmidt, and S. M. Spearing, “Characterization of low temperature, wafer-level gold-gold thermocompression bonds,” *Proceedings of Materials Research Society (MRS)*, vol. 605, p. 171, Feb. 2000.

[206] A. Drost, “Simultaneous fabrication of dielectric and electrical joints by wafer bonding,” in *Proceedings Intl. Conf. Micromachined Devices and Components*, 1998, pp. 62 – 71.

[207] W. C. Welch, “Vacuum and hermetic packaging of MEMS using solder,” Ph.D. Thesis, University of Michigan, 2008.

[208] Disco, “Automatic surface grinder DAG810,” [Online]. Available: http://www.disco.co.jp/eg/products/catalog/pdf/dag810.pdf/ . [Accessed: 28-Jul-2013].

[209] P. Sun, Q. Zhou, B. Zhu, D. Wu, C. Hu, J. M. Cannata, J. Tian, P. Han, G. Wang, and K. K. Shung, “Design and fabrication of PIN-PMN-PT single-crystal high-frequency ultrasound transducers,” *IEEE Transactions on Ultrasonics, Ferroelectrics, and Frequency Control*, vol. 56, no. 12, pp. 2760–3, Dec. 2009.

[210] F. Goldschmidtboeing, C. Eichhorn, M. Wischke, M. Kroener, and P. Woias, “The influence of ferroelastic hysteresis on mechanically excited PZT cantilever beams,” in *Int. Workshop on Micro and Nanotechnology for Power Generation and Energy Conversion Application (PowerMEMS 2011)*, 2011, no. 1, pp. 114–117.

[211] Medel Corp., “Vibrant Soundbridge Features.” [Online]. Available: http://www.medel.com/data/pdf/. [Accessed: 28-Jul-2013].

[212] P. Janphuang, R. Lockhart, D. Briand, and N. F. de Rooij, “Wafer level fabrication of vibrational energy harvesters using bulk PZT sheets,” *Procedia Engineering*, vol. 47, pp. 1041–1044, Jan. 2012.

[213] D. Shen, J.-H. Park, J. Ajitsaria, S.-Y. Choe, H. Wikle III, and D.-J. Kim, “The design, fabrication and evaluation of a MEMS PZT cantilever with an integrated Si proof mass for vibration energy harvesting,” *Journal of Micromechanics and Microengineering*, vol. 18, no. 5, pp. 1–7, 2008.

[214] “Teddy’s Rat Lab: ‘And Ears to Hear’ [Online]. Available: http://teddysratlab.blogspot.com/2011/03/and-ears-to-hear.html. [Accessed: 23-Jul-2013].

[215] I. H. Publications and H. P. I. H. Publications, *Hearing Loss - A Medical Dictionary, Bibliography, and Annotated Research Guide to Internet References*. ICON Health Publications, 2004, p. 436.

[216] H. Lane, R. Hoffmeister, and B. Bahan, *A journey into the deaf-world*. DawnSignPress, 1996, p. 560.

[217] Medel Corp., “How hearing works.” [Online]. Available: http://www.medel.com/how-hearing-works/.

[218] C. Luo, G. Z. Cao, and I. Y. Shen, “Development of a lead-zirconate-titanate (PZT) thin-film microactuator probe for intracochlear applications,” *Sensors and Actuators A: Physical*, vol. 201, pp. 1–9, Oct. 2013.

[219] J. Lau, C. Lee, C. Premachandran, and Y. Aibin, *Advanced MEMS packaging*. McGraw-Hill Professional, 2009, p. 576.

APPENDIX A

ROOM TEMPERATURE AND ZERO FORCE TEMPORARY ATTACHMENT METHOD VIA PARYLENE COATING

Recently, wafer handling techniques have received great attention for 3-D packaging, TSV formation, and integration of special materials into MEMS. These techniques require moderate to high force levels, thermal treatments, or special equipment [219], which may degrade the superior properties of delicate materials such as magnetic films and piezoelectric plaques. In this work, a new attachment method for such materials is reported.

A wafer-level attachment method using parylene as an interlayer material for integrating various shaped and fragile substrates into MEMS processes is presented in this study. The proposed method utilizes a handle wafer containing pillars and perforations. The structures to be attached are placed on the pillars (Figure A.1a), and they are attached to the substrate through a standard parylene coating process realized at room temperature with no applied force. Here, parylene conformally fills the gaps between the structures and the handle wafer by penetrating through the perforations (Figure A.1b).

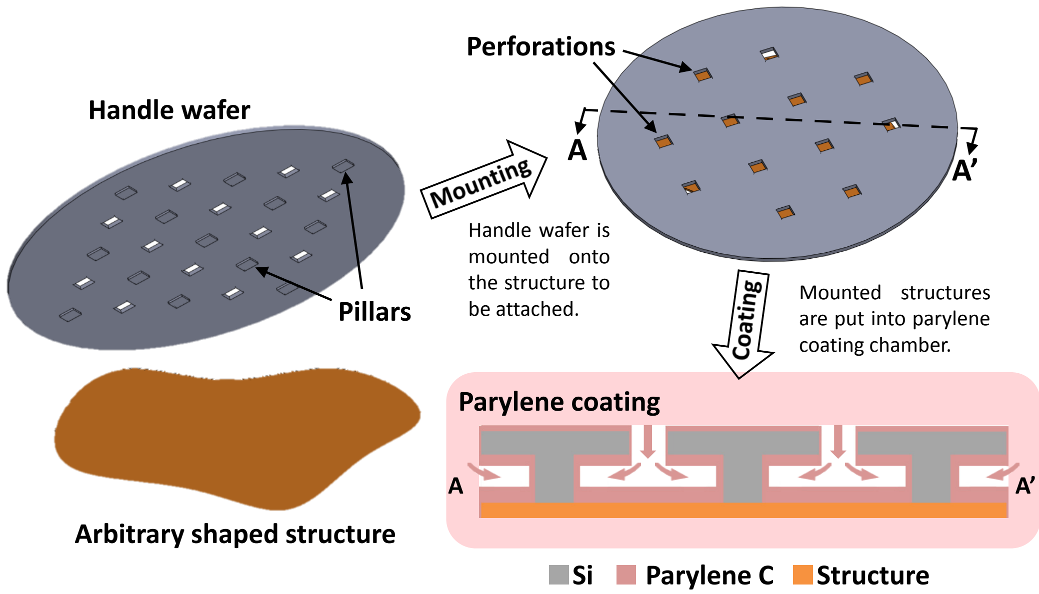

Figure A.1: a) Handling of thin structures using parylene coating, b) cross section of A-A’.

As a first step, a handle wafer containing only a pillar pattern is studied to observe the parylene penetration and interlayer formation between two substrates. The gap between the substrates, resulting from the pillar height, is filled via parylene coating, and the substrates are attached to each other.

Figure A.2 shows the cross section around a 125 µm pillar. Although the region in Figure A.2b, which is closer to the wafer edge, is completely filled with parylene, the region in Figure A.2c has a void, since parylene stacking occurs and pillar structures prevent further penetration to inner regions.

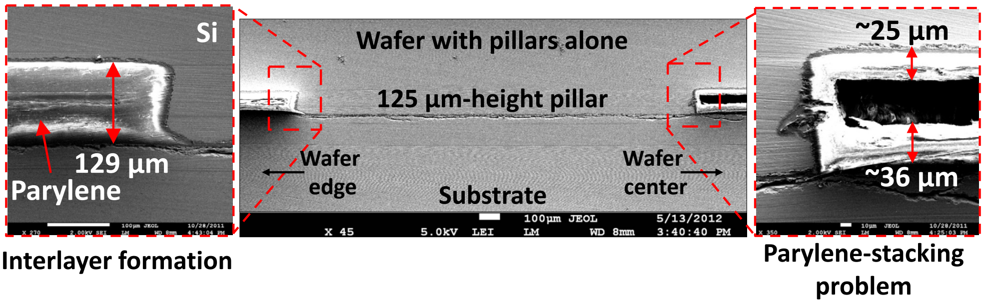

Figure A.2: Cross sectional SEM image around a) fully filled side, b) pillar, c) partially filled side.

Secondly, a study is conducted to find the optimum pillar pattern yielding the maximum parylene penetration. A handle wafer containing several pillar patterns (Figure A.3a) has been fabricated with a pillar height of 20 µm (Figure A.3b), and it is observed that Pattern 2 (size, S: 2.5 mm; distance, D: 9.5 mm) yields the highest mean penetration length of 1.8 cm from the wafer edge. However, this penetration length is too small for completely attaching two large substrates (e.g. 4" wafers). Increasing the pillar height up to 100 µm naturally improves the penetration length (Figure A.3c) enabling the attachment of 3"-sized substrates, but this results in excessive parylene consumption and process time.

(a)

Pattern No	1	2	3	4
Size (S) [mm]	5	2.5	1.3	0.63
Distance (D) [mm]	12	9.5	5.5	3.6

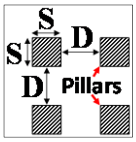

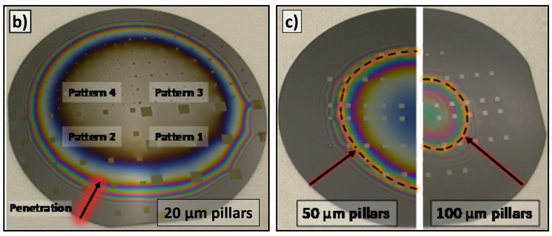

Figure A.3: a) Pillar patterns b) wafer with various patterns c) wafers with pattern similar to Pattern 2 and pillars with height of 50 µm and 100 µm.

Finally, for improving the parylene penetration while decreasing the consumption and process time, the handle wafer is modified to have both pillars and perforations. Figure A.4 shows the fabrication flow for the handle wafer. The patterns are formed with a single mask in such a way that each pillar is placed at the center of four perforations and vice versa (Figure A.5a).

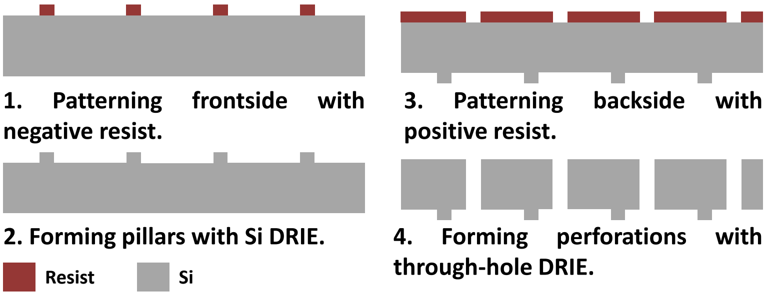

Figure A.4: Fabrication flow of the perforated handling wafer.

Perforated handle wafers with pillar heights of 10, 15, and 20 µm have been fabricated and coated concurrently with 15 µm-thick parylene. An aluminum weight of 75 g has been used to provide the parallelism of two substrates during the coating. Then, the attached substrates are diced, and the average penetration length for 10 and 15 µm pillars are measured as 0.7 and 1.1 mm, respectively. By using 20 µm pillars, parylene can penetrate and coat at least 4.5 mm long spacings (Figure A.5a). The quality of the attachment is analyzed by measuring the shear strength of the diced samples, and an average shear strength of 0.49 MPa is obtained for the 20 µm-pillar case. It is shown that the proposed method is a promising technique for integrating fragile or various shaped structures into low temperature and low stress MEMS processes, such as dicing, lithography, wet, and dry etching without degrading their characteristics.

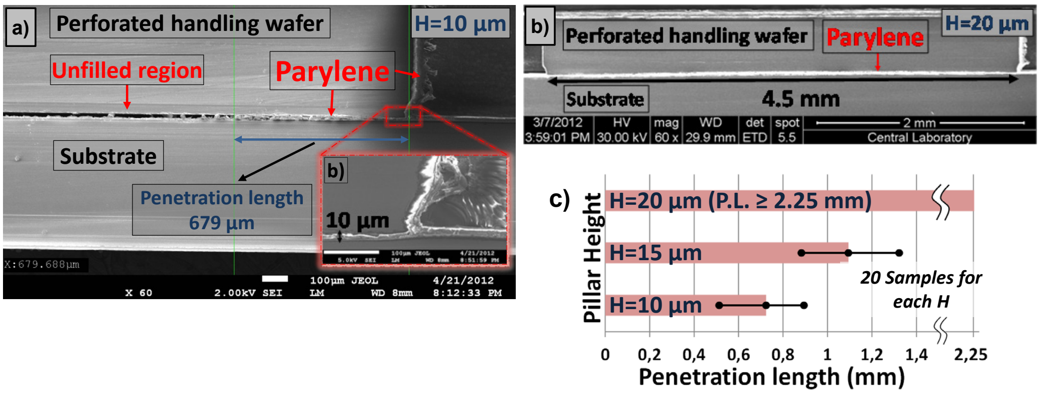

Figure A.5: SEM image of a a) fully filled, b) partially filled sample and c) its close-up view d) parylene penetration length comparison.